Optical nonlinearities in copper halide nanocrystals

Yingli Li

Optical nonlinearities in copper halide nanocrystals

Yingli Li

February 14, 1998

Contents

List of Figures

List of Tables

Chapter 1

Introduction

1.1 Background

People are hearts and people are communications. For better understanding and convenience, rapid and efficient exchange of information is desired in the future society. To fulfill the requirement, optoelectronic devices with high speed and large capacity are potentially needed. Recently, there has been increasing interest in searching of novel materials with large optical nonlinearities and fast optical response.

Studies on nanometer-scale semiconductors with various microstructures including the quantum wells, quantum wires, quantum dots, clusters and nanocrystals have been carried out intensively in recent decades, with the advances in fabrication technique and the sophisticated background for bulk semiconductors. [1] Great achievements have been made in studies on GaAs-based semiconductor quantum-well structures, indicating the promising prospect of low-dimensional semiconductor structures as for optoelectronic applications. [2, 3] In semiconductor microstructures, the boundary condition imposed on the bulk electronic states changes the electronic energy structure from bands to discrete levels which are tunable with geometric size. Meanwhile, the oscillator strength, which is distributed over continuum states in bulk materials, becomes concentrated on the sharp transition of excitons and consequently the excitonic optical nonlinearity is enhanced. It has been already known that quasi-two-dimensional excitons give rise to the strong nonlinear response in the vicinity of the band gap, from the intensive work on optical nonlinearities in GaAs-based semiconductor quantum-well structures.

The study on the nonlinear optical properties of nanocrystals may be traced back to the pioneering work by Jain and Lind in 1983. They first reported a work on the commercial glass filter containing CdS_xSe_{1-x} nanocrystals, and found a nonlinear susceptibility $|\chi^{(3)}|$ of about 1.3×10^{-8} esu at 532 nm. [4] This value is about 400 times larger than the bulk CdS value $\sim 3.4 \times 10^{-9}$ esu if one takes into account the low volume fraction ($\sim 1\%$) of the nanocrystals embedded in glass. Since then a great deal of efforts have been devoted

to fabricating various kinds of nanocrystals and elucidating the origin of nonlinearity in nanocrystals near their band-gap. Most of the works have been done on the II-VI compound semiconductors such as CdSSe and I-VII compounds like CuCl. In these direct-transition type semiconductors, confinement effects on the electron-hole pair are classified into the strong and weak confinement regimes, according to the ratio of the crystallite radius R to the exciton Bohr radius a_B. The nonlinear optical properties in nanocrystals have been also investigated for the corresponding confinement regimes.

In the strong confinement regime, the photoexcited electron and hole are individually confined. Theoretically, Schmitt-Rink, Miller and Chemla first discussed about the nonlinear absorption in nanocrystals smaller than a_B and suggested a state-filling mechanism. [5] The lowest interband transition was predicted to saturate like a two-level atomic system. A R^{-3}-dependence for $\chi^{(3)}$ could be inferred from the simple model without taking into account the size dependence of relaxation parameters. Experimental works have been intensively done using CdS_xSe_{1-x} nanocrystals. For instance, Roussignol, Ricard and Flytzanis investigated the wavelength dependence of $\chi^{(3)}$ for CdS_xSe_{1-x} nanocrystals, and observed the resonant enhancement of $\chi^{(3)}$ at the absorption peak due to the lowest transition of confined electron and hole. [6]. The energy dependence of $|\chi^{(3)}|$ could be qualitatively reproduced by using the standard two-level system formalism. On the other hand, a number of studies on the size dependence of $\chi^{(3)}$ have yielded inconsistent results; a larger nonlinear susceptibility for a larger size has been found for CdS_xSe_{1-x} nanocrystals by the saturation spectroscopy [7, 8] and degenerate four-wave mixing(DFWM) measurements, [9] while Roussignol et al. have shown that the larger $\chi^{(3)}$ values are obtained with decreasing sizes.[6] Besides, few of those studies concerned about the relaxation parameters except for the study by Shinojima, Yumoto and Uesugi. [9] They measured the size dependence of the effective nonlinear cross section σ_{eff} as well as the carrier recombination time τ using sputtered $CdS_{0.12}Se_{0.88}$ nanocrystals. [9] The σ_{eff}, which is proportional to $\chi^{(3)}/\alpha\tau$, shows a weak enhancement from $R/a_B = 0.25$ to $R/a_B = 2.5$ while $\chi^{(3)}$ increases greatly with the nanocrystal size.

In the weak confinement regime, the Coulomb interaction between the electron and hole yields an exciton and the exciton is confined as a quasiparticle. The nonlinearity arises from the exciton-exciton interaction which results in the deviation of harmonicity of the boson-like exciton within the nanocrystal , and the size enhancement of nonlinear susceptibility has been investigated theoretically and experimentally. The theoretical studies have shown that the confinement of the excitonic envelope wavefunction due to the infinite barrier potential gives rise to the enhancement of the oscillator strength for an exciton within the nanocrystal by a factor of R^3/a_B^3, and hence $\chi^{(3)}$ depends on the crystallite size. Such a giant oscillator strength effect has been confirmed for CuCl nanocrystals; the radiative decay rate of confined excitons is proportional to $R^{2.1}$ for glass matrix and

R^3 for NaCl crystal matrix.

The important role of the giant oscillator strength effect in the size enhancement of nonlinearity has been experimentally shown for CuCl nanocrystals by Kataoka et al, based on a two-level atomic model. As the quantum-confined exciton system can be modeled as a two-level atomic system, the imaginary part of $\chi^{(3)}$ on resonance in the low density regime is given by

$$Im\chi^{(3)} = (\frac{e^2}{2m_0\omega})^2\hbar \cdot N \cdot f_x^2 \cdot \frac{T_1}{\Gamma_h^2}. \tag{1.1}$$

Here, T_1 and Γ_h are longitudinal relaxation time and homogeneous width of excitons, respectively, and f_x, N are the oscillator strength and the number density of nanocrystals, respectively. The detailed study measuring the susceptibility on resonance and the relaxation parameters T_1 and Γ_h revealed that the oscillator strength per nanocrystal exhibits an intriguing feature in the size range of $R = 1.5 - 8.0$ nm at 80 K, i.e., $f_x \propto R^{2.2}$ at 1.9 - 4.0 nm and subsequently decreases for $R \geq 5.0$ nm.

Although the $R^{2.2}$-dependence of f_x indicates the giant oscillator strength of coherently generated excitons in nanocrystals, the saturation and decrease of f_x for larger sizes can not be explained by the two-level atomic model. This result suggests that there exist further contributions such as higher excited states and a two-exciton state to the nonlinearity in larger nanocrystals, and it has been left to be clarified. Further detailed studies on nanocrystals with sizes covering the two regimes are necessary to obtain a thorough understanding of the inherent mechanisms determining the size dependence of nonlinearities in nanocrystal materials. In CuBr, the exciton Bohr radius is 1.25 nm, which is roughly twice that of CuCl, and one can investigate confinement effects and size dependence of $\chi^{(3)}$ over a wide range of crystallite sizes from the strong confinement regime to the weak confinement regime.[10] The lowest exciton state in CuBr is the Z_{12} exciton consisting of light and heavy holes in the Γ_8 band, while that of CuCl is the Z_3 exciton coming from the Γ_7 band. In addition, a k-linear term in the Γ_8 band is not negligible in CuBr, and thus the Z_{12} exciton has a multi-component character. In the solid solution of $CuBr_xCl_{1-x}$, on the other hand, the valence band structure changes continuously with a composition ratio x the lowest valence band consists of Γ_7 band for $x < 0.26$, while it consists of Γ_8 band for $x > 0.26$. For $x \simeq 0.26$ the Γ_7 and Γ_8 bands are nearly degenerate at the wavevector $k = 0$. [11, 12]

1.2 Purpose

The aim of this study is to elucidate the origin for the size-dependent enhancement of nonlinear susceptibilities in copper halide nanocrystals, including CuCl, CuBr and $CuBr_xCl_{1-x}$ (with $x = 0.97, 0.26, 0.11$) nanocrystals, which show the quantum confine-

ment effects of excitons. First, the size dependence of the third-order nonlinear susceptibility $\chi^{(3)}$ and its origin are investigated for CuBr nanocrystals. $\chi^{(3)}$ due to the confined excitons is measured by means of degenerate four-wave-mixing using a nanosecond laser. The energy dispersion of $\chi^{(3)}$ is observed near the exciton resonance, and the resonant $|\chi^{(3)}|/\alpha$ values at the Z_{12}-exciton resonance is measured for nanocrystals with various radii to obtain the size dependence. Then the size-dependent nonlinearity is analyzed by a two-level atomic model, which relates the nonlinearity to the exciton lifetime T_1 , homogeneous width Γ_h and the oscillator strength f_x. The nanocrystal size-dependences of T_1 and Γ_h are then investigated, respectively. The time-resolved photoluminescence spectroscopy and the resonant photoluminescence spectroscopy are employed to measure T_1 and Γ_h, respectively. Using the measured parameters the size dependence of the oscillator strength is derived, and the origin for the size-dependent nonlinearity in CuBr nanocrystals is discussed comparing with that for CuCl.

Second, based on the above comparison, the role of the valence band structures in the nonlinearity of nanocrystals is investigated. The size-dependent nonlinearity in $CuBr_xCl_{1-x}$ nanocrystals is studied. The $CuBr_xCl_{1-x}$ nanocrystals with $x = 0.97(0.11)$ is used as it has the same valence band structure as CuBr(CuCl). The solid solution with $x = 0.26$ where the valence bands are nearly degenerate is also investigated. The size-dependences of the resonant $\chi^{(3)}$, T_1 and Γ_h are measured, and the size-dependences of the oscillator strength are derived for the three composition ratios of $x = 0.97, 0.26$ and 0.11. All the results are compared to elucidate the size-dependent behaviors of nonlinearity. The observed saturation behavior for large sizes in CuCl-type nanocrystals is discussed on the basis of the theory taking into account the two-exciton states. The different behaviors of size dependence for large sizes between the CuCl- and CuBr-type nanocrystals indicate a role of the valence band structure in the size-dependent enhancement.

Third, the enhancement factors of the giant oscillator strength with respect to the bulk oscillator strength are estimated from the experimental data and compared among the copper halide nanocrystals with various composition ratios. The results will give an experiment evidence for the giant oscillator strength effect due to the exciton confinement imposed by the matrix potential.

Finally, the size dependence of the nonlinearity in nanocrystals is compared with the quantum well structures, in order to obtain an overall view on the dimension dependence of the nonlinearity in restricted geometries. A guideline for the designing of nonlinear optical materials using nano-structured semiconductors is obtained.

The thesis is organized as follows. In Chapter 2, the theoretical background for the optical properties of nanostructured semiconductors is presented. In Chapter 3, the sample preparation of copper halide nanocrystals and the experimentals are described. The experimental results and the size dependence of the oscillator strength for CuBr and

$CuBr_xCl_{1-x}$ nanocrystals are presented in Chapter 4 and Chapter 5, respectively. Finally, the conclusion is drawn in Chapter 6.

Chapter 2

Theoretical background for optical properties of nanostructured semiconductors

2.1 Electronic structures of nanostructured semiconductors

2.1.1 Excitons

The theory of excitons was first formulated in 1930s by Frenkel, Peierls and Wannier. Experimentally, characteristic absorption lines within the band gap were observed in insulators, or in certain semiconductors. These absorption features were attributed to the elementary excitations within the band gap. The excitations are known as excitons; they correspond to a bound electron-hole pair state as a consequence of the attractive Coulomb interaction between an electron excited from the valence band and the hole left behind. [13, 14, 15]

The exciton state can be analyzed within the framework of the effective-mass approximation. Consider the case where an electron with effective mass m_e is excited to the conduction band and a hole with m_h is left behind in the valence band, and take into account the Coulomb interaction. The Hamiltonian modeled for the exciton in cgs unit is

$$H = \frac{p_e^2}{2m_e} + \frac{p_h^2}{2m_h} - \frac{e^2}{\kappa|r_e - r_h|}, \tag{2.1}$$

where κ is the appropriate dielectric constant, and $r_e(r_h)$ is the coordinate of the electron (hole). The lattice polarization contribution to the dielectric constant should be included if the frequency of motion of the exciton is higher than the optical phonon frequencies.[13] It has been assumed that the conduction and valence bands are nondegenerate and of standard parabolic form. This Hamiltonian for the two-body exciton system is just analogous to that for the Hydrogen atom. Therefore, the eigenfunctions and eigenvalues are

obtained in a straight-forward fashion, in analogy to the Hydrogen-atom problem. The exciton wave function $\Psi(r_e, r_h)$ reads as:

$$\Psi(r_e, r_h) = \phi(r_e - r_h) \cdot \exp(i\vec{K} \cdot \vec{r}) \cdot u^c_{k_e}(r_e) u^v_{k_h}(r_h) \quad . \tag{2.2}$$

Here in the right part of the equation, the first part $\phi(r_e - r_h)$ is the wave function of Hydrogen-atom describing the relative motion of the electron and the hole while the second part describes the translational motion of the mass-center. $\vec{K}$ is the wave number vector of exciton satisfying $\vec{K} = \vec{k_e} + k_h$, and $\vec{r}$ is the displacement vector of the mass-center. $u^c_{k_e}$ ($u^v_{k_h}$) is the well-known atomic part of Bloch function for the conduction(valence) band electron(hole). The extent of exciton, characterized by the Bohr radius a_B, is of the form

$$a_B = \frac{\kappa\hbar^2}{\mu e^2}, \tag{2.3}$$

and the Rydberg energy is

$$E_R = -\frac{e^2}{2\kappa a_B}, \tag{2.4}$$

where μ is the reduced mass, $\mu = 1/(m_e^{-1} + m_h^{-1})$. The eigenvalue is

$$E_n = E_g - \frac{1}{n^2} E_R + \frac{\hbar^2 K^2}{2M}, \tag{2.5}$$

where E_g is the band-gap energy, M is the translational mass of exciton, and n is an integer. The $\hbar^2 K^2/2M$ term corresponds to the kinetic energy of the translational motion. The momentum of the exciton is a good quantum number, provided the translational symmetry in infinite bulk crystal. The eigenstate of the translational motion describes the elementary excitation that coherently spreads throughout the crystal, like a plane wave. The translational motion of exciton is obviously dependent on the boundary condition in finite solids, and this will be discussed in the following section.

The exciton is a rather idealized boson, because the exciton-exciton interaction is negligible in the infinite bulk crystal. Deviation from the boson character of excitons becomes important if the interaction gets stronger, for example, when the exciton is confined spatially.

2.1.2 Quantum confinement effects

Let us consider a finite spherical semiconductor crystallite with radius R, embedded in the matrix with a band gap much larger than that of the semiconductor. The well defined boundary gives rise to the quantization of elementary excitations. The difference of band gap functions as a barrier of potential. The electronic structures and optical properties of excitons in this finite-sized solid can be modeled as the fundamental problem

of quantum mechanics: a Hydrogen atom confined in an infinite-potential spherical well. The Hamiltonian (2.1) is rewritten as

$$H = \frac{p_e^2}{2m_e} + \frac{p_h^2}{2m_h} - \frac{e^2}{\kappa|r_e - r_h|} + V(r_e) + V(r_h), \tag{2.6}$$

where $V(r_i)|_{i=e,h}$ equals zero when $0 \leq r_i \leq R$ and becomes infinity otherwise.

If the size of the crystallite is minimized to the order of exciton Bohr radius, quantum confinement effects of the excitons shall appear and drastic change of physical properties from that of bulk is expected. For example, the electronic energy spectrum will be characteristic of discrete levels in contrast to that of bulk crystal, and the ground state energy of the exciton shifts to higher energy, etc. Theoretically, the ground state property of the electron and the hole has been discussed within the framework of the effective-mass approximation by Efros and Efros, Brus and Kayamanuma, etc.[16, 17, 18] The quantum confinement effect in direct gap semiconductor nanocrystals can be classified into two limiting regimes: strong and weak confinement regimes, according to the ratio of R/a_B in the bulk material.

The strong confinement regime, also named as the individual confinement regime, corresponds to the case $R/a_B \ll 1$, where the Coulomb interaction of the electron and the hole is negligible compared to the kinetic energy. The two-particle system is pictured as two individual particles confined within the well. The electron and the hole should occupy primarily the individual lowest eigenstate of the quantum well. The wavefunction for the electron and the hole is

$$\Psi(r_e, r_h) = \psi(K_{ln} r_e)\psi(K_{ln} r_h) \cdot u^c(r_e)u^v(r_h), \tag{2.7}$$

and $\psi(x)$ is a function defined as

$$\psi(x) = Y_{lm}(\theta, \phi) j_l(x). \tag{2.8}$$

Here $j_l(x)$ is the l-th spherical Bessel function while K_{ln} satisfies the boundary condition $j_l(K_{ln}R) = 0$, and $Y_{lm}(\theta, \phi)$ is the spherical harmonic function. The corresponding energy to create an electron-hole pair is [16]

$$E = E_g + \frac{\hbar^2 K_{ln}^2}{2\mu}. \tag{2.9}$$

The weak confinement regime, also known as the mass-center confinement regime or the exciton confinement regime, corresponds to the case of $R/a_B \gg 1$, where the Coulomb interaction is dominant over the kinetic energy. The character of the exciton as a quasiparticle is well conserved, and the translational degrees of freedom are confined. The wavefunction of the exciton is written as

$$\Psi(r_e, r_h) = \phi(r_e - r_h) \cdot \psi(r) \cdot u^c(r_e)u^v(r_h). \tag{2.10}$$

and $\psi(r)$ is of the form

$$\psi(r) = j_l(K_{ln}r)Y_{lm}(\theta,\phi). \qquad (r = \frac{m_e r_e + m_h r_h}{m_e + m_h}) \tag{2.11}$$

By comparing Eq. (2.10) with Eq. (2.2), one can understand that $\psi(r)$ is the envelope of the exciton confined in the sphere. The eigenvalue of the confined exciton is

$$E = E_g - \frac{E_R}{n^2} + \frac{\hbar^2 K_{ln}^2}{2M}. \tag{2.12}$$

For allowed transitions, $l = 0$ and $K_{0n} = n\pi/R$.

Kayanuma's calculation using Ritz's varitional method indicates that the transition between the two limiting regimes occurs at around $R/a_B \simeq 2 \sim 3$, i.e., the regime $R/a_B \leq 2$ can be well described by the strong confinement picture while the weak confinement picture accounts well for the region $R/a_B \geq 4$. The result is shown in Fig. 2.1. [18]

The quantum confinement gives rise to the change of the electronic wavefunction as well as the energy structure compared with the bulk, and consequently results in the drastic change of other optical properties. These are generally referred to as quantum confinement effects.

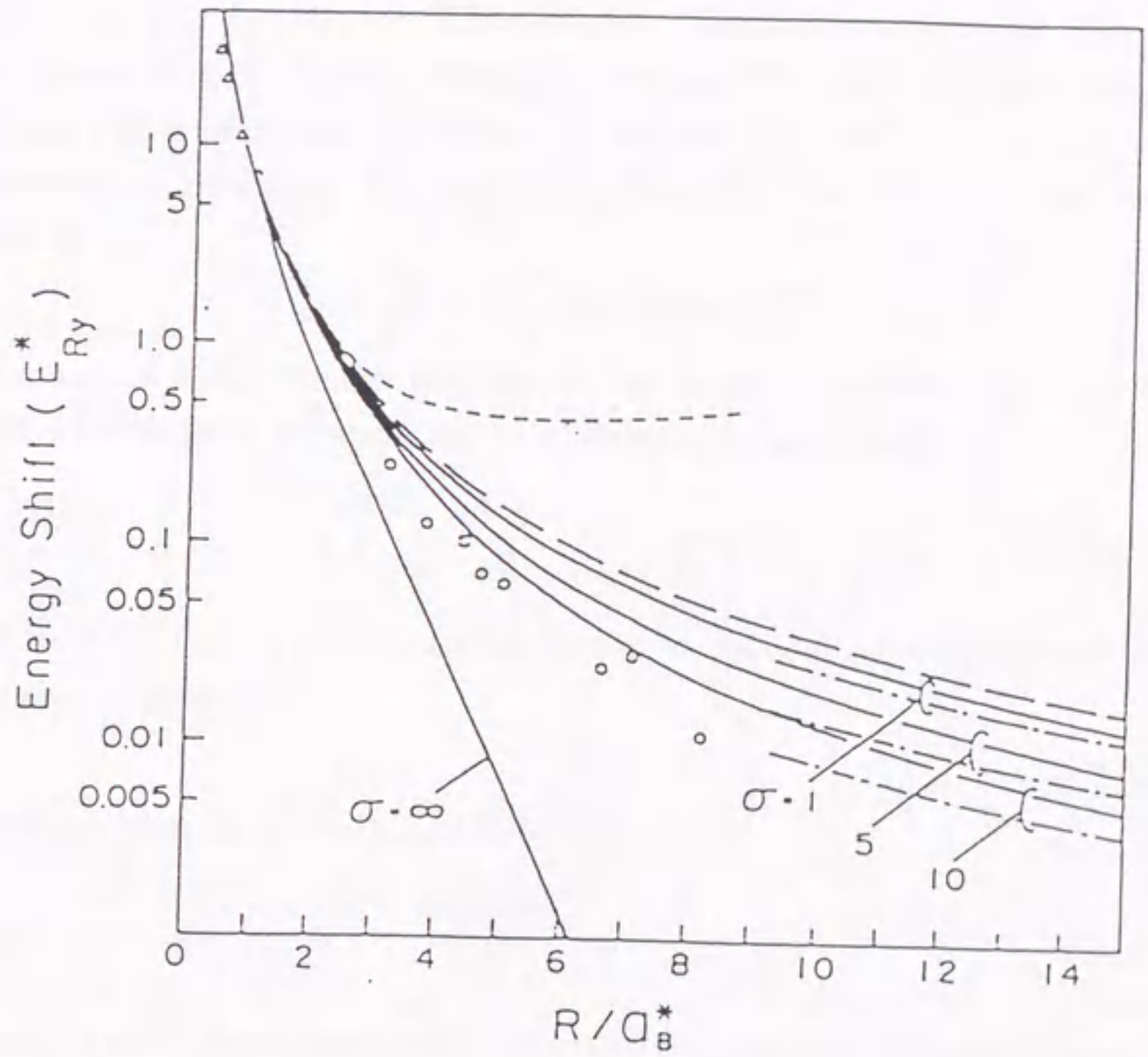

Figure 2.1: Kayanuma's theoretical calculation of the higher-energy shift of the ground state of the electron-hole system in the spherical quantum well (solid lines) with $\sigma = m_h/m_e$ as a fixed parameter. The short-dashed line and the dashed-dotted lines represent the asymptotic results for the strong and weak confinement regime, respectively. The long-dashed line is the result by a one-parameter variational calculation. The observed values of the luminescence peak in the CuCl microcrystals in NaCl(open dots) and the absorption peak of CdS microcrystals in the silicate glass(open triangles) are also plotted.

2.1.3 Oscillator strength of excitons

The dielectric polarization of matter occurs as a result of the displacements of ions and/or transition of electrons. In classical electromagnetics, the polarization is phenomenologically described by the Lorentz oscillator model. In the Lorentz model, the matter is treated as an ensemble of dipoles vibrating with various angular frequencies and each dipole oscillates like a harmonic oscillator. For an oscillator with charge e, mass m_0 and angular frequency ω_0 moving in the external field of $E(= E_0 exp(-i\omega t))$, the equation of motion reads as

$$m_0(\frac{d^2x}{dt^2} + \gamma\frac{dx}{dt} + \omega_0^2 x) = e \cdot E, \tag{2.13}$$

where x denotes the displacement and the second term in the left part of the equation describes the friction force proportional to velocity. The solution for x is

$$x = \frac{e}{m_0} \cdot \frac{1}{\omega_0^2 - \omega^2 - i\gamma\omega} \cdot E \ . \tag{2.14}$$

Suppose the number density of the such oscillators is N_0, and since the polarization p due to this oscillator is given by

$$p = N_0 ex, \tag{2.15}$$

The dielectric function in cgs unit is of the form

$$\epsilon = 1 + \frac{4\pi N_0 e^2}{m_0} \cdot \frac{1}{\omega_0^2 - \omega^2 - i\gamma\omega}. \tag{2.16}$$

If we consider the case where the number density of the total oscillators is N, and f denotes the percentage of the certain oscillators with frequency ω_i, The dielectric function $\epsilon(\omega)$ is written as a summation over i as

$$\epsilon(\omega) = 1 + \Sigma\frac{4\pi N e^2}{m_0} \cdot \frac{f}{\omega_i^2 - \omega^2 - i\gamma\omega}. \tag{2.17}$$

f, a non-dimensional parameter, describes the number of certain oscillators that contribute to the polarization under consideration here.

In quantum mechanics, optical transitions in solids can be calculated using a time-dependent perturbation theory. The dielectric function obtained using the dipole transition approximation is just in the same form as that of (2.17), and f is expressed as

$$f = \frac{2m_0\omega_i}{\hbar} \cdot |< i|x|f >|^2 \tag{2.18}$$

for the transition from state $|i>$ to state $|f>$ with the transition energy $\hbar\omega_i$, and x is defined as the polarization direction of external electric field. f. is named as the oscillator

strength for the transition of one electron. In the case of impurity absorption, for example, f is proportional to the absorption area, i.e.,

$$\int \alpha(\omega)d\omega = \frac{2\pi^2 e^2}{m_0 c} \cdot \frac{N_i f}{\sqrt{\epsilon_b}}, \tag{2.19}$$

where N_i is the number density of impurities and ϵ_b is the background matrix dielectric constants. For excitons in the bulk semiconductor crystal with the direct allowed gap, the 1s-exciton oscillator strength per unit cell f_0 is

$$\begin{aligned} f_0 &= \frac{2m_0\omega_0}{\hbar} \cdot |<c|x|v>|^2 \cdot |\phi_{1s}(0)|^2 \cdot v \\ &= \frac{2m_0\omega_0}{\hbar}|p_{cv}|^2 \cdot |\phi_{1s}(0)|^2 \cdot v, \end{aligned} \tag{2.20}$$

where $|\phi_{1s}(0)|^2$ $(= 1/\pi a_B^3)$ denotes the probability the electron stays at the lattice site of the hole, v denotes the unit cell volume, and the matrix p_{cv} describes the transition moment between the conduction band and the valence bands. [13] f_0 is related to Δ_{LT} (the energy splitting of the transverse and the longitudinal excitons with zero momenta) by

$$f_0 = \frac{2\epsilon_\infty \Delta_{LT} E_T}{(\hbar\omega_p)^2}, \tag{2.21}$$

where ϵ_∞ is the high-frequency relative dielectric constant, E_T is the energy of the transverse exciton and $\omega_p = 4\pi N_0 e^2/m_0$. Δ_{LT}, which may be determined experimentally, is a parameter that arises from the repulsive interaction between photon and exciton when mixing to form the polariton, and it reflects the strength of interaction between the light and the exciton.

2.1.4 Giant oscillator strength

Let us now consider the oscillator strength of the lowest exciton confined in a spherical infinite potential. In the weak confinement regime, the exciton oscillator strength per crystallite can be calculated using Eq. (2.18) and (2.10), i.e.,

$$f_x = \frac{2m\omega_x}{\hbar}|\int \Psi(r,r)p_{cv}\ d^3r|^2, \tag{2.22}$$

where the integral is carried out over the crystallite sphere, and $\hbar\omega_x$ is defined as the transition energy. For the lowest confined-exciton state $(n = 1, m = l = 0)$, the center-of-mass motion takes the form of

$$\psi(r) = \sqrt{\frac{1}{4\pi}} \cdot \frac{\sin(\pi r/R)}{\pi r/R}, \tag{2.23}$$

and the electron-hole relative motion is expressed explicitly as

$$\varphi_{1s}(r_e - r_h) = \sqrt{\frac{1}{\pi a_B^3}} \cdot exp(-\frac{r_e - r_h}{a}), \tag{2.24}$$

respectively. The transition dipole moment is given by

$$\int \Psi(r,r) p_{cv}\ d^3r = \phi_{1s}(0) \cdot \sqrt{\frac{8}{\pi}} R^{3/2} \cdot p_{cv}. \tag{2.25}$$

As a result, the oscillator strength is

$$f_x = |\int \Psi(r,r)\ d^3r|^2 \cdot \frac{2m\omega_x}{\hbar}|p_{cv}|^2 \tag{2.26}$$

$$= \frac{8}{\pi^3}(\frac{R}{a_B})^3 \cdot (\pi a_B^3 \cdot f_0)\ . \tag{2.27}$$

3e f_x for the confined exciton state per crystallite is enhanced by a factor of $(R/a_B)^3$. This is called the giant oscillator strength.[18, 19, 20] The volume dependence comes from the volume dependent transition moment. (Also see Eq. (2.18).) It is essentially the same as the effect of the giant oscillator strength which was first proposed by Rashba and Gurgenishvili for the bound exciton state.[21, 22] The giant oscillator strength originates from the fact that the exciton spreads coherently throughout the volume. Such an enhancement of oscillator strength results in the enhancement of any transitions relevant to the volume-dependent transition moment. The co-operative transition of spontaneous radiation is theoretically expected to give rise to the superradiance, the radiation with great transition strength.[23] The volume-dependent dipole moment may lead to the enhancement of optical nonlinearities with the crystallite size.[19, 20]

The size dependence of oscillator strength in the wide range of radius, including the strong and weak confinement regime, was calculated by Kayanuma using Ritz's variational method where infinite spherical potential was assumed, [18] and the result is shown in Fig. 2.2. For $R/a_B > 2$ the cubic dependence is obtained, while the dependence becomes weak for $R/a_B < 2$. In contrast to the weak confinement regime, the transition dipole moment in the strong confinement regime is shown to be equal to p_{cv}, i.e., independent of the radius R. [19] Consequently, the oscillator strength per crystallite is also constant. The size-dependent enhancement of oscillator strength exists only in the weak confinement regime.

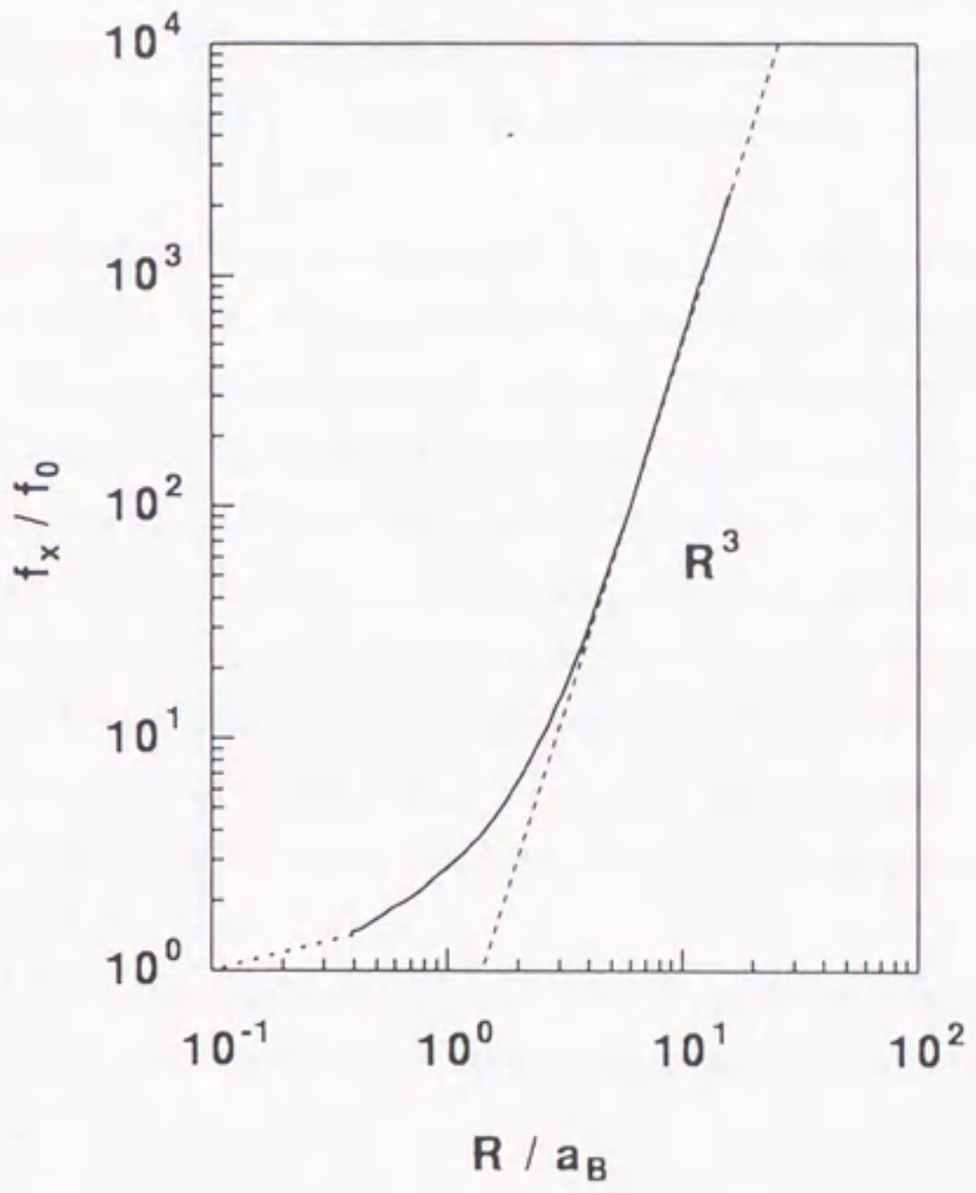

Figure 2.2: Ratio of the oscillator strength per nanocrystal to that for the bulk exciton per unit cell as a function of R/a_B, calculated by Kayanuma.[18] The dashed line indicates the R^3-dependence of the giant oscillator strength.

2.1.5 Band structures of copper halides

CuBr, CuCl and their solid solution are all copper halides. The copper halides have the zincblende structure under ambient conditions. The Cu atoms form tetrahedrally coordinated halides isomorphic with the diamond-like semiconductors. The valence bands of these I-VII semiconductors originate from the filled d^{10} shell of the metal$^+$ ions and the s^2p^6 rare gas configuration of the halogen$^-$ ions, while the conduction bands come from the 4s-electron of Cu. All these semiconductors are of direct-transition type, with both the bottom of the conduction band and the top of the valence band locate at the Γ point ($k = 0$) in the k-space. Like other zincblende type semiconductors, the valence band is of Γ_{15} symmetry, having a six-fold degeneracy including the freedom of spin. It splits into the fourfold Γ_8- and the twofold Γ_7- band due to the spin-orbit interaction Δ_{so} of valence electrons.

A characteristic property in copper halides is that the spin-orbit interaction changes its sign from CuCl to CuBr, i.e., the Γ_8 band is on the higher-energy side of the Γ_7 band for CuBr, while the energy order is reversed in CuCl. This is due to: (1) since the energies of the d-levels of Cu are close to those of the p-levels of halogen, the heavy hybridization of the p- and d-levels occurs; (2) the spin-orbit interaction for the Cu$^+$ 3d electron has a reverse sign of that for the halogen$^-$ p electron; (3) the ratio of the Cu$^+$ 3d electron state, i.e., the percentage of time the valence electron stays on the Cu atom site, are 75, 64 and 50% for CuCl, CuBr and CuI, respectively. [24, 25, 12] The mixture of CuBr and CuCl makes a solid solution of $CuBr_xCl_{1-x}$. The Δ_{so} changes continually from -70 meV for CuCl to 150 meV for CuBr. The Γ_8 band becomes nearly degenerate with the Γ_7 band at $x = 0.26$. (See Fig. 2.3.)

The electron and hole Hamiltonian, H_e, H_s and H_h, in the effective-mass approximation are expressed by the wave vector k and the angular momentum operator J (J=3/2) for the hole as [26, 27, 28, 29]

$$H_e = \frac{\hbar^2}{2m_e}k^2$$

$$H_s = \frac{\hbar^2}{2m_0}\gamma_1 k^2$$

$$\begin{aligned} H_h &= \frac{\hbar^2}{m_0}\left[(\frac{1}{2}\gamma_1 + \frac{5}{4}\gamma_2)k^2 - \gamma_2(k_x^2J_x^2 + k_y^2J_y^2 + k_z^2J_z^2) - 2\gamma_3(\{k_xk_y\}\{J_xJ_y\} + c.p.)\right] \\ &\quad +\hbar K_l(k_x(J_y^2 - J_z^2)J_x + c.p.), \end{aligned} \tag{2.28}$$

where H_s stands for the split-off band Γ_7 while H_h is for Γ_8, $\{k_xk_y\} = (k_xk_y + k_yk_x)/2$ and so on, m_e and m_0 are the masses of the conduction and free electrons, respectively, $\gamma_1, \gamma_2, \gamma_3$ are the Luttinger parameters, $\hbar K_l$ is the coefficient of the k-linear term, and c.p. means the cyclic permutation of the preceding term. The dispersion of the valence

band is isotropic only when $\gamma_2 = \gamma_3 = \gamma$. The isotropic k-quadratic dispersion is given by assuming $K_l = 0$

$$E(k^2) = \frac{\hbar^2}{2m_0}(\gamma_1 \pm 2\gamma)k^2, \tag{2.29}$$

where the "-" sign corresponds to the heavy-hole. The introduction of k-linear term results in the splitting of the heavy-hole dispersion at small k. The energy dispersion diagram in k-space for the copper halides is shown in Fig. 2.3. We can see from the figure the multi-branch character of the Γ_8 band which is composed of light hole and heavy hole. The K-dependent Hamiltonian for the exciton, characterized by the valence band, is given by replacing $\gamma_1, \gamma_2, \gamma_3$ and K_l with the corresponding exciton parameters $\gamma_1^{ex}, \gamma_2^{ex}, \gamma_3^{ex}$ and K_l^{ex} for the hole Hamiltonian in equation (2.28), respectively. Relations between them are as follows.

$$\begin{aligned} \gamma_1^{ex} &= \beta_h \gamma_1, \quad & \gamma_2^{ex} &= \beta_h^2 \gamma_2, \\ \gamma_3^{ex} &= \beta_h^2 \gamma_3, \quad & K_l^{ex} &= \beta_h K_l, \end{aligned} \tag{2.30}$$

where $\beta_h = m_0/(m_0 + m_e\gamma_1)$.

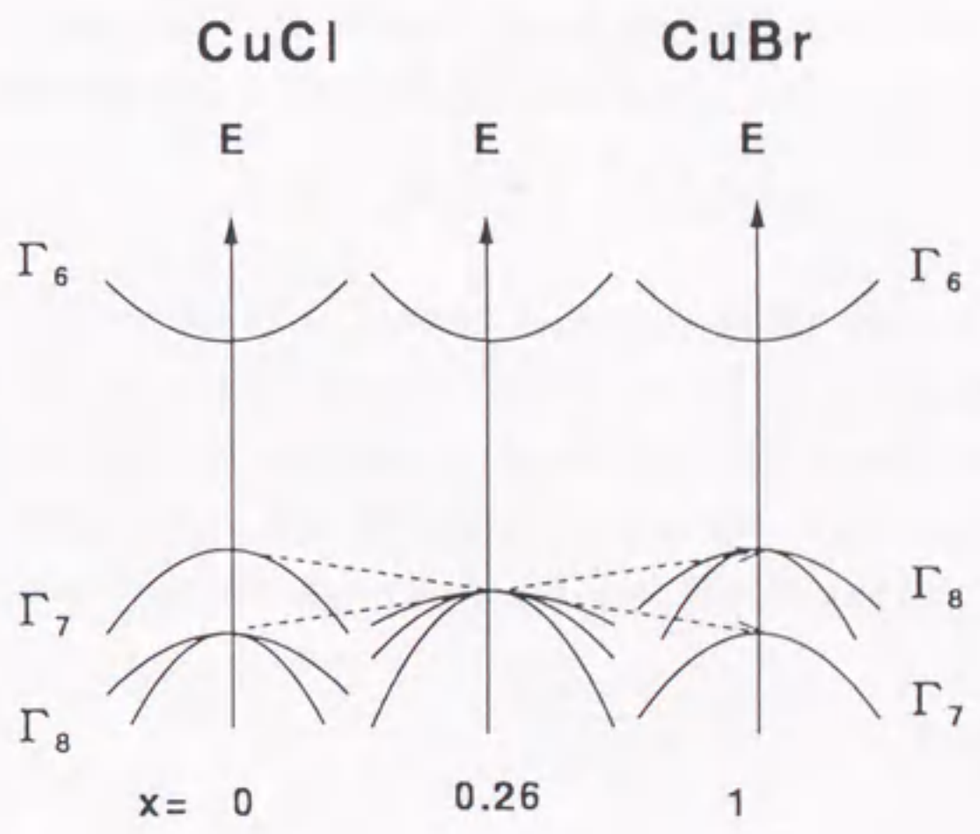

Figure 2.3: Band structure for copper halides.

2.2 Nonlinear optical polarization

2.2.1 Nonlinear susceptibilities

Since the appearance of the laser in 1950s as one of the greatest inventions in the history of sciences, the fascinating field of nonlinear optics has undoubtedly become one of the broadest scope and the most influential proponents. [30, 31]

In the classical physics the interaction of light with matter, including the absorption and the scattering of light, is understood as the problem of propagation of the electric and the magnetic fields governed by the set of Maxwell's equations. Let us take a look at the propagation equation of the electric field in matter, i.e.,

$$\nabla \times \nabla \times \vec{E} + \frac{1}{c^2}\frac{\partial^2 \vec{E}}{\partial t^2} = -\frac{4\pi}{c^2}\frac{\partial^2 \vec{P}}{\partial t^2}. \tag{2.31}$$

One can see that the variation of the time-dependent polarization acts as the source creating electric fields in other spatial places. The dependence of polarization on the electric field, known as the constitutive equation, is usually a linear equation under the condition of weak fields. Consequently, only the electric fields with the same frequency as that of the external field exist in the matter, which belongs to the category of linear optics.

Under the circumstance of high intensity laser irradiation or equivalently strong fields, the polarization is generally expressed in cgs unit as

$$\vec{P} = \chi^{(1)}\vec{E} + \chi^{(2)}\vec{E}\vec{E} + \chi^{(3)}\vec{E}\vec{E}\vec{E} + \ldots, \tag{2.32}$$

where $\chi^{(1)}$, $\chi^{(2)}$ and $\chi^{(3)}$ are the first-, second- and third-order susceptibilities, respectively; $\chi^{(1)}$ corresponds to the polarizability and others are called nonlinear susceptibilities. It is classified into the category of nonlinear optics. The higher-order polarization generates new fields of double-frequency, triple-frequency and so on. Considering the linear and the third-order polarization, the refractive index n and the absorption coefficient α can be expressed as

$$n = n_0 + n_2 E^2, \tag{2.33}$$

$$\alpha = \alpha_0 + \alpha_2 E^2. \tag{2.34}$$

Such an optical field dependent character is applicable to all-optical manipulating devices. For an instance, the refractive index modulated by two light pulses can diffract a third-light pulse like a grating, and the way of diffraction is under control of the modulation, i.e., the two light pulses. The above configuration is equivalent to a high-speed switching device.

It is worthy noting that the magnitude of the susceptibility depends on the choice of definition which is relevant to the unit systems adopted in electromagnetics. The relations between the cgs and MKS units are summarized in Table 2.1. $\chi^{(3)}$ throughout this thesis is adopted as the cgs (esu) unit susceptibility defined here unless remarks have been noted.

Table 2.1: Comparisons of cgs and MKS unit formula

cgs	**MKS**
$D = E + 4\pi P$	$D = \epsilon_0 E + P$
$P = \chi^{(1)}_{cgs} E + \chi^{(3)}_{cgs} E^3$	$P = \epsilon_0(\chi^{(1)}_{MKS} E + \chi^{(3)}_{MKS} E^3)$
$\nabla^2 E = \frac{\epsilon}{c^2}\frac{\partial^2 E}{\partial t^2} + \frac{4\pi}{c^2}\frac{\partial^2 P}{\partial t^2}$	$\nabla^2 E = \frac{\epsilon}{c^2}\frac{\partial^2 E}{\partial t^2} + \frac{1}{c^2}\frac{\partial^2 P}{\partial t^2}$

To obtain the expressions of the nonlinear susceptibilities, the semi-classical theory, combining the classical electromagnetics with the quantum mechanical descriptions for the material, serves the convenient and effective method. Here is shown the procedure of obtaining the expressions for nonlinear susceptibilites in the density matrix formalism.

Let ψ be the wavefunction of the material system under the influence of the electromagnetic filed. The density matrix operator is defined as the ensemble average over the product of the ket and bra state vectors

$$\rho = \overline{|\psi><\psi|}, \tag{2.35}$$

and the ensemble average of the electric polarization P is given by

$$< P >= \overline{<\psi|P|\psi>} = Tr(\rho P), \tag{2.36}$$

The equation of motion for the density matrix ρ is

$$i\hbar\frac{d\rho}{dt} = [H, \rho], \tag{2.37}$$

where

$$H = H_0 + H_{int}, \tag{2.38}$$

$$H_{int} = er \cdot E exp(-i\omega t). \tag{2.39}$$

Here, H_0 is the unperturbed Hamiltonian, and H_{int} is the interaction Hamiltonian in the electric dipole approximation where only the electronic contribution to the susceptibilities has been considered. By inserting the equation of motion with the perturbation expansions of

$$\rho = \rho_0 + \rho_1 + \rho_2 + \ldots, \tag{2.40}$$

one finds

$$i\hbar \frac{d\rho_n}{dt} = [H_0, \rho_n] + [H_{int}, \rho_{n-1}] \tag{2.41}$$

where $n = 1, 2, \ldots$. The solutions are obtained to be

$$\rho_0 = exp(-\frac{H_0}{k_B T}) \tag{2.42}$$

$$\rho_1 = U_0(t)\frac{1}{i\hbar}\int_{-\infty}^{t} dt_1 [H_{int}(t_1), \rho_0] U_0(-t) \tag{2.43}$$

$$\rho_2 = U_0(t)\frac{1}{(i\hbar)^2}\int_{-\infty}^{t} dt_1 \int_{-\infty}^{t_1} dt_2 [H_{int}(t_1), [H_{int}(t_2), \rho_0] U_0(-t) \tag{2.44}$$

and so on, where $U_0(t) = exp(-iH_0 t/\hbar)$. The expansion of the polarization is expressed as

$$< P >=< P^{(1)} > + < P^{(2)} > + < P^{(2)} > + \ldots, \tag{2.45}$$

while

$$< P^{(n)} >= Tr(\rho^{(n)} P). \tag{2.46}$$

The full expressions for the polarization $< P >$ and the susceptibilities $< \chi^{(n)} >$ follow immediately from the expressions of $\rho^{(n)}$, and the comparison of Eq. (2.45) with Eq. (2.31).

2.2.2 Two-level model

Consider a system composed of discrete energy levels, and the frequency of the applied external field is near or just at resonance with certain two levels of the system under study. In general, the system may be approximately treated as a two-level atomic system. For excitons confined in the nanocrystal, the two-level model may be appropriate when the laser light is tuned to the certain confinement level.

Consider a two-level atomic system, with two energy levels $|e >$ and $|g >$ with an energy separation of $\hbar\omega_0$, interacting with two nearly resonant light beams with the frequencies of ω_1 and ω_2, respectively. The Hamiltonian reads

$$H_{ge} = H_{eg}^{*} = -\mu_{ge}[E_1 exp(-i\omega_1 t) + E_2 exp(-i\omega_2 t)] + c.c. \tag{2.47}$$

The equation of motion, with the longitudinal (T_1) and transverse (T_2) relaxation times taken into account, is written down as

$$\frac{\partial \rho_D}{\partial t} = -\frac{2i}{\hbar}(H_{ge}\rho_{ge} - \rho_{eg}H_{ge}) - \frac{1}{T_1}(\rho_D - \rho_D^{(0)}), \tag{2.48}$$

$$\frac{\partial \rho_{ge}}{\partial t} = \frac{\partial \rho_{eg}^{*}}{\partial t} = -\frac{i}{\hbar} H_{ge}\rho_D - (\frac{1}{T_2} + i\omega)\rho_{ge},$$

where $\rho_D = \rho_{gg} - \rho_{ee}$ and $\rho_{gg} + \rho_{ee} = 1$, $\rho^{(0)}$ is the value of ρ_D without the light beams, μ_{ge} is the electric dipole matrix element of the transition. [32, 33] The straight forward calculation of $\rho_{ge}^{(3)}$ with the frequency $\omega_3 = 2\omega_1 - \omega_2$ and with the definition

$$P^{(3)} = \mu_{eg}\rho_{ge}^{(3)} + c.c. = \chi^{(3)}(\omega_3)E_1^2 E_2^{*} exp(-i\omega_3 t) + c.c., \tag{2.49}$$

the third-order susceptibility $\chi^{(3)}(\omega_3; -\omega_1, -\omega_1, \omega_2)$ reads as

$$\chi^{(3)} = \frac{-N \cdot 2i|\mu_{eg}|^4/\hbar^3}{1/T_1 + i(\omega_2 - \omega_1)} \cdot \frac{1}{1/T_2 + i(\omega_0 - \omega_3)} \cdot \left[\frac{1}{1/T_2 - i(\omega_0 - \omega_2)} + \frac{1}{1/T_2 + i(\omega_0 - \omega_1)}\right]. \tag{2.50}$$

Here, N denotes the number density of two-level systems per unit volume. For the degenerate case of $\omega = \omega_1 = \omega_2$ the above equation becomes

$$\chi^{(3)} = -N\frac{4i|\mu_{eg}|^4}{\hbar^3} \cdot \frac{1}{1/T_2 + i(\omega_0 - \omega)} \frac{T_1/T_2}{1/T_2^2 + (\omega_0 - \omega)^2}. \tag{2.51}$$

Apparently $\chi^{(3)}$ is enhanced at the vicinity of the resonance. When $\omega = \omega_0$, $\chi^{(3)}$ is expressed as:

$$\chi^{(3)} = -i\frac{4N|\mu_{eg}|^4}{\hbar^3} \cdot T_1 T_2^2 \quad . \tag{2.52}$$

Consequently, $\chi^{(3)}$ is governed by the four intrinsic parameters: number density of the two-level systems, the longitudinal relaxation time, the transverse relaxation time (which is related to the homogeneous width Γ_h, $\Gamma_h = \hbar/T_2$) and the dipole moment μ_{eg}. The linear absorption coefficient $\alpha(\omega)$, for comparison, is expressed as

$$\alpha(\omega) = N \cdot \frac{4\pi|\mu_{eg}|^2}{n_0\hbar c} \cdot \frac{\omega/T_2}{(\omega - \omega_0)^2 + 1/T_2^2}. \tag{2.53}$$

Here n_0 is the refractive index. Note the higher order of μ_{eg} in Eq. (2.50) than in Eq. (2.53), which reflects the higher-order character of light-matter interaction for $\chi^{(3)}$.

Chapter 3

Experimental

3.1 Sample preparation and characterization

3.1.1 Preparation of nanocrystals embedded in glass

Samples of CuBr and $CuBr_xCl_{1-x}$ nanocrystals embedded in glass matrix were obtained by the double heat-treatment procedure of borosilicate glasses doped with CuBr and CuCl. [34, 35] The composition of the glass is listed in Table 3.1. The constituents were

Table 3.1: Composition of glass doped with copper (I) halide nanocrystals (mol%)

SiO_2	B_2O_3	Na_2CO_3	Al_2O_3	SnO	CuBr	CuCl	NaBr	NaCl
30	52.5	7.5	7.5	0.5	x	1-x	10x	10(1-x)

molten in Al_2O_3 crucibles at 1300°C for one hour in a furnace. The melt was rapidly quenched by pouring onto a steel plate, resulting in clear glass sheets with a slightly yellowish appearance for a sample thickness of several millimeters. The glass sheet was cut into pieces of about 1cm-square by a diamond band sawing machine. Then the pieces of glass were annealed at temperatures of 450 - 600°C for 30 minutes to several days to promote the nucleation and growth of nanocrystals. Finally the platelets were polished to thickness of about $100 - 300$ μm for optical measurements.

3.1.2 Characterization of samples using X-ray diffraction methods

Experiment setup

The characterization of nanocrystals, including the mean radius, crystal structure and composition ratio of the as-grown CuBr or $CuBr_xCl_{1-x}$ nanocrystals, was performed by using the X-ray diffraction (XRD) methods. For most of the CuBr and $CuBr_xCl_{1-x}$

nanocrystals, the synchrotron radiation (SR) light source at the Photon Factory in Tsukuba was utilized. As shown in Fig. 3.1, the synchrotron radiation ($1\mathring{A}$) monochromatized by the Si crystal was exposed onto the glass sample. The diffraction signal was recorded by the two-dimensional imaging plate. The high intensity SR light and the two-dimensional imaging plate made the measurement of wide angle diffraction possible to finish within one hour with a satisfactory S/N ratio. Those experiments were carried out by Dr. Takata and his collaborators. For some of the $CuBr_xCl_{1-x}$ nanocrystals, especially those of $x = 0.97$ and $x = 0.11$ and some CuBr nanocrystals, the conventional X-ray diffraction measurements were performed utilizing the CuKα ($\lambda = 1.542\mathring{A}$) radiation from the Rigaku (RAD-3A 1 kW, and/or RAD-C 20kW) X-ray source.

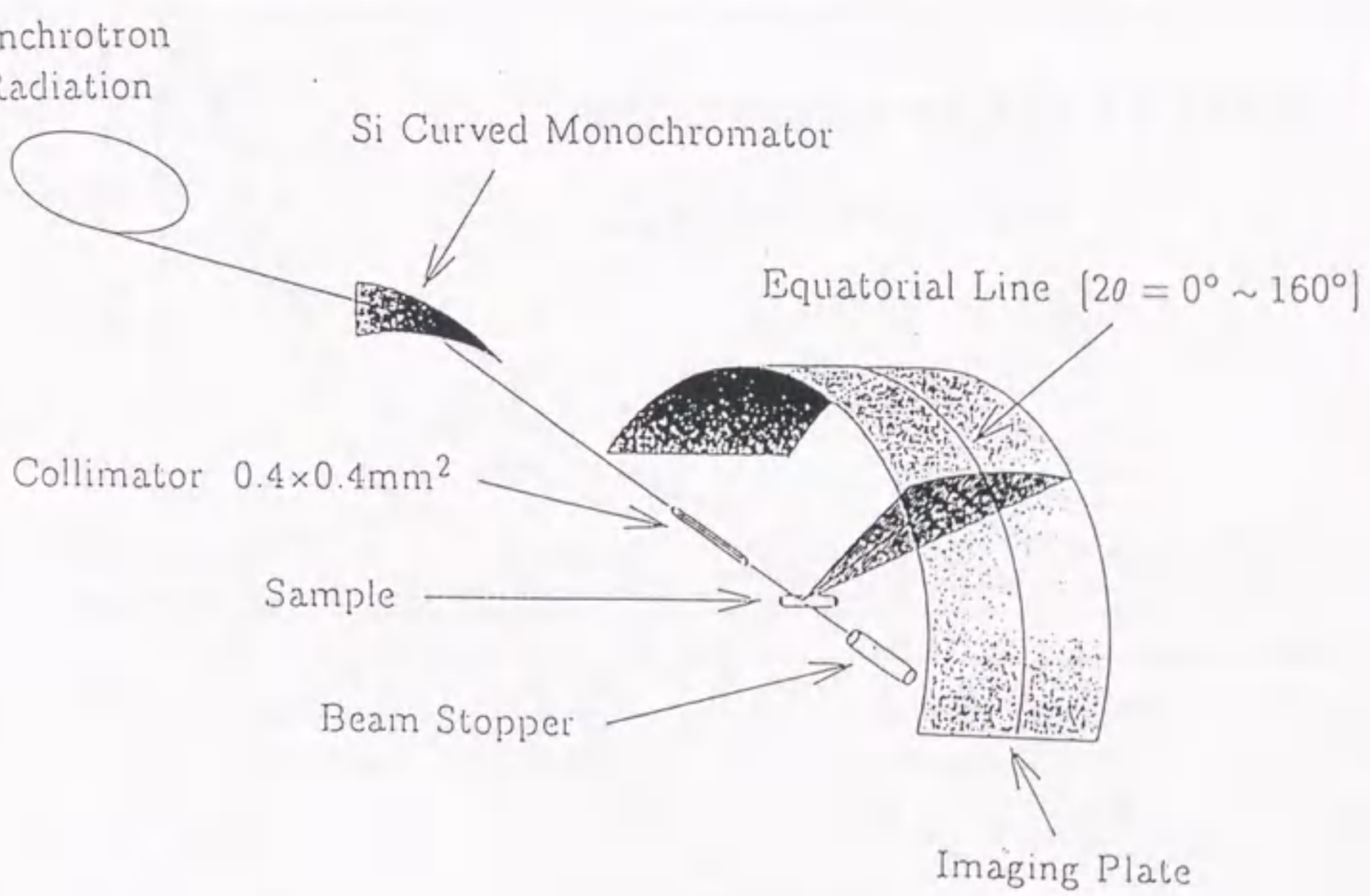

Figure 3.1: Experimental setup of X-ray diffraction at the Photon Factory of KEK.

Results of the sample characterization: lattice structures, sizes and composition ratios

Figure 3.2 shows the X-ray diffraction (XRD) pattern of a glass sample containing CuBr nanocrystals. A set of sharp diffraction peaks can be distinguished on the rather slowly varying background of the matrix glass halo. The diffraction angles and the relative intensities of these peaks correspond well to those of bulk CuBr with zincblende structure, but the full widths at half maximum (FWHM) of them are considerably broader than the resolution. They are hence assigned to be the diffraction pattern of CuBr nanocrystals. From the diffraction angles, the lattice constant was obtained by using Cohen's method. [36] The result is $5.683 \pm 0.006 \mathring{A}$, consistent with the bulk value of $5.691 \mathring{A}$. This indicates that the obtained CuBr nanocrystals have the same lattice structure as the bulk.

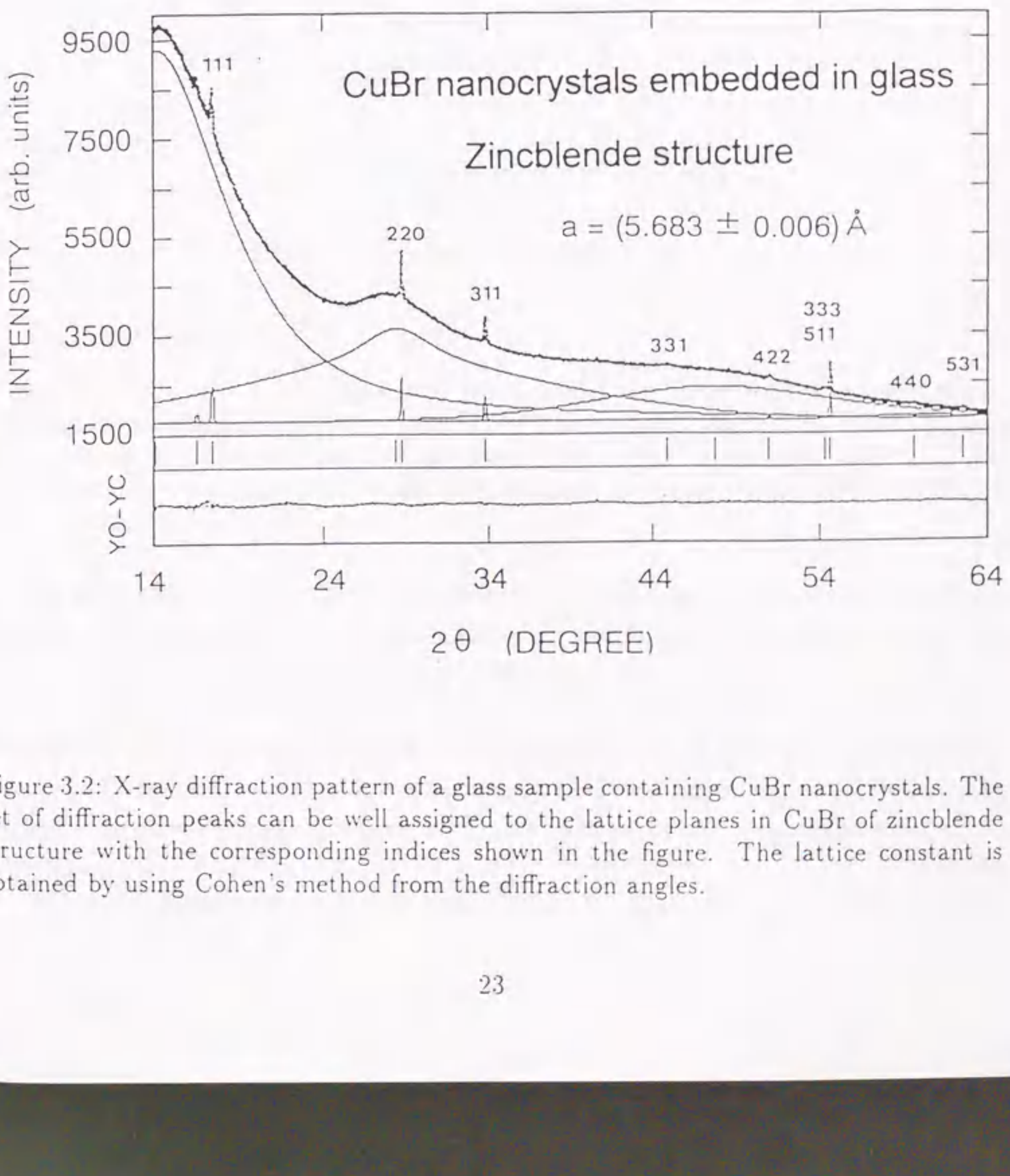

Figure 3.2: X-ray diffraction pattern of a glass sample containing CuBr nanocrystals. The set of diffraction peaks can be well assigned to the lattice planes in CuBr of zincblende structure with the corresponding indices shown in the figure. The lattice constant is obtained by using Cohen's method from the diffraction angles.

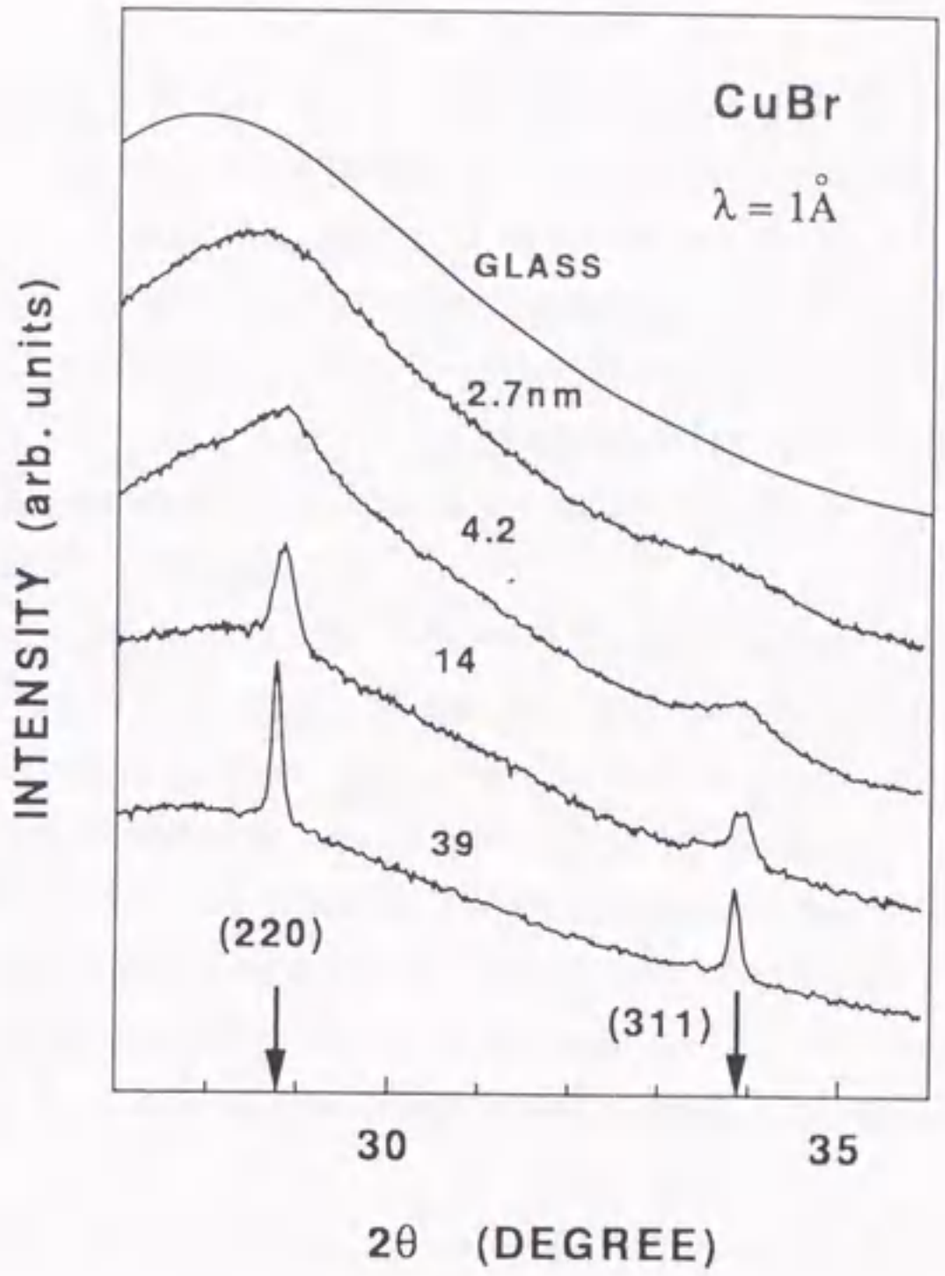

Figure 3.3: X-ray diffraction patterns of glass samples containing CuBr nanocrystals with different crystallite radii and an untreated base-glass sample. Two vertical arrows indicate the positions of diffraction peaks arising from (220) and (311) planes in bulk CuBr with the zincblende structure. The mean radii obtained by using the Scherrer formula are shown in the figure.

Figure 3.3 shows the XRD patterns between 27° and 36° for four CuBr-doped glass samples prepared under different heat-treatment conditions and a base-glass sample without the heat treatment. Distinguishable diffraction peaks which are superimposed on the broad halo pattern due to the matrix glass are seen at 28.78° and 33.88° for all the heat-treated samples. Two vertical arrows indicate the diffraction angles from (220) and (311) planes in CuBr bulk crystal with the zincblende structure. Again, one can see the agreement of the observed peak positions with that of bulk crystal is satisfactory for all the samples.

The mean radius of nanocrystals is estimated from the broadening of diffraction pat-

tern by using the Scherrer formula,

$$R = \frac{2}{3} \cdot \frac{0.9\lambda}{w \cos\theta} , \tag{3.1}$$

where λ is the wavelength of the X-ray radiation, θ and w are the diffraction angle and the full width at half-maximum (FWHM) of the diffraction peak, respectively. [37] The factor 2/3 takes into account the spherical shape of nanocrystals. The evaluation of θ and w was carried out by the careful least-squares profile fitting, which was applied to separate the diffraction patterns of nanocrystals from those due to the glass. Diffraction profiles of (220) and (311) were fitted to the Gaussian function with the same broadening parameter w, and the parameter w was determined within a fitting error of 10%. The obtained radii are shown in the figure.

The above method of data analysis measures the size of the coherent volume, i.e., ideal lattices without stacking fault. Any incoherent factors, like the lattice stacking fault or surface lattice relaxation etc., may also give rise to the width of the diffraction profile, and result in the error of the size estimation. In order to further confirm the reliability of the obtained radius, the two samples (R=4.2 and 14 nm) were further set to small angle X-ray scattering measurements. The mean radii obtained by the small angle X-ray scattering (SAXS) method turned out to be 4.2 nm and 15 nm, respectively. (Table 3.2.) The radii determined by both methods agree well within the experimental error of 10%.

Table 3.2: Comparison of nanocrystal mean radii obtained by XRD and SAXS. All is in unit of nanometer.

SAMPLE	XRD	SAXS
A	4.2	4.2
B	14	15

The nanocrystal size determined by the XRD method could have been compared to that determined by the transmission electron microscopy (TEM). Unfortunately the nanocrystals were found to be growing under the exposure of electron beams, and hence the TEM observation failed to apply for measuring sizes of copper halide nanocrystals. The accuracy of the size estimated by the X-ray diffraction method has been known to be good. [38] Sizes of CdSSe nanocrystals in glasses determined by means of the high resolution transmission electron microscopy (HRTEM) are in good agreement with those determined by smaller angle X-ray scattering (SAXS) within an error of 20%. [39] (See Table 3.3.)

Figure 3.4 shows the X-ray pattern of $CuBr_xCl_{1-x}$ nanocrystals with different composition ratios and sizes. The dotted (broken) lines indicate the diffraction angles of (220)

Table 3.3: Composition of crystallite sizes for three CdSSe samples by HRTEM and SAXS. S_{eff} is the effective size for the cubic nanocrystals obtained from HRTEM and D_s is the diameter of spherical nanocrystals by SAXS. (After Ref. [39].)

SAMPLES	HRTEM S_{eff}(nm)	SAXS D_s(nm)
A	5.5	7.8
B	8.8	11
C	16.4	16.2

and (311), respectively, for the bulk CuBr (CuCl) crystal with zincblende structure. Since the lattice constant of CuBr and CuCl solid solution varies continuously with the composition ratio x, the diffraction angle also changes with x uniquely. The composition ratio x of $CuBr_xCl_{1-x}$ nanocrystals were determined from the measured lattice constant a by using the Vegard law

$$a = xa_{CuBr} + (1-x)a_{CuCl}, \tag{3.2}$$

where $a_{CuBr} = 5.691\mathring{A}$ and $a_{CuCl} = 5.416\mathring{A}$ [40]. The mean radius was measured by fitting the XRD pattern to estimate the broadening width due to finite size and using the Scherrer equation.

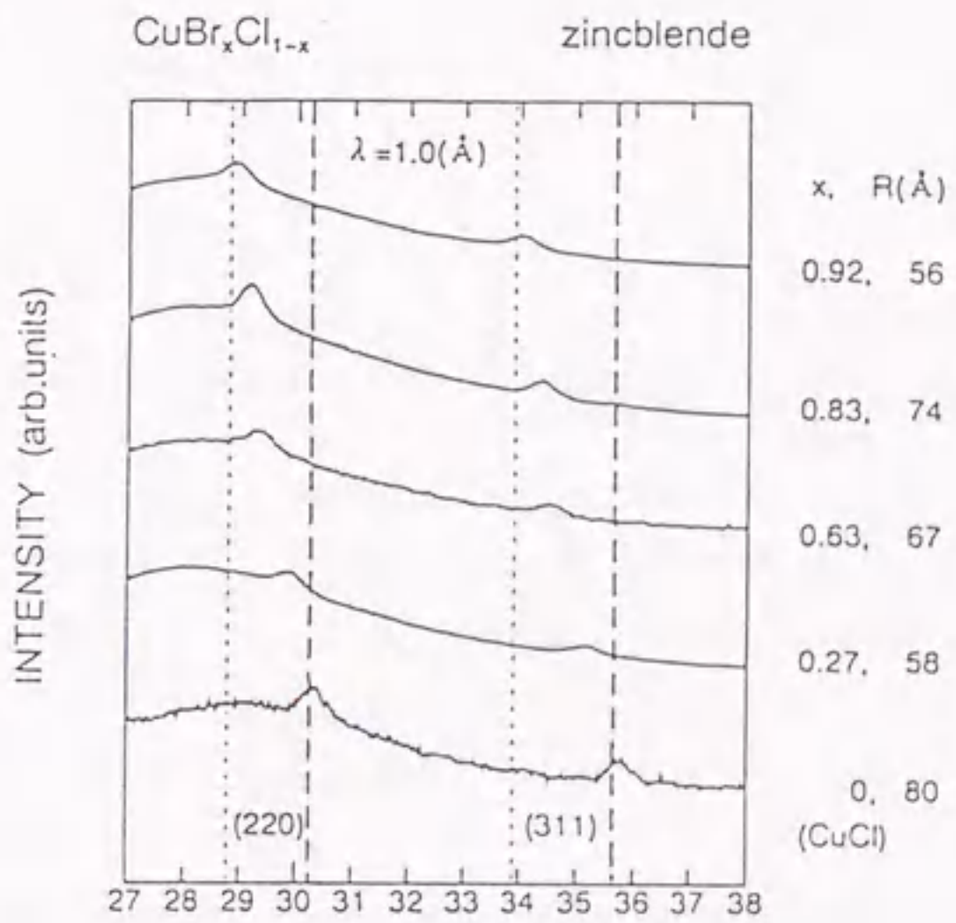

Figure 3.4: XRD pattern due to the zincblende (220) and (311) planes of $CuBr_xCl_{1-x}$ nanocrystals with different composition ratios. Dotted (broken) lines indicate the diffraction angle of bulk CuBr (CuCl).

3.2 Measurements of $\chi^{(3)}$ by degenerate four-wave mixing

3.2.1 Degenerate four-wave mixing

Degenerate four-wave mixing (DFWM) is a widely used experimental technique for investigation of the nonlinear susceptibilities and the dynamical properties of nonlinearity in semiconductors.[41, 42, 43] DFWM refers to the third- or higher-order nonlinear optical process involving four electromagnetic waves interacting with each other. In DFWM experiments there are four geometrical configurations as shown in Fig. 3.5. The two-beam configuration was adopted in this work.

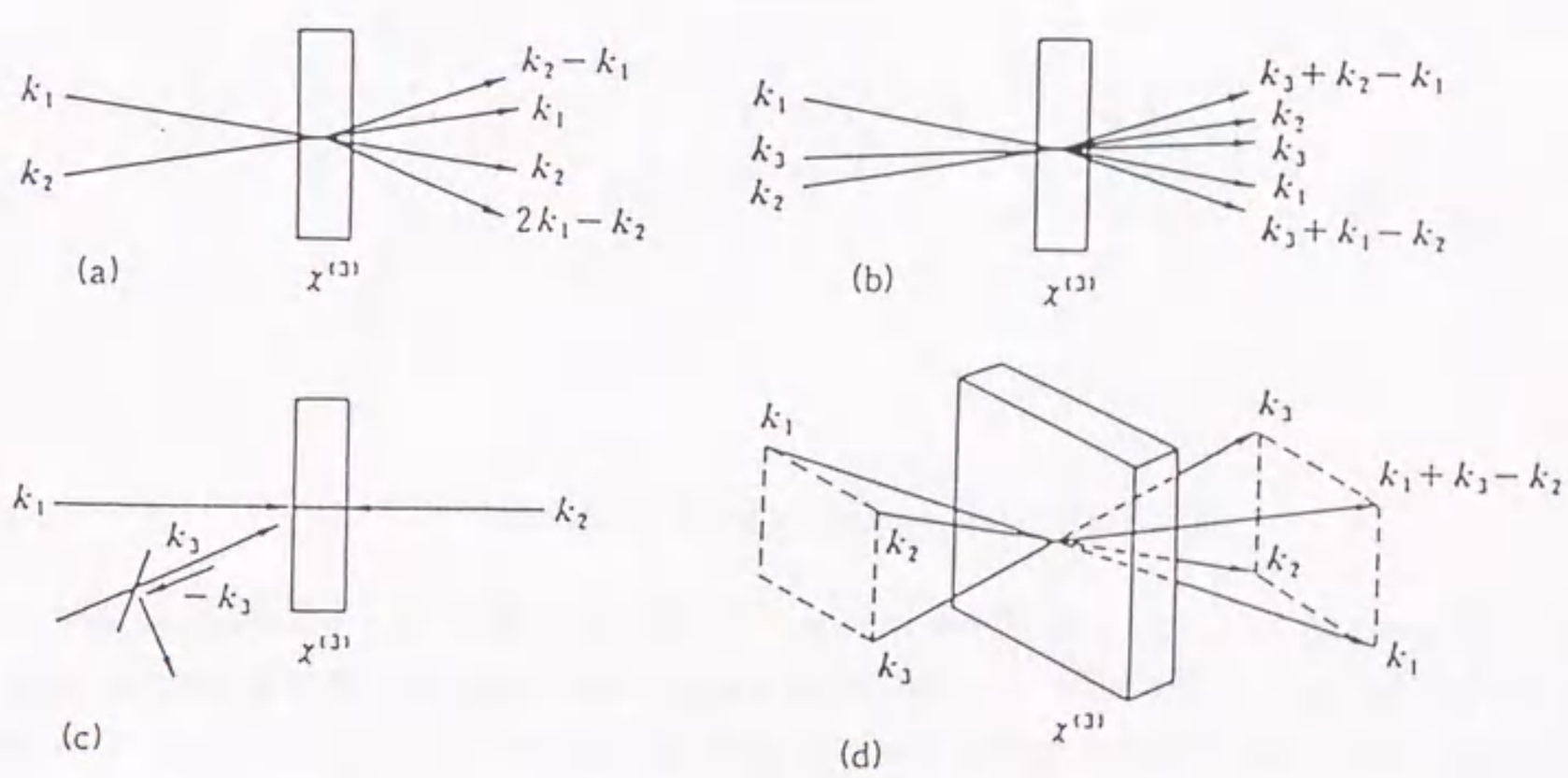

Figure 3.5: Four different configurations for DFWM experiments.

In the two-beam configuration of DFWM experiment, a grating due to the interference of polarization is created by illuminating a sample with two copropagating input beams of equal frequency at a small crossing angle θ_0 (Fig. 3.6). The photon excitations result in

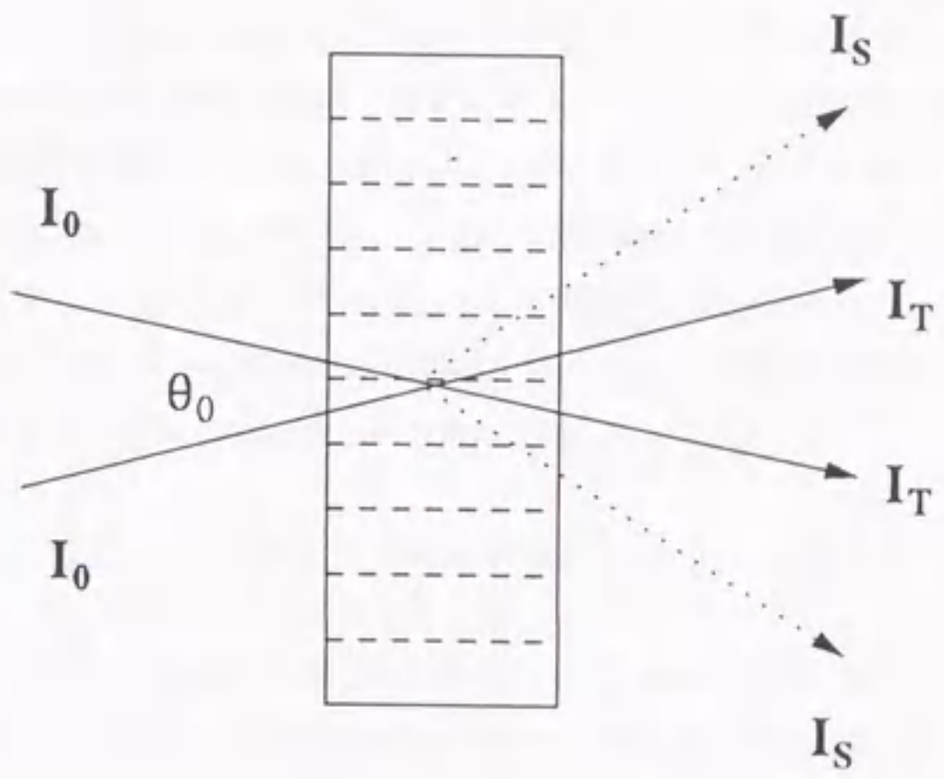

Figure 3.6: 2-beam forward configuration of DFWM.

the changes of the refractive index Δn and absorption coefficient $\Delta\alpha$, and hence a spatial grating is formed which diffracts the incident laser beams. The diffraction efficiency η, defined as $\eta = I_s/I_0$ where I_0 is the intensity of laser beam incident on the surface of sample and I_s is the diffraction signal intensity, is relevant to the modulus of $\chi^{(3)}$, and depends on the temporal behavior of the grating within the laser duration. One can estimate $\chi^{(3)}$ through η with the following procedure.

For the *cw* case, i.e., under the excitation of continuous wave light, a stationary grating is formed in the sample. η is given in the small signal limit by [44, 42]

$$\eta = \left[(\frac{2\pi}{\lambda}\Delta n)^2 + (\frac{1}{2}\Delta\alpha)^2\right] \cdot \frac{l^2}{4} exp(-\alpha l) \tag{3.3}$$

$$= (\sigma_{eff} N l)^2 exp(-\alpha l). \tag{3.4}$$

Here, α is the absorption coefficient and l is the thickness of sample. σ_{eff} is known as

the nonlinear absorption cross section, which is related to the modulus of the third-order nonlinear susceptibility $|\chi^{(3)}|$ and the carrier lifetime τ by

$$|\chi^{(3)}| = \frac{n^2c^2}{8\pi^2\omega} \cdot \frac{\alpha\tau}{\hbar\omega} \cdot \sigma_{eff}. \tag{3.5}$$

N is the carrier density determined by

$$\frac{dN}{dt} = \frac{1 - exp(-\alpha l)}{l\hbar\omega} I_0 - \frac{N}{\tau}, \tag{3.6}$$

for the single-exponential-decaying system. Therefore, the $\chi^{(3)}$ value can be related to the experimentally measured η through σ_{eff}, using Eq. (3.4) and (3.5).

For the general case where the time duration t_p of the pulse is comparable to or even shorter than τ, the above procedure remains effective if one treats $\eta, I_0, I_s, N, \Delta n, \Delta\alpha$ and σ_{eff} as time dependent parameters. The ultrafast transient case where the phase relaxation phenomena are involved when t_p becomes comparable to the phase relaxation time is not included in this discussion. Then, the time dependent scattering efficiency $\eta(t)$ due to the time-dependent grating, is given by [42, 45]

$$\eta(t) = \frac{I_s(l,t)}{I_i(0,t)} = [\sigma_{eff}N(t)]^2 \cdot \exp(-\alpha l), \tag{3.7}$$

where I_i denotes the incident laser beam intensity. Experimentally measured diffraction efficiency η_{obs} equals to the ratio of integrated signal energy with respect to the laser pulse energy, i.e.,

$$\eta_{obs} = \frac{\int_0^{t_p} I_s(t)}{\int_0^{t_p} I_i(t)} \tag{3.8}$$

$$= (\sigma_{eff}l)^2 exp(-\alpha l) \cdot \frac{\int_0^{t_p} I_i(t) \cdot N(t)^2}{\int_0^{t_p} I_i(t)}. \tag{3.9}$$

Therefore $\chi^{(3)}$ can be calculated using Eq. (3.5) and (3.9), once $N(t)$ is known through Eq. (3.6) with I_0 replaced by $I_i(t)$.

3.2.2 Formula for calculation of $\chi^{(3)}$

The single-exponential case

For the *cw* case where the pulse duration t_p of pumping light is much longer than the nonlinear response time T_1 involved, the value of $|\chi^{(3)}|$ in cgs/esu unit is calculated using the following formula:

$$|\chi^{(3)}| = \frac{n^2c}{32\pi^3} \frac{\alpha\lambda}{(1-T)\sqrt{T}} \sqrt{\frac{\eta_0}{I_0}}, \tag{3.10}$$

where c is the velocity in vacuum, n is the refractive index of sample. α and T are the absorption coefficient and transmittance at wavelength λ, respectively.

For the transient case, i.e., $t_p \ll T_1$, one must use the following equation to obtain a $|\chi^{(3)}|$ value which can be compared with the $|\chi^{(3)}|$ value for the *cw* case.[46]

$$|\chi^{(3)}| = \frac{n^2 c}{32\pi^3} \frac{\alpha\lambda}{(1-T)\sqrt{T}} \sqrt{\frac{\eta_{obs}}{I_0}} \cdot \beta \frac{T_1}{t_p}. \tag{3.11}$$

Here, β is a dimensionless numerical constant, depending on the temporal shape of laser pulse. If the factor of $\beta T_1/t_p$ is not taken into account (i.e., Eq. (3.10)), the estimated $\chi^{(3)}$ value from the measured η_{obs} under the condition of $t_p \ll T_1$ is always smaller than that measured under the *cw* excitation condition ($t_p \gg T_1$). Such a $\chi^{(3)}$ value can be only referred to as an effective $\chi^{(3)}$ in the transient regime, because it is dependent on the ratio T_1/t_p as discussed in Reference[46].

The multi-exponential case

When the time response does not show a single exponential decay, both transient and *cw* gratings exist in the sample. When the decay kinetics is fitted to a three-component-exponential decay (Eq. (4.3)), one can write down $\eta(t)$ phenomenologically by assuming proper expressions for $N(t)$ and just follow Eq. (3.9). One may assume, for instance,

$$N(t) = a\exp(-\frac{t}{\tau_1}) + b\exp(-\frac{t}{\tau_2}) + c\exp(-\frac{t}{\tau_3}). \tag{3.12}$$

In this case an effective lifetime T_1^* is defined as

$$T_1^* = \frac{a\tau_1 + b\tau_2 + c\tau_3}{a+b+c}. \tag{3.13}$$

By using Eq. (3.9) one has the following equation which relates the observed diffraction efficiency η_{obs} to the diffraction efficiency η_0 in the stationary regime.

$$\eta_{obs} = \frac{\eta_0}{T_1^{*\,2}} \times \frac{1}{t_p}\int_0^{t_p} dt\{\int_0^t dt\prime \frac{a\exp[-(t-t\prime)/\tau_1] + b\exp[-(t-t\prime)/\tau_2] + c\exp[-(t-t\prime)/\tau_3]}{a+b+c}\}^2, \tag{3.14}$$

where the incident laser pulse is assumed to be a rectangular pulse with temporal duration of t_p. The first integral on $t\prime$ from 0 to t describes the rise up of $N(t)$, and the second integral on t from 0 to t_p accounts for the accumulation of diffraction signal detected within the laser pulse duration. The $\chi^{(3)}$ value can be calculated using Eq. (3.14) and (3.10).

The transformation of an effective $\chi^{(3)}$ to a stationary $\chi^{(3)}$ based on Eq. (3.10) and (3.14) was experimentally confirmed using CdS_xSe_{1-x} nanocrystals in glass for which measurements were done in the visible light region.[47] The transient DFWM signal measured by the 3-beam boxcars configuration (see Fig 3.5) using a picosecond laser with the duration of 7 ps, exhibits a two-component decay with time constants(relative intensity)

of 400 ps(1) and 1000 ps(0.01), and the effective lifetime T_1^* is 406 ps. The diffraction efficiency, η_{ps}, measured using the 7 ps-pulse laser is 5.2×10^{-9}, which is much smaller than $\eta_{ns} = 2.3 \times 10^{-5}$ measured using the 7 ns-pulse laser at the same excitation level of 10kW/cm^2. If we use Eq. (3.10), the value of η_{ps} yields 2.3×10^{-8}esu for $|\chi^{(3)}_{ps}|$, while the value of η_{ns} yields 1.5×10^{-6}esu for $|\chi^{(3)}_{ns}|$. However, using Eq. (3.10) and (3.14), we obtain $|\chi^{(3)}_{ps}| = 2.3 \times 10^{-6}$esu for η_{ps}. This value is in good agreement with the $\chi^{(3)}_{ns}$ value measured in the stationary regime within a factor 1.5. If we put directly η_{ps} and T_1^*=406 ps into Eq. (3.11), we can get the same value. Therefore, we can derive a stationary $\chi^{(3)}$ value which characterizes nonlinear properties of materials using Eq. (3.10) and (3.14) even if there exists a multi-component decay in the nonlinear time response. It is worthwhile to point out that when we use a standard reference sample such as CS_2, response times of both the reference sample and the sample in study must be much shorter than the pulse width used.[48] Only when the stationary grating in the DFWM configuration is generated for both of the samples, do the measured diffraction efficiencies yield the stationary $\chi^{(3)}$ values.

3.2.3 Experimental setup of DFWM

The absolute values of $\chi^{(3)}$ were measured by degenerate four-wave mixing with the 2-beam configuration as shown in Fig. 3.7. [35] A XeCl excimer-laser pumped dye (PBBO and BBQ) laser (Lambda Physics FL3000) was used with the laser pulse width of 20 ns operating at a repetition rate of 10 Hz. The laser beam is split into two collimated beams of same intensity by a Michelson interferometer. The two laser beams attenuated by the neutral density filter were focused onto the sample at a crossing angle of about 1.1°, which corresponds to the Raman-Nath regime.[49] The spatially separated diffraction signal was then collected by a photomultiplier and the signal averaged by a boxcar integrator was recorded on a pen recorder. The pumping laser intensity was reduced to the level (about 20 kW/cm^2) low enough to ensure that the detected nonlinearity is due to the third-order nonlinear polarizability.

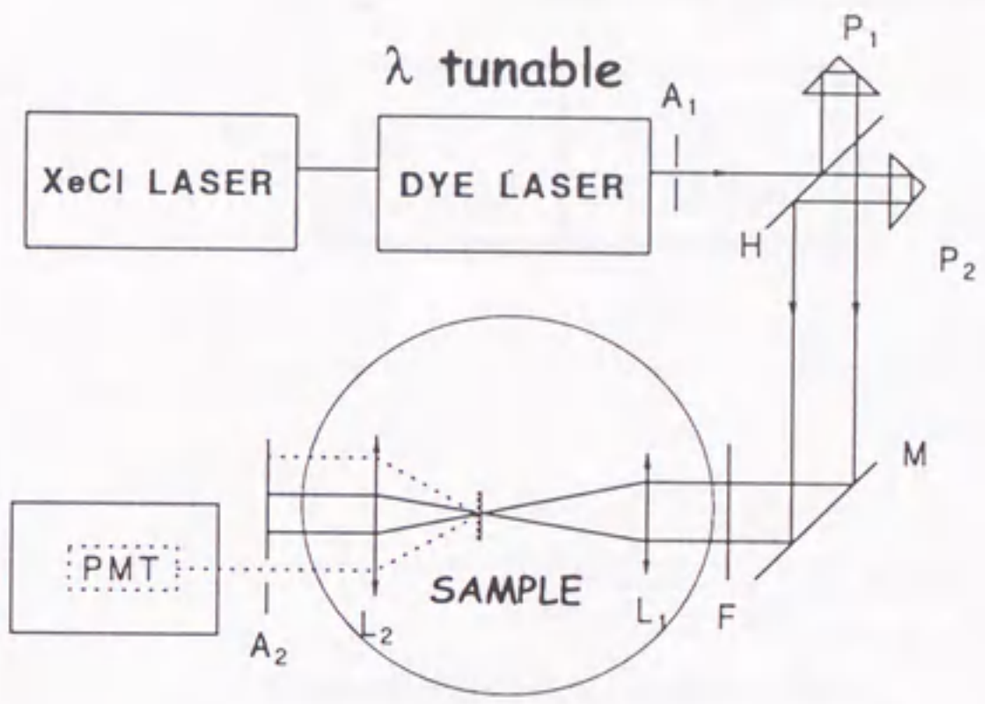

Figure 3.7: Schematic of the DFWM experimental setup in two-beam configuration for measurements of $\chi^{(3)}$. Prisms P_1 and P_2 and half mirror H provide the parallel beams of equal intensity. M is the mirror and F is the neutral density filter. L_1 and L_2 are lenses. Apperture A_1 is for modification of laser beam quality and A_2 is used as a spatial filter.

3.3 Measurements of relaxation parameters

3.3.1 Measurements of longitudinal relaxation time T_1

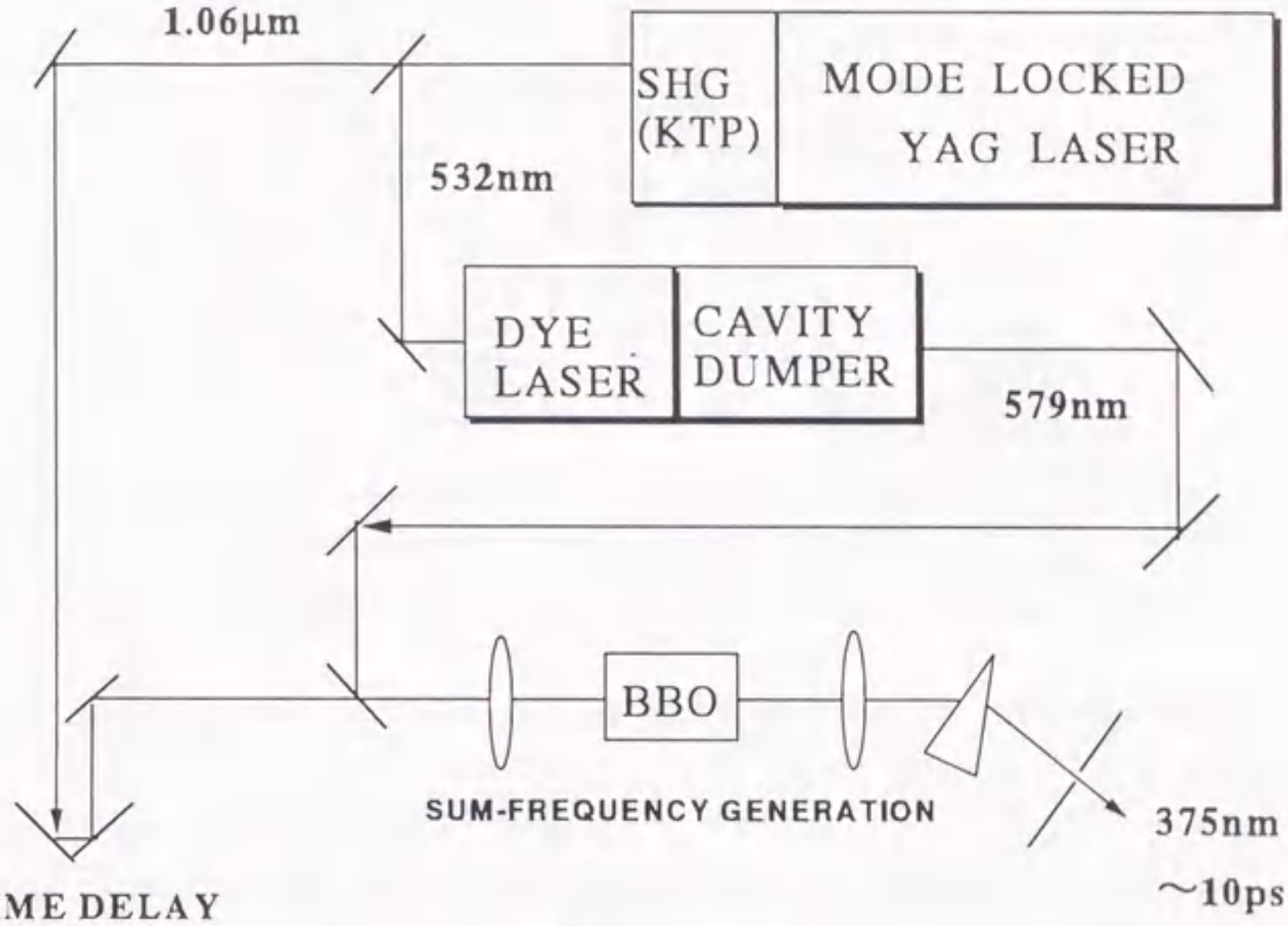

Figure 3.8: Excitation source for measurements of luminescence decays.

The longitudinal relaxation time T_1 of the Z_{12} excitons in CuBr nanocrystals was determined from the luminescence decay kinetics measured by utilizing a picosecond pulse laser (Fig. 3.8) and a time-correlated single photon counting system(Fig. 3.9). The excitation light of 375 nm was generated by the sum frequency of 1.06 μm fundamental light and 579 nm dye laser output of a synchronously mode-locked dye laser (R6G) pumped by a mode-locked Nd:YAG laser (532 nm). The pulse width was about 10ps, and the repetition rate was dumped to $0.8 - 4$ MHz. The second harmonic generation (SHG) of the Ti:Al_2O_3 laser (about 380 nm) , with repetition rate of 76 MHz and pulse width of about 200 fs, was employed for lifetime measurements of $CuBr_xCl_{1-x}$ nanocrystals. A Hamamatsu photo-multiplifier tube equipped with multi-channel-plate (MCP) was used. The deconvolution of luminescence decay curve with the apparatus response of laser pulse

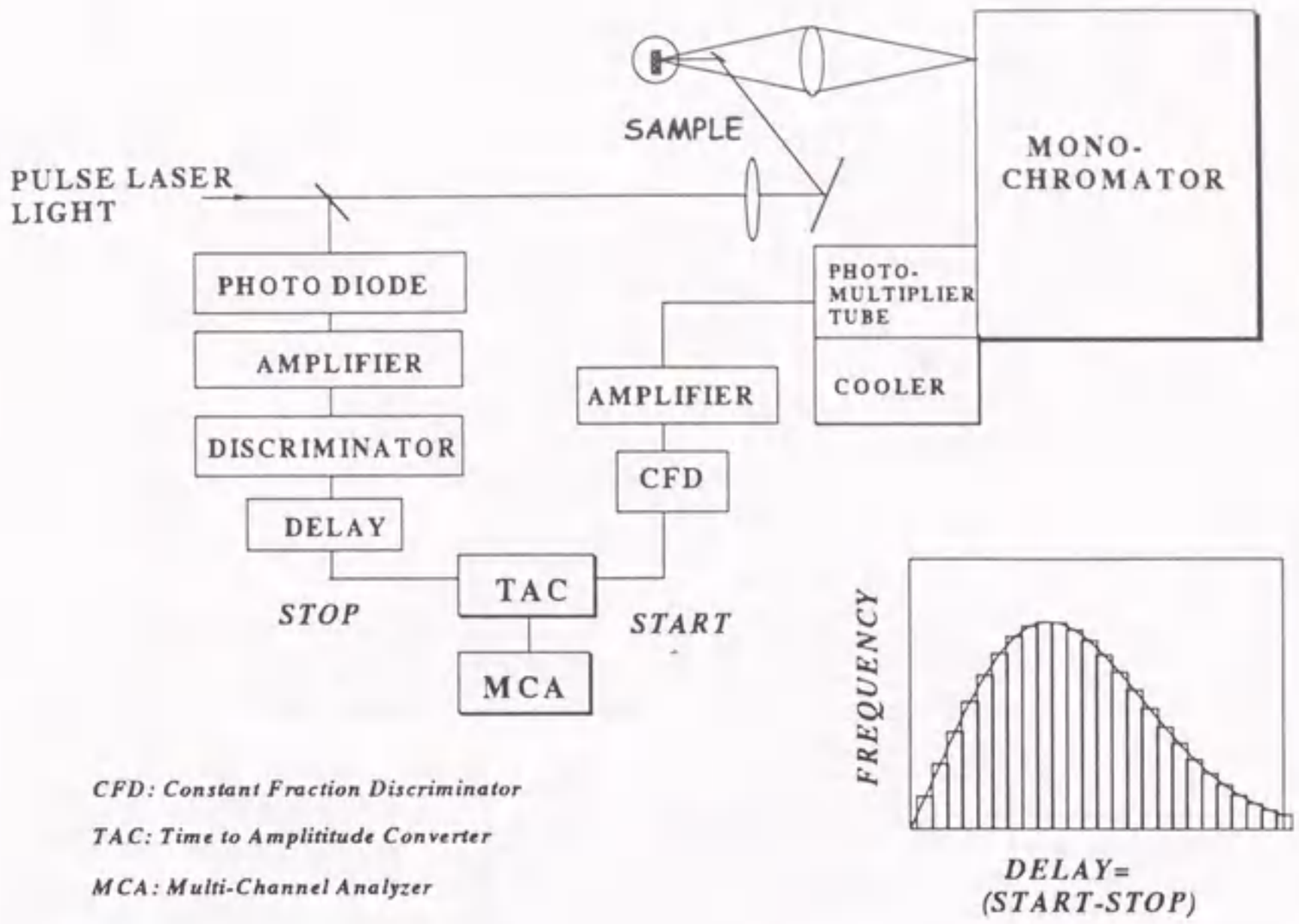

Figure 3.9: Schematic diagrams of the time-correlated single photon counting system.

yielded the time resolution of about 20 ps.

For some $CuBr_xCl_{1-x}$ (x=0.97) nanocrystals, the luminescence decay time is too short to be detected by the time-resolved luminescence measurements. The pump-probe technique was employed to measure the exciton lifetime. (Fig. 3.10) The fundamental output of a mode-locked Ti:Al_2O_3 laser (832 nm, 200 fs) amplified by a regenerative amplifier was frequency doubled to generate ultraviolet pulse light, which was split into two beams. One of the beam was attenuated (to 1/20 of the pump beam intensity) to serve as a probe beam. The central wavelength of the pulse laser light(spectral width $\sim$ 20 meV) was tuned to the exciton absorption peak ($\sim$416 nm), and the transmitted probe light was spectrally resolved at a resolution of $\sim$ 1 meV using a monochromater. The decay of the transimittance light (at 416 nm) was measured by changing the delay time between the pump and probe light pulses. The cross-modulation technique with chopping frequencies of 10 and 20 Hz for lock-in detection was utilized to improve the signal-to-noise(S/N) ratio. [50]

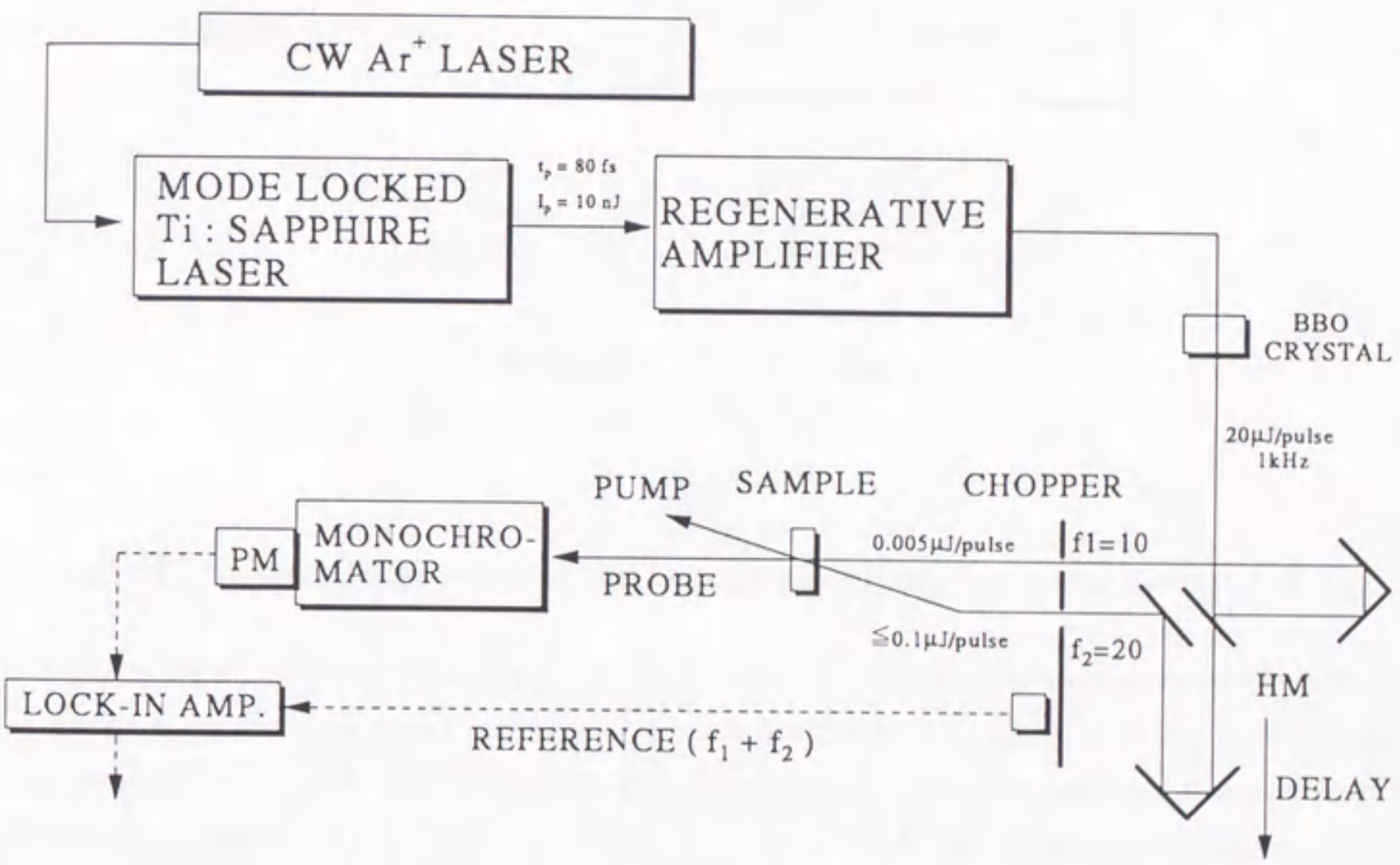

Figure 3.10: Experiment setup of the pump and probe measurement.

3.3.2 Measurements of homogeneous width Γ_h

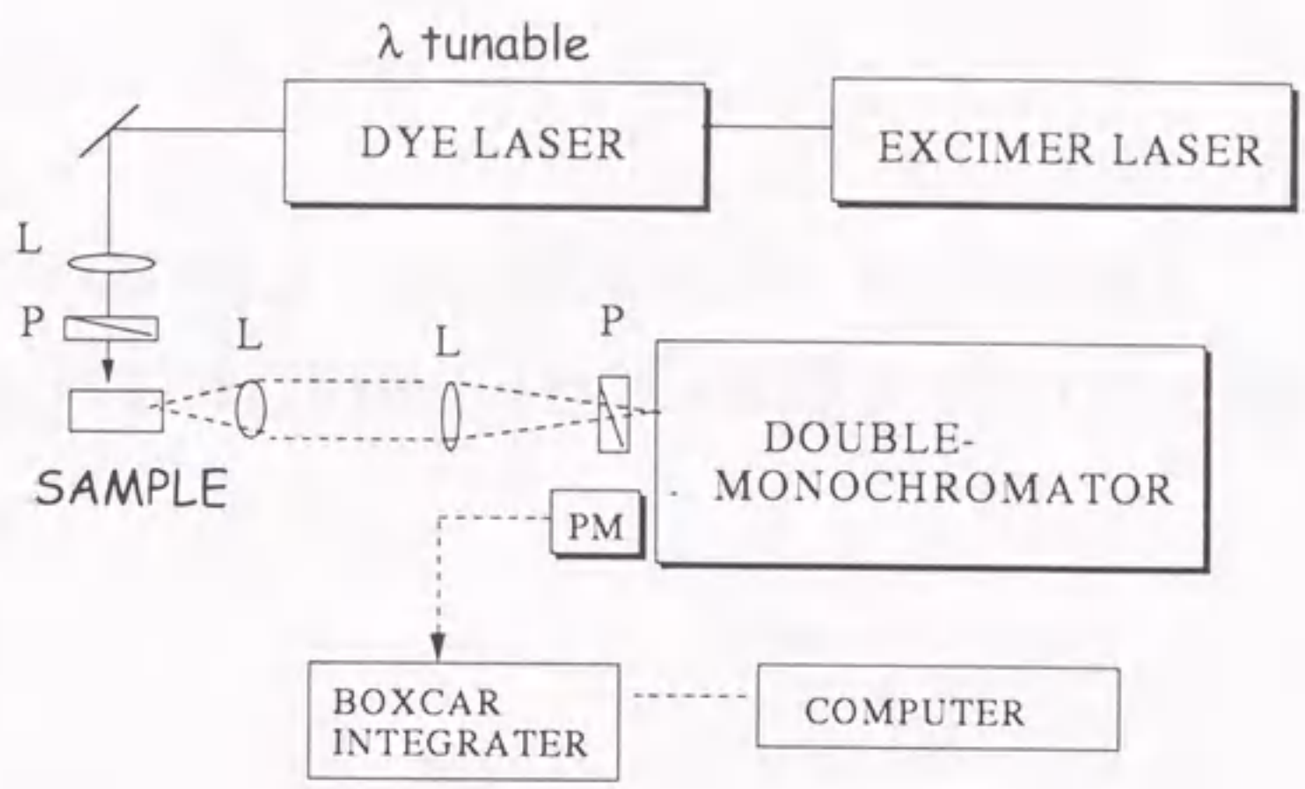

P: Polarizer L: Lens

Figure 3.11: Experimental setup of the resonant luminescence measurements of Γ_h.

The resonant luminescence measurements were used to obtain the homogeneous width Γ_h of Z_{12} exciton band. The same laser in $\chi^{(3)}$ measurements was used working at the same excitation level (~ 20 kW/cm^2). Resonant luminescence was collected and focused into a double-monochromator (Jobin-Yvon U1000, $f = 1m$) with the spectral resolution of 0.4 meV. (Fig. 3.11) As the spectral width (0.02meV) of the laser light is much narrower than the absorption peak (usually larger than 10 meV) , the laser light is just at resonance with the exciton energy of nanocrystals with a certain size. The luminescence spectrum in the higher energy side of excitation energy corresponds to the resonant luminescence of the selectively excited nanocrystals. This spectrum should exhibit a Lorentzian shape, and the spectral width of the spectrum reflects the homogeneous width of the size-selected nanocrystals within the size distribution. When the inhomogeneous width is much larger than the homogeneous width, the half of the half width at half maximum (half of HWHM) of the resonant luminescence band corresponds to Γ_h. [51] Thus Γ_h is obtained by fitting the measured spectrum on the higher-energy side of the excitation energy to a Lorentz-function.

Chapter 4

Third-order nonlinear optical susceptibilities in CuBr nanocrystals

Preface

As mentioned in Chapter 1, the important role of the giant oscillator strength effect in the size enhancement of nonlinearity has been experimentally shown for CuCl nanocrystals. The $R^{2.2}$-dependence of f_x indicates the giant oscillator strength of coherently generated excitons in a nanocrystal. However, the saturation and decrease of f_x for larger sizes can not be explained by the two-level atomic model, and it has been left to be clarified. In this chapter, the size dependence and the origin of the nonlinear susceptibilities are investigated for CuBr nanocrystals. In CuBr, the exciton Bohr radius is 1.25 nm which is roughly twice that of CuCl, and one can investigate confinement effects and size dependence of $\chi^{(3)}$ over a wide range of crystallite sizes from the strong confinement regime to the weak confinement regime. The lowest exciton state in CuBr is the Z_{12} exciton consisting of light and heavy holes in the Γ_8 band, while that of CuCl is the Z_3 exciton coming from the Γ_7 band. In addition, a k-linear term in the Γ_8 band is not negligible in CuBr, and thus the Z_{12} exciton has a multi-component character.

4.1 Results

4.1.1 Quantum size effect

The absorption spectra of CuBr nanocrystals with various radii at 77 K are shown in Fig. 4.1. At the bottom of the figure is shown a spectrum for the bulk-like crystal. The two vertical downward arrows indicate the Z_{12} and Z_3 exciton absorption peaks from the lower energy side in bulk CuBr crystal. Two absorption bands around about 3.0 eV and 3.1 eV can be observed in all the spectra, and they correspond to the Z_{12} and Z_3 excitons in CuBr nanocrystals. Both the absorption bands exhibit a blue-shift broadening with

decreasing radii. The size-dependent behaviors of the absorption spectra can be classified

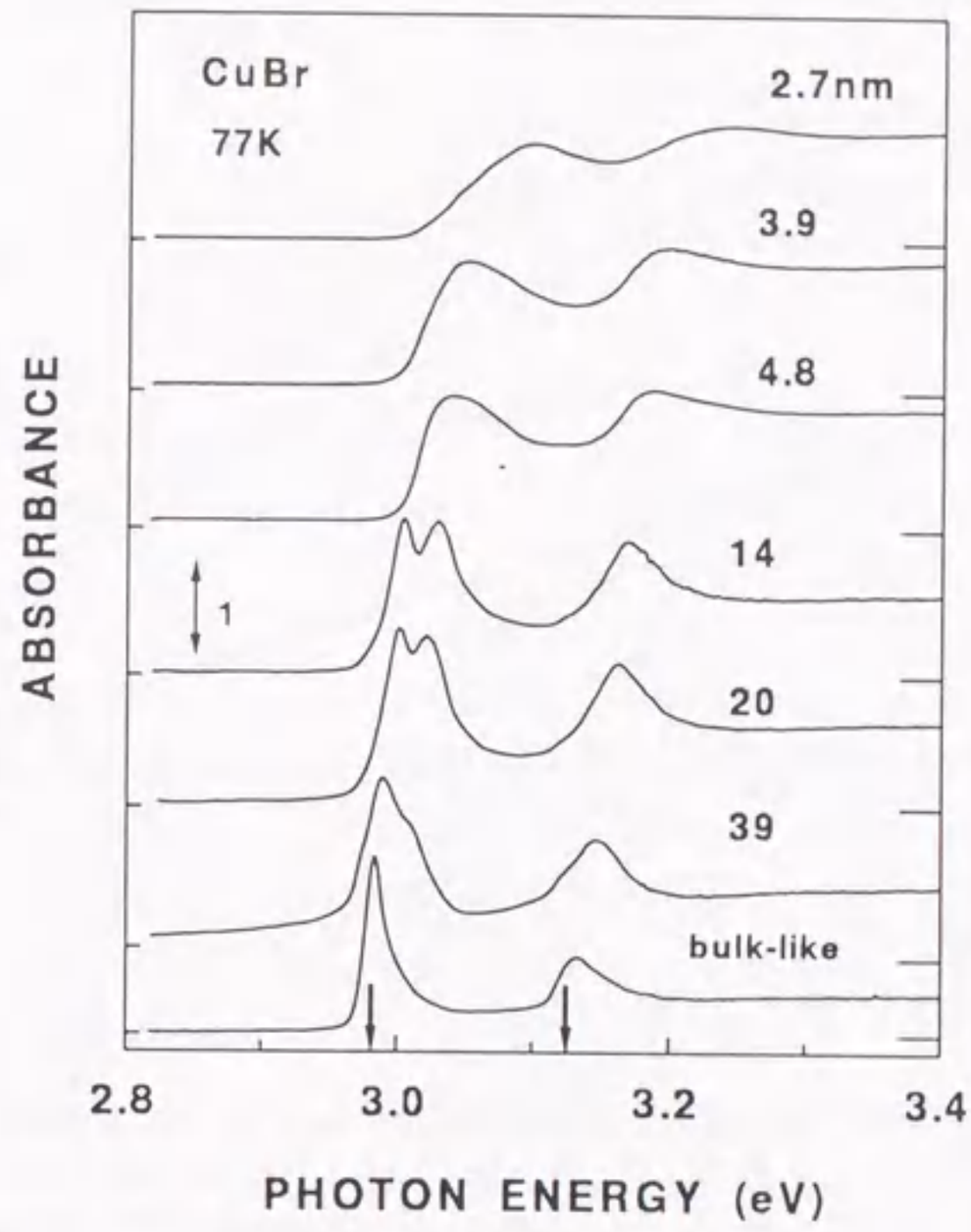

Figure 4.1: Absorption spectra of CuBr nanocrystals at 77 K. The vertical arrows indicate absorption energies of the bulk Z_{12} and Z_3 excitons.

into two regimes according to R. In the size range of $2.7 \leq R \leq 5.0$ nm, both the Z_{12} and Z_3 bands are shifted to the higher energy side by $50 \sim 120$ meV with decreasing radii. In the size range of $5.0 \leq R \leq 39$ nm, the absorption band due to Z_{12} excitons splits into two peaks with the energy separation of about 25 meV. The center of mass of the Z_{12} band shifts to the higher energy sides by $23 \sim 50$ meV upon a decrease of size. The splitting of Z_{12} band is not due to a size distribution because we cannot observe any obvious structure in the Z_3 band. It may be attributed to the splitting of light- and heavy-hole excitons. The blue-shift indicates the quantum confinement effect. However, the blue-shift, i.e., the confinement energy, does not follow R^{-2}-dependence given by the simple quantum mechanical calculation of the exciton confinement model (Eq. (2.12)).

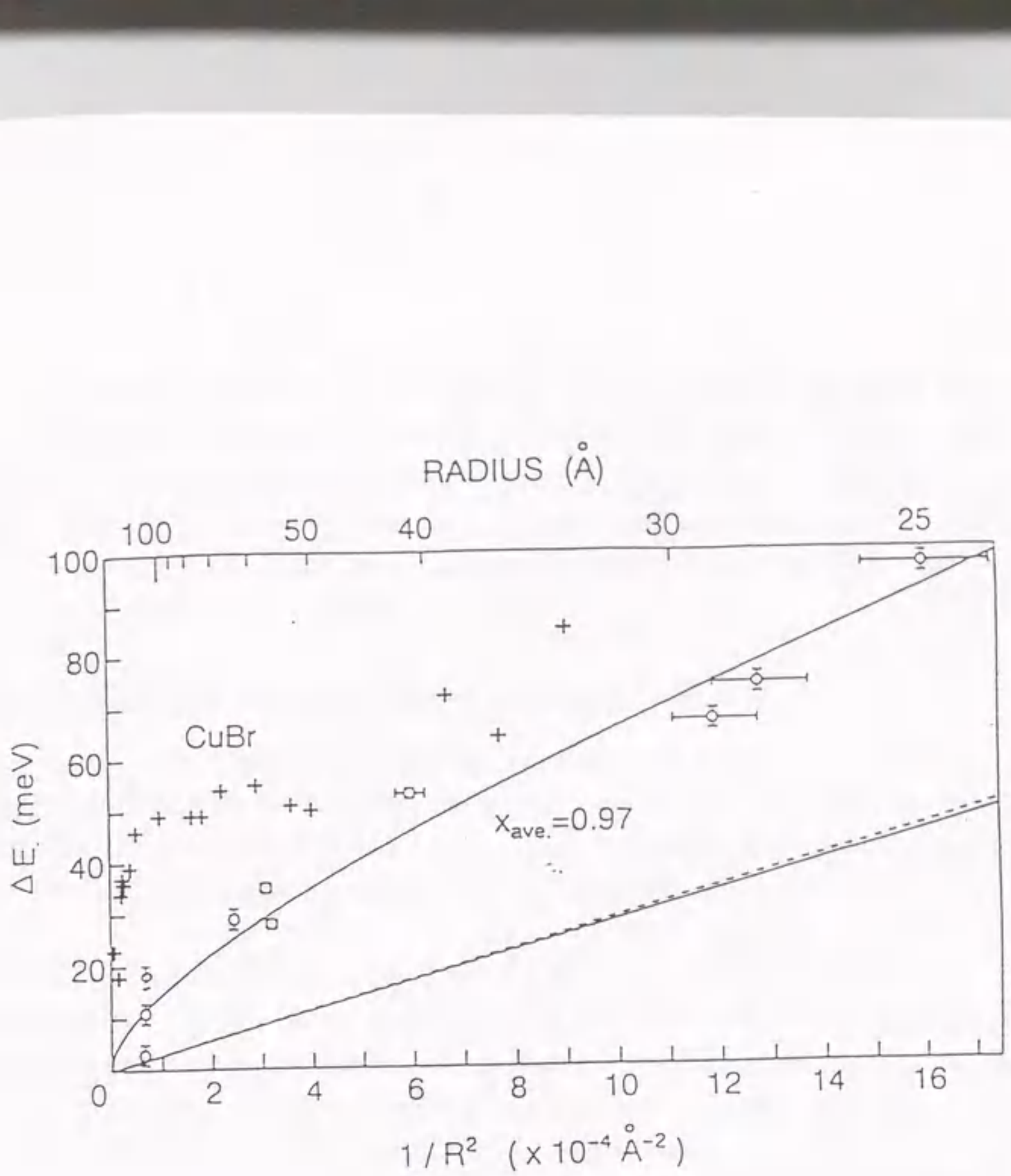

Figure 4.2: Size dependence of the confinement energy of Z_3 excitons in CuBr and $CuBr_xCl_{1-x}$ (x=0.97) nanocrystals. (+) CuBr, (o) $CuBr_xCl_{1-x}$ (x=0.97). The solid and dashed lines indicate the R^{-2}-dependence calculated by the simple exciton-confinement model.

A recent investigation on the R-dependence of the exciton energies, using nanocrystals of $CuBr_xCl_{1-x}$ solid solutions with different composition ratios, has revealed that the confinement energy generally exhibits a larger dependence than expected by the simple confinement model. [52] Figure 4.2 shows the confinement energy of the Z_3-exciton as a function of R^{-2} for both CuBr and $CuBr_xCl_{1-x}$ ($x = 0.97$) nanocrystals. [52] The solid and dashed lines indicate the R^{-2}-dependences given by the simple exciton confinement model. The large deviation from the R^{-2}-dependence for the confinement energy is obvious for both CuBr and $CuBr_xCl_{1-x}$ nanocrystals. As for the case of $CuBr_xCl_{1-x}$ nanocrystals, the confinement energy ΔE can be phenomenologically described by

$$\Delta E = \frac{\hbar^2\pi^2}{2MR^2} + \frac{A}{R}, \tag{4.1}$$

where A is a constant. The R^{-2}-term represents the contribution of the kinetic energy. The R^{-1} term suggests the contribution of a repulsive Coulomb potential. Similar sit-

uation occurs for other alloy nanocrystals ($x = 0.27, 0.49, 0.70$, and 0.83), and therefore the deviation from the simple exciton confinement model was attributed to the interface charges of copper halide nanocrystals in glass. [52] For CuBr nanocrystals, the size dependence of the confinement energy can be reprodued assuming that the coefficient A is size-dependent. The samples used in this study show the center of mass confinement, i.e., the weak confinement of exciton.

4.1.2 Third-order nonlinear susceptibility $\chi^{(3)}$

In order to confirm that the measured susceptibility is due to the third-order polarization, the excitation intensity dependence of the diffraction efficiency was measured. A quadratic-dependence is expected for the third-order nonlinearity polarization. Figure 4.3 shows the excitation intensity dependence of diffraction efficiency in DFWM experiments for CuBr nanocrystals with $R = 4.0$ nm at 77 K. η was measured at the absorption peak of Z_{12} excitons. The measured value exhibits the square dependence on the excitation intensity as shown by the dashed line up to the excitation level of 20 kW/cm^2, and starts to deviate from the dependence at higher excitation intensities. In this study the DFWM experiments were performed at the level low enough to show the square dependence which indicates that the third-order nonlinearity is involved. The $\chi^{(3)}$ value was estimated from the measurements at the excitation intensities within the range of the square dependence,for example below 20 kW/cm^2 in Fig. 4.3, and using Eq. (3.10) with $n = 1.5$ for the glass samples.

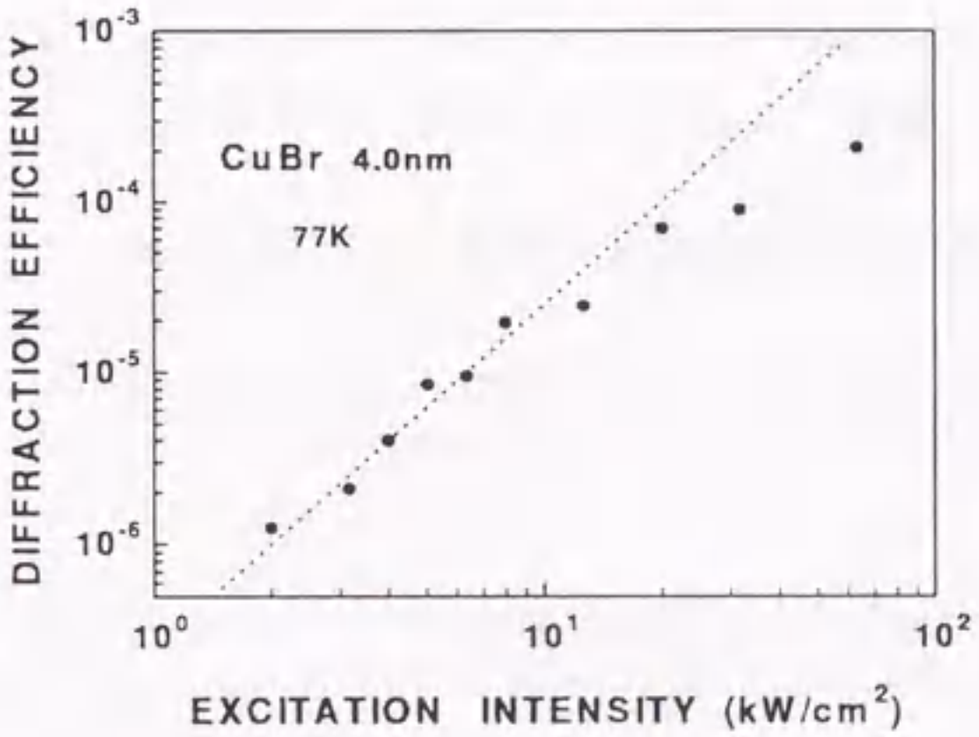

Figure 4.3: Excitation intensity dependence of diffraction efficiency in DFWM for CuBr nanocrystals with $R = 4.0$ nm. The dashed line indicates the square dependence.

To investigate the resonant behavior near the exciton resonance the $\chi^{(3)}$ values were measured at the vicinity of the Z_{12}- and Z_3-exciton absorption peaks. Figure 4.4 depicts the photon energy dependence of the absolute value of $\chi^{(3)}$ measured at 77 K for CuBr nanocrystals with various radii. The magnitude of $|\chi^{(3)}|$ shown by open circles is greatly

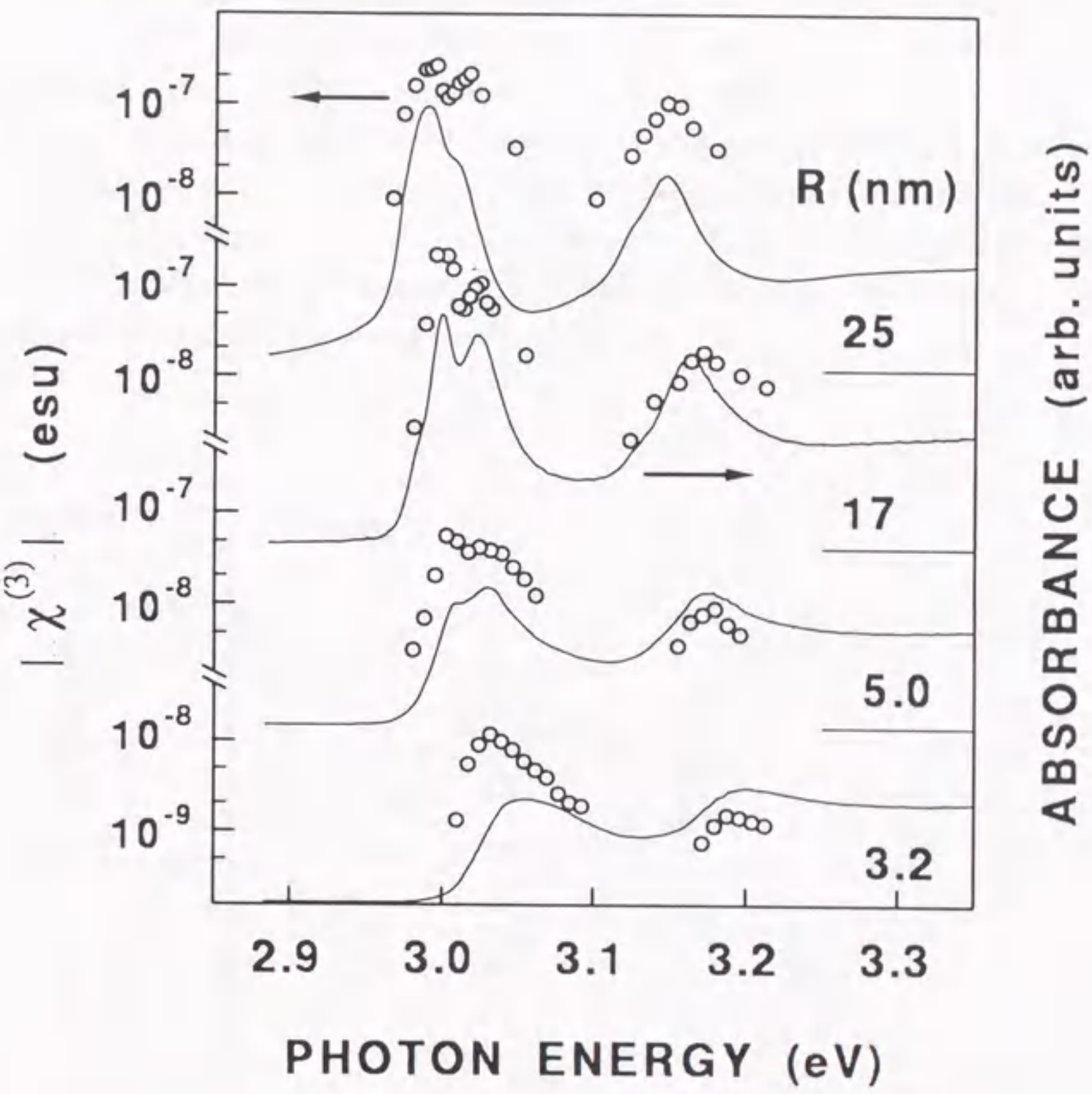

Figure 4.4: Photon energy dependence of $|\chi^{(3)}|$ for CuBr nanocrystals with different mean radii. Open circles and solid curves illustrate $|\chi^{(3)}|$ and the absorption spectra, respectively.

enhanced in the vicinity of the absorption peaks of Z_{12} and Z_3 excitons, indicating the resonant enhancement with the confined excitons. Note that $|\chi^{(3)}|$ is shown on a logarithmic scale and the width of $|\chi^{(3)}|$ is considerably narrower than the absorption band width. For $R = 25$ nm, $|\chi^{(3)}|$ exhibits clearly two maxima while in the absorption spectrum one peak and a shoulder are seen. The sharp resonant behavior of $|\chi^{(3)}|$ is consistent with the fact that the higher-order interaction between light and matter is involved in the third-

order nonlinear process compared to the absorption process. The value of $|\chi^{(3)}|$ at the resonance of Z_{12} excitons is strongly sample-dependent, and ranges from 8.3×10^{-9}esu to 2.6×10^{-7}esu for the samples shown in Fig. 4.4, which implies that $|\chi^{(3)}|$ is size-dependent.

In order to obtain the crystallite size dependence of the third-order susceptibility, one must take into account the difference in the number density of nanocrystals contained in the samples under measurements. Since the absorption coefficient is proportional to the number of nanocrystals in the sample, a value of $|\chi^{(3)}|/\alpha$ was used for the comparison between the different sizes. The R dependence of $|\chi^{(3)}|/\alpha$ measured at the absorption peak of Z_{12} excitons is shown in Fig. 4.5. The data show a general trend of increasing $|\chi^{(3)}|/\alpha$ values upon an increase of the radius, and the values range from 8.0×10^{-11} to 1.1×10^{-9} esu· cm for $R = 2.7 - 50$ nm. A size dependence of $R^{0.4}$ is obtained by the least-squares fit. There is, however, a noticeable scatter in the data, which implies that the $|\chi^{(3)}|$ is dependent on some parameters other than the size.

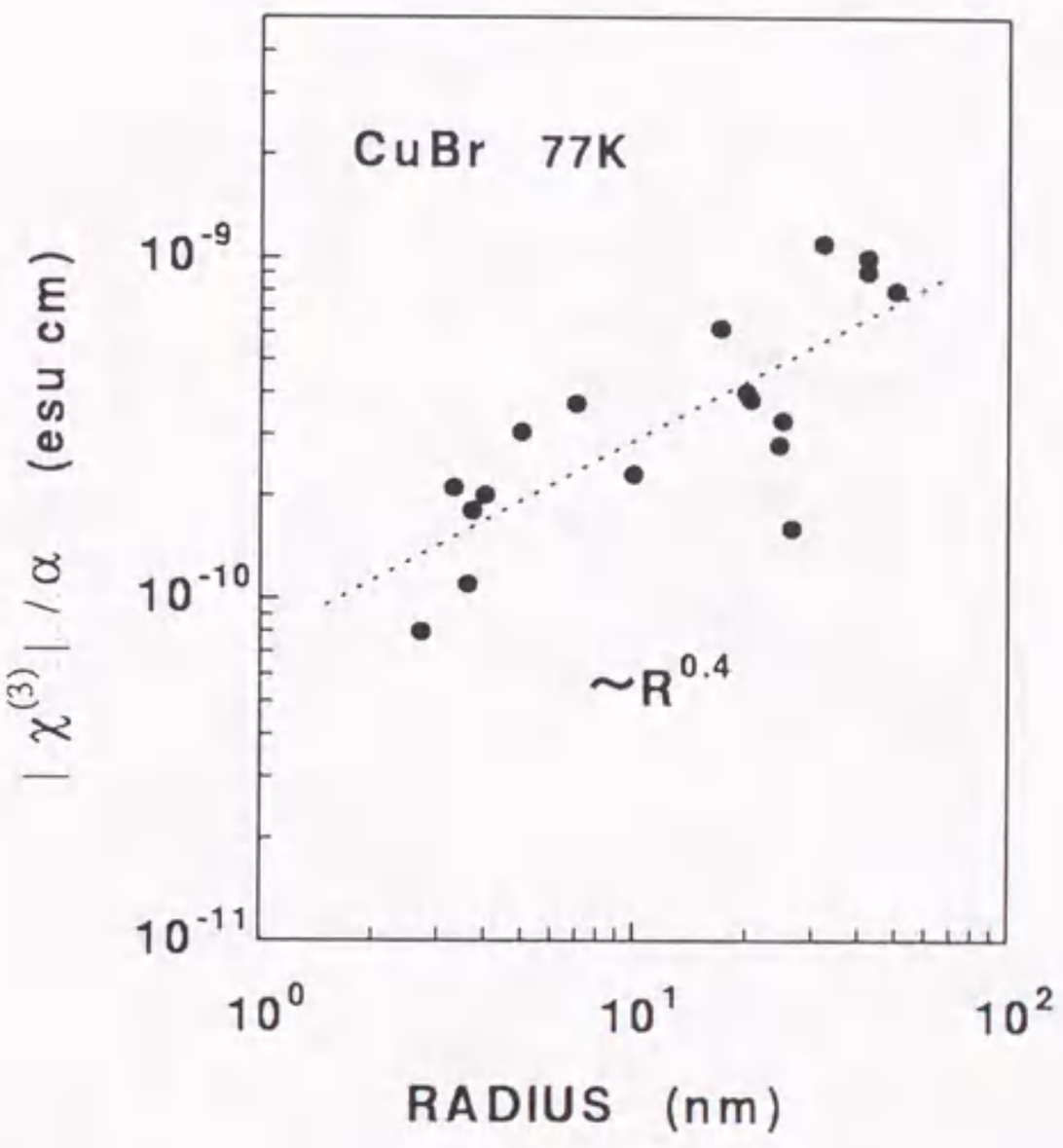

Figure 4.5: $|\chi^{(3)}|/\alpha$ as a function of crystallite radii for CuBr nanocrystals at 77 K. The straight line indicates the result of a least-squares fit, which is the $R^{0.4}$-dependence.

The laser spectral width used in this study (0.02 meV) is much narrower than the spectral width of Z_{12} absorption band ($\geq$20 meV) which is inhomogeneously broadened because of the size distribution. Thus, in our experiments we excite selectively

the nanocrystals in which the pumping light is resonant with the Z_{12} exciton level with Γ_h. The measured diffraction efficiency gives a $|\chi^{(3)}|$ value for the nanocrystals with a certain size within the size distribution. In this case $N_p f_x$ is proportional to $\alpha\Gamma_h$, where N_p is the number density of nanocrystals selectively excited and α is the absorption coefficient at the laser frequency.[6] Therefore, Eq. (1.1) is rewritten to :

$$Im\chi^{(3)}/\alpha \propto f_x \cdot \frac{T_1}{\Gamma_h} \quad . \tag{4.2}$$

As the $|\chi^{(3)}|$ value at the resonance peak is approximately equal to $\mathrm{Im}\chi^{(3)}$, the observed dependence of $|\chi^{(3)}|/\alpha$ shown in Fig. 4.5 suggests that $f_x \times T_1/\Gamma_h$ is dependent on the samples. Consequently, we need further to measure size-dependences of T_1 and Γ_h in order to investigate the origin of the size-dependent behavior of $|\chi^{(3)}|/\alpha$.

4.1.3 Lifetime of excitons

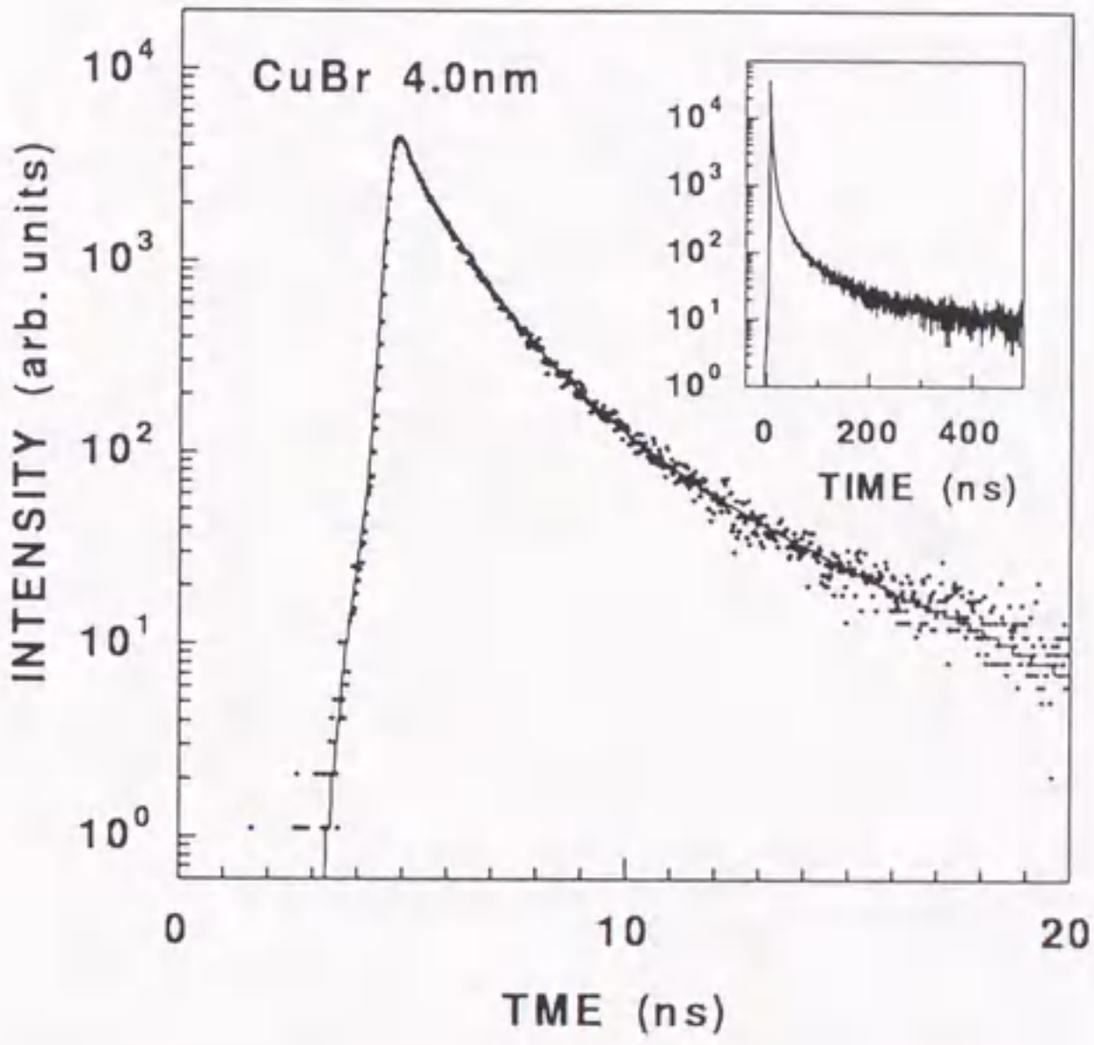

Figure 4.6: Decay curves of luminescence due to Z_{12} excitons in CuBr nanocrystals with $R = 4.0$ nm at 77 K. The solid curve shows the fitted curve with the three-exponential decay. The inset displays the decay on an extended scale.

The longitudinal relaxation time T_1 is determined by measuring the luminescence decay of Z_{12} exciton. Figure 4.6 shows the decay curve of the luminescence due to Z_{12} excitons for the sample with $R = 4.0$ nm at 77 K. As shown in the inset, the decay curve on

the time scale up to 500 ns exhibits a multi-component decay. As there exists a size-distribution of nanocrystals in the sample, the emission band consists of contributions from different nanocrystals, which results in the distribution of decay constants. Assuming three exponentially decaying components,

$$I(t) = a\exp(-\frac{t}{\tau_1}) + b\exp(-\frac{t}{\tau_2}) + c\exp(-\frac{t}{\tau_3}), \tag{4.3}$$

one can define an effective lifetime T_1^* as

$$T_1^* = \frac{a\tau_1 + b\tau_2 + c\tau_3}{a+b+c} \quad . \tag{4.4}$$

Fitting Eq. (4.3) to the decay curve in Fig. 4.6, we obtained 2.0, 30 and 400 ns for τ_1, τ_2 and τ_3, and the coefficients a, b and c were 1, 0.02 and 0.001, respectively. T_1^* turns out to be 2.9 ns, which is dominated by the fast decay component. Figure 4.7 shows

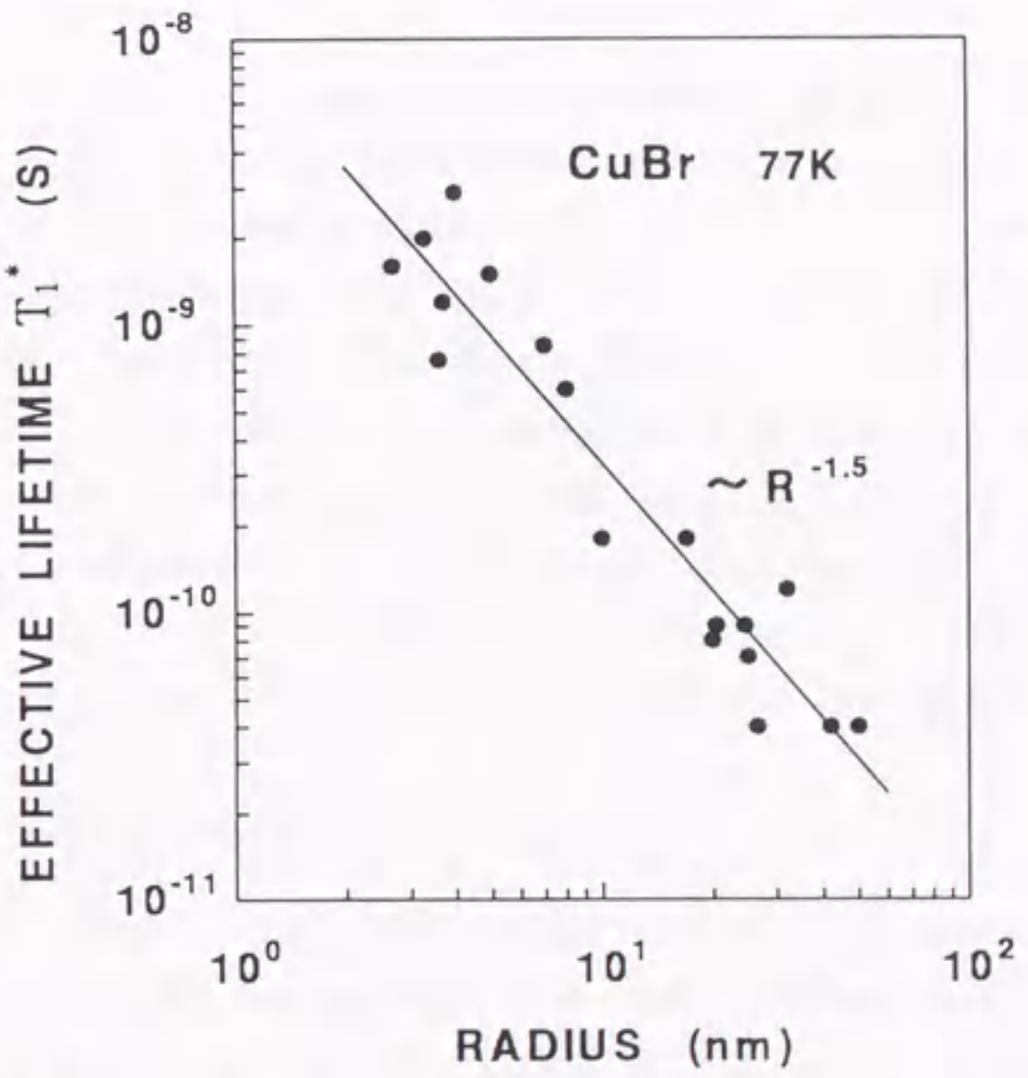

Figure 4.7: Crystallite radius dependence of the effective lifetime T_1^* in CuBr nanocrystals at 77 K. The solid line is the result of a least-squares fit indicating the $R^{-1.5}$-dependence.

the R dependence of T_1^* at 77 K. T_1^* decreases from 2 ns to 30 ps with increasing R for $2.7-50$ nm. The least-squares fit yields the $R^{-1.5}$-dependence, but the data are scattered around this dependence. As the measured decay time is governed by the nonradiative recombination process as well as the radiative process, T_1^* depends on the samples due

to the sample-dependent nonradiative recombination. The scatter of data does not indicate the measurement error of T_1^* but the sample-dependence of the lifetime due to the nonradiative recombination.

As the laser pulse width used in the DFWM measurements is 20 ns, the slow components (30ns- and 400ns-component) in the decay curve for $R = 4.0$ nm (Fig. 4.6) do not satisfy the *cw* excitation condition, i.e., $\tau_2, \tau_3 > t_p$. As pointed out in the previous chapter, the DFWM measurements may give different values of $\chi^{(3)}$ if the relaxation parameters and the pulse width used in the experiment are not properly taken into account. It is significant to clarify carefully the contributions of those slow components to the third-order susceptibilities obtained by Eq. (3.10).

Since the luminescence decay exhibits the three-component decay behavior, one may suppose the photo-excited carrier density $N(t)$ is also in the form

$$N(t) = a\exp(-\frac{t}{\tau_1}) + b\exp(-\frac{t}{\tau_2}) + c\exp(-\frac{t}{\tau_3}), \tag{4.5}$$

where the coefficients a,b and c are the same as those used in Eq. (4.3). By using Eq. (3.10) and (3.14), the $\chi^{(3)}$ value in the stationary regime was calculated, and compared to the $|\chi^{(3)}|$ values calculated using Eq. (3.10). The discrepancy was very small and the contribution of the slow components was found to be negligible. For example, in CuBr nanocrystals with R=4.0 nm, the decay kinetics is decomposed into three components and the slowest one is even longer than the pulse duration of 20 ns as shown in Fig. 4.6. The contributions of τ_1, τ_2 and τ_3 components estimated by using Eq. (3.14) were 91.3%, 8.2% and 0.5%, respectively, and the slowest component of τ_3 was negligible. Therefore, the $\chi^{(3)}$ values obtained from Eq. (3.10) well represent the stationary $\chi^{(3)}$ values in this research in spite of the existence of slow components longer than the laser pulse width.

4.1.4 Homogeneous width of excitons

The size dependence of homogeneous width was investigated by resonant luminescence spectroscopy. Figure 4.8 shows the emission spectra for different radii at 77 K. All the spectra were obtained under the same excitation level as in the DFWM experiments. The uppermost spectrum shows the emission spectrum measured by interband excitation for the sample with $R = 3.6$ nm. The two emission bands are assigned to Z_{12} excitons (E_x) and biexcitons (B). When we changed the laser wavelength as indicated by vertical arrows, we observed the considerably narrow luminescence spectrum in the higher energy side of excitation energy. The spectral shape in the higher energy side can be well fitted to the Lorentz-function, and we attribute this spectrum to the resonant luminescence from the size-selected nanocrystals within the size distribution. As the inhomogeneous width is much larger than the homogeneous width, the half of the half width at half maximum

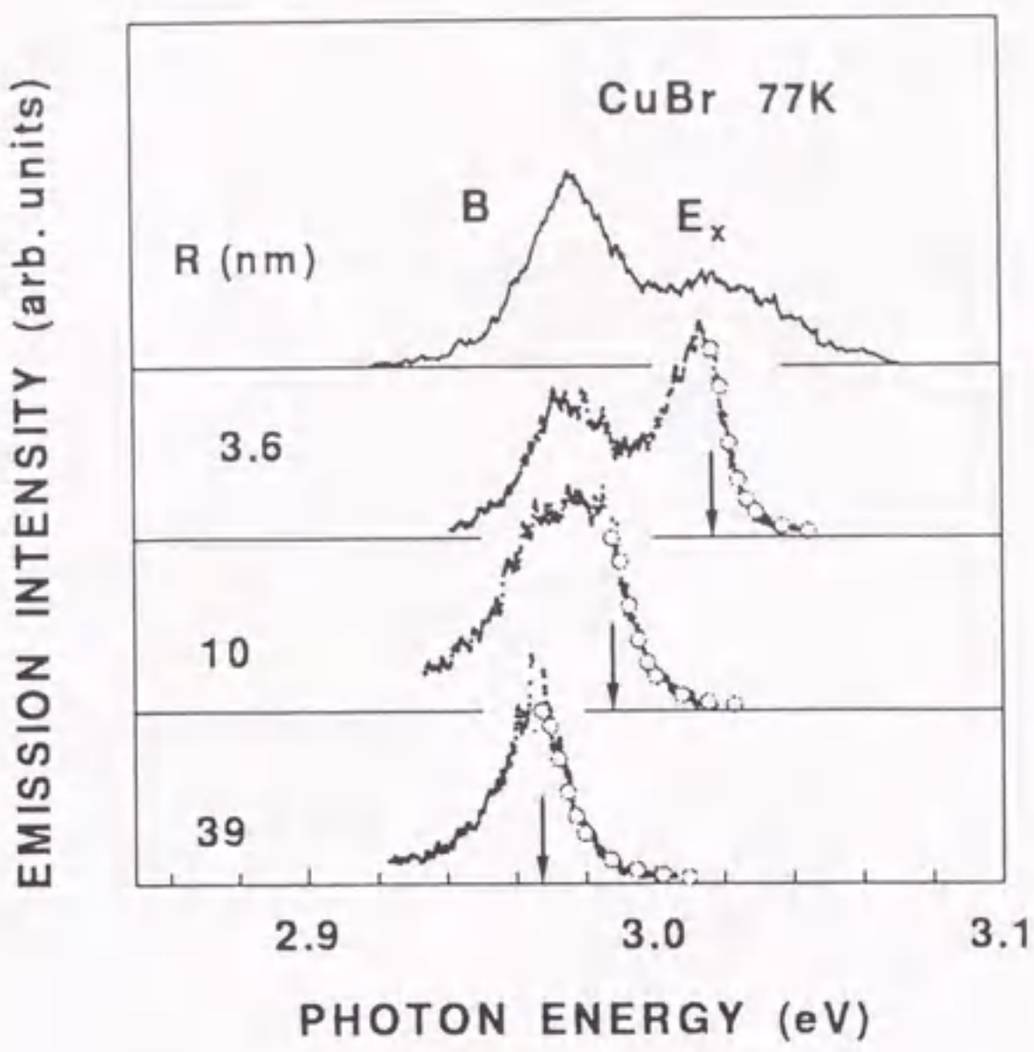

Figure 4.8: Resonant luminescence spectra of CuBr nanocrystals with different radii at 77 K. The uppermost spectrum shows the luminescence spectrum for R=3.6 nm under the interband excitation. The two emission bands are due to excitons (E_x) and biexcitons (B), respectively. Open circles indicate Lorentzian fittings.

of the resonant luminescence band corresponds to Γ_h. Γ_h was found to be independent of the excitation intensity between 10 and 100kW/cm^2. In Fig. 4.8, the widths are 2.5, 3.1 and 4.0 meV for R =3.6, 10 and 39 nm, respectively.

In order to investigate the mechanism that determines Γ_h, resonant luminescence was measured for the sample with R = 3.6 nm changing temperatures between 8 and 170 K as shown in Fig. 4.9. The obtained homogeneous widths can be well fitted to the function $0.4 + 0.022T + 5.0/(exp(\hbar\omega_{LO}/K_BT) - 1)$, where $\hbar\omega_{LO}$ is taken as the bulk longitudinal optical (LO) phonon energy 20.7 meV. [53] The first term on the right-hand side represents the temperature independent broadening, and the second T-linear term is due to the longitudinal acoustic phonon scattering. The third term is caused by the LO-phonon scattering of excitons. As can be seen, Γ_h is proportional to the temperature in the range of $8-50$ K, which indicates the accoustic-phonon scattering via piezoelectric coupling and deformation potential coupling. At 77 K, both the LO-phonon scattering and the acoustic phonon scattering contribute to Γ_h, though the latter is dominant.

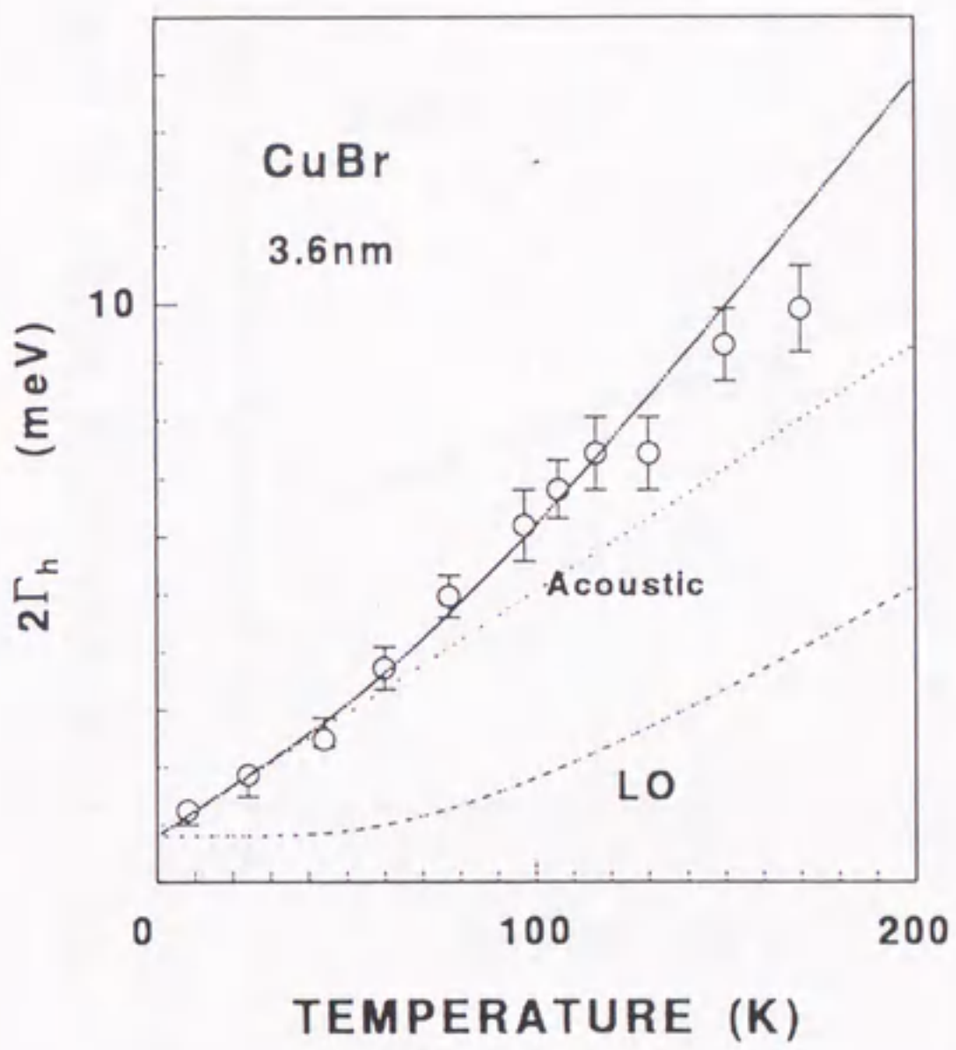

Figure 4.9: Temperature dependence of homogeneous width of Z_{12} excitons in CuBr nanocrystals of $R = 3.6$ nm. The solid line indicates the best fit of $\Gamma_h = 0.4 + 0.022 \cdot T + 5.0/(exp(\hbar\omega_{LO}/KT) - 1)$, where $\hbar\omega_{LO}$ is taken as the bulk LO phonon energy 20.7 meV. The dotted-line indicates the T-linear dependence which is due to the acoustic phonon, and the broken curve represents the LO-phonon scattering contribution.

The radius dependence of Γ_h at 77 K is shown in Fig. 4.10. Γ_h is weakly dependent on the radius, and exhibits the $R^{0.1}$-dependence. The width varies from 2.5 meV to 4.0 meV when R is increased from 2.7 nm to 39 nm. The values of Γ_h are in agreement with the results which were obtained from the resonant luminescence spectroscopy[51] and persistent hole-burning spectroscopy[54] for CuCl nanocrystals embedded in NaCl crystals. Similar results have been also obtained in CuBr nanocrystals by persistent hole-burning experiments at the excitation levels of $\sim 100\mathrm{kW/cm^2}$. [55]

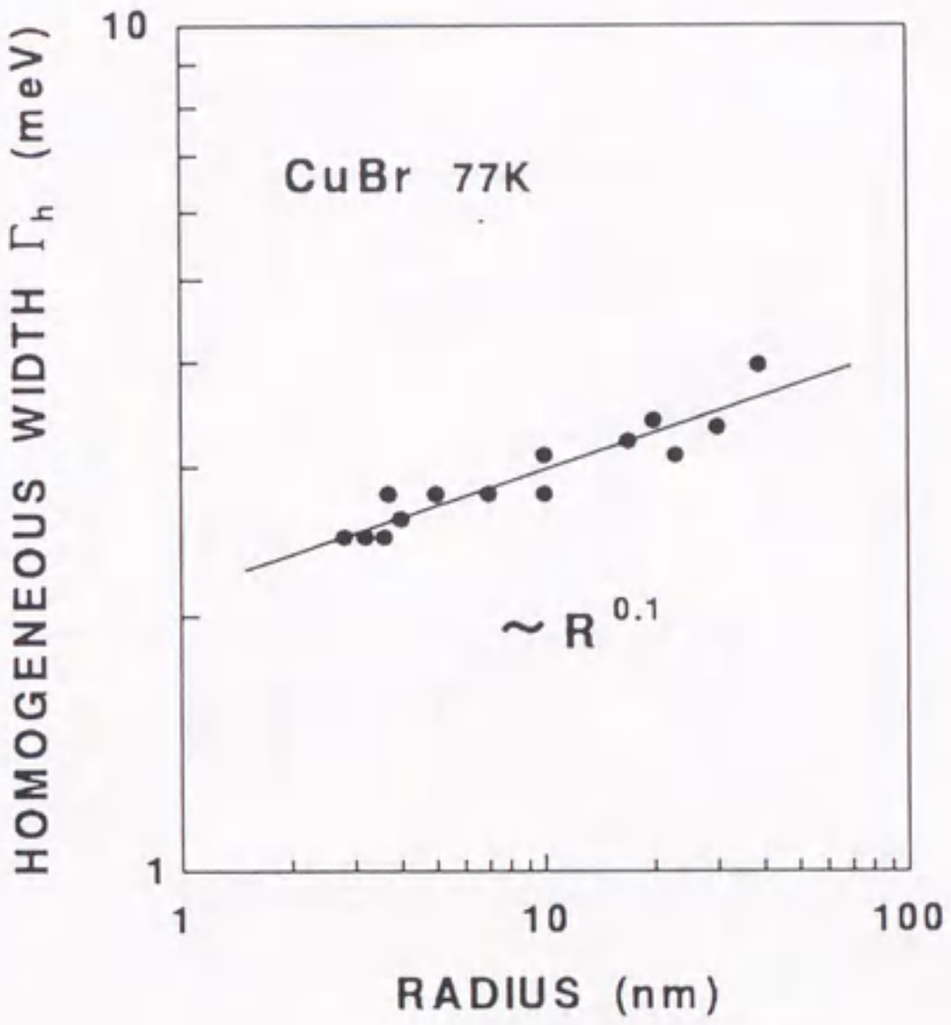

Figure 4.10: Crystallite radius dependence of homogeneous width of Z_{12} exciton band in CuBr nanocrystals at 77 K. The solid line is the result of a least-squares fit which indicates the $R^{0.1}$-dependence.

4.2 Discussion

Figure 4.11 shows the figure of merit $|\chi^{(3)}|\Gamma_h/\alpha T_1^*$. The figure of merit increases upon an increase of R, without showing saturation in the size range studied. The least-squares fit yields the $R^{1.9}$-dependence, which is stronger than the observed dependence of $|\chi^{(3)}|/\alpha$ in Fig. 4.5. This results from the fact that T_1^* is approximately dependent on $R^{-1.5}$. A larger $|\chi^{(3)}|/\alpha$ value can be obtained with a shorter response time in a larger nanocrystal, which is a satisfactory property for the nanocrystals as a promising candidate of the nonlinear optical materials.

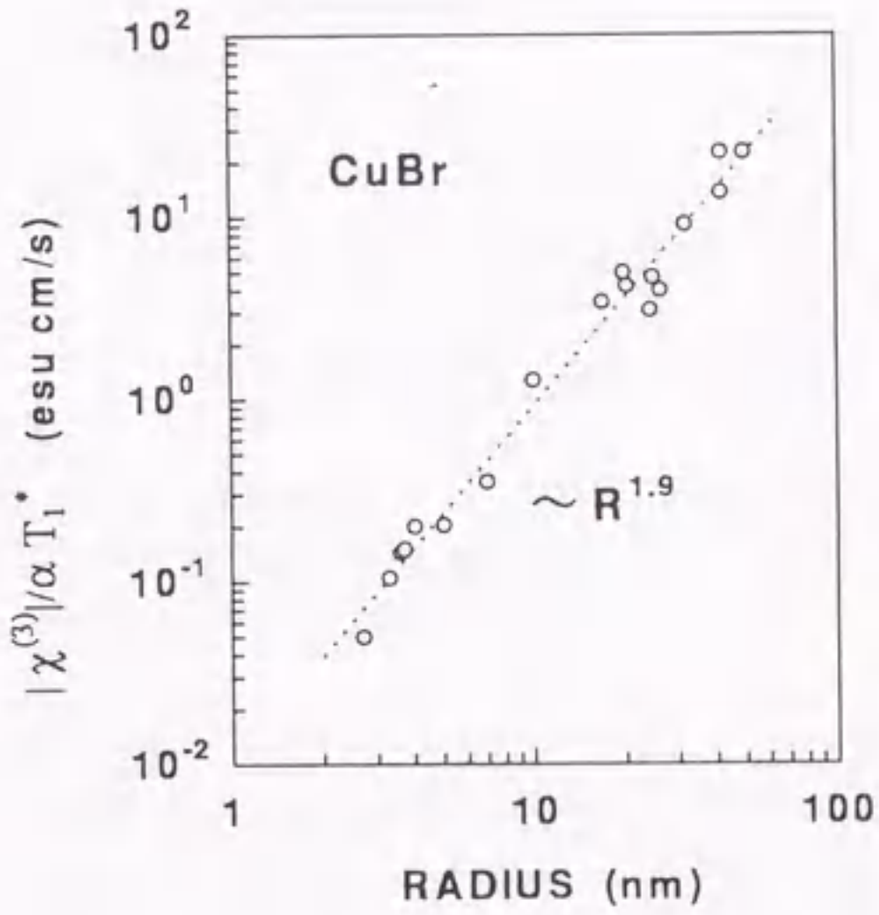

Figure 4.11: Figure of merit $|\chi^{(3)}|/\alpha T_1^*$ for Z_{12} excitons in CuBr nanocrystals as a function of the nanocrystal radius.

Now we come to the point to elucidate the size dependence of oscillator strength of the confined Z_{12} exciton, using the size-dependences of $|\chi^{(3)}|/\alpha, \Gamma_h$ and T_1^*. The size dependence of $|\chi^{(3)}|\Gamma_h/\alpha T_1^*$ which is proportional to f_x is plotted in Fig. 4.12. In the size range of $2.7 \leq R \leq 50$ nm, $\chi^{(3)}\Gamma_h/\alpha T_1^*$ exhibits the $R^{2.0}$-dependence, indicating an enhancement of more than two orders of magnitude. This dependence is in good agreement with that observed for CuCl nanocrystals, which is $R^{2.1}$. [56] It is clear now that similar enhancement effect of the exciton oscillator strength exists also in CuBr nanocrystals, and it is this enhancement effect that gives rise to the size-dependent susceptibilities. This giant oscillator strength arises from the coherent character of the exciton formed through out the nanocrystal, and consequently the third-order nonlinear polarization is dependent on the square of volume. In contrast, the linear absorption is just proportional to the

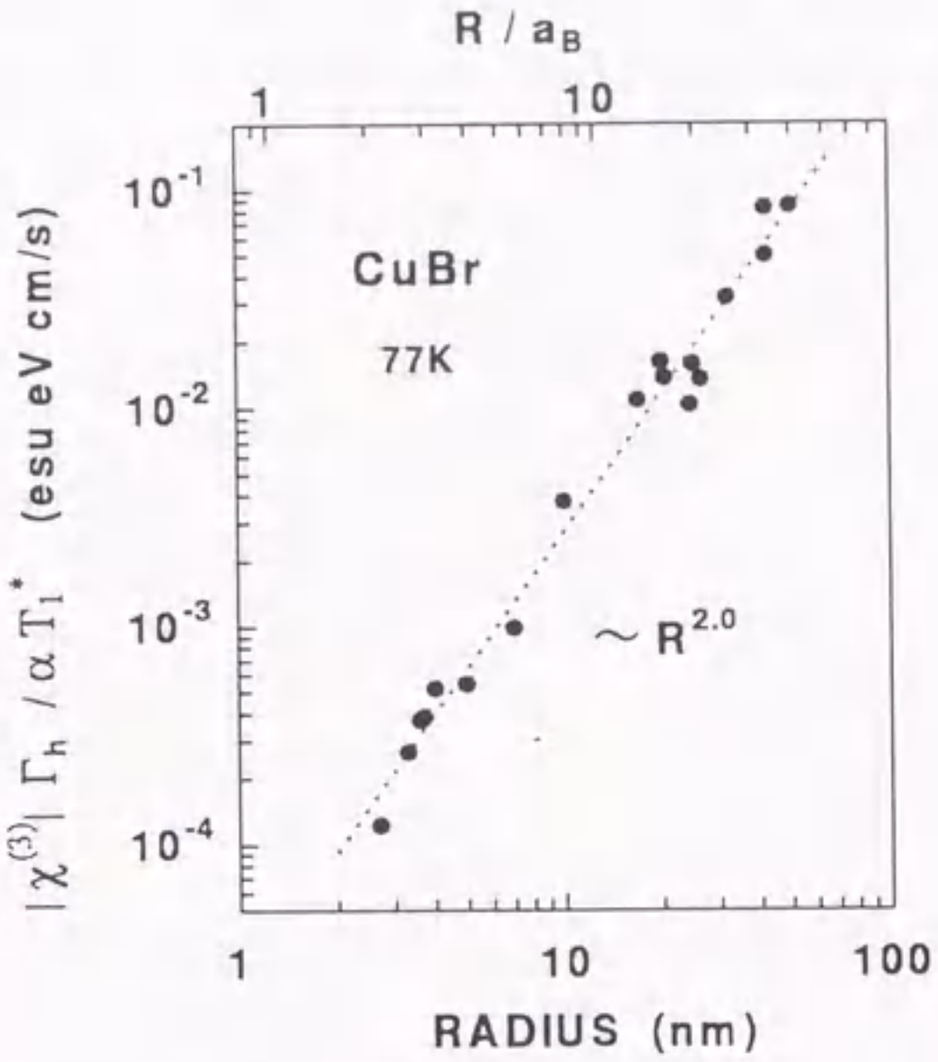

Figure 4.12: Crystallite radius dependence of $|\chi^{(3)}|\Gamma_h/\alpha T_1^*$ being proportional to the oscillator strength of Z_{12} excitons in CuBr nanocrystals. Solid line is the result of a least-squares fit which indicates the $R^{2.0}$-dependence.

volume and the absorption coefficient is independent of the nanocrystal size. (Also see Eq. (2.50) and (2.53) and notice the difference in power of the moment μ_{eg}.)

The theoretical calculation on the confined excitons predicts the R^3-dependence while the experiment result is R^2. This discrepancy may be attributed to the fact that the confinement potential is finite in CuBr nanocrystals embedded in glass, while infinite confinement potential has been assumed in the theoretical calculation. The band gap of the glass matrix used in this work is about 4.3 eV, while that of the CuBr nanocrystals is about 3.1 eV. [57] The confinement potential of the electron-hole pair is 1.2 eV, roughly 12 times of the Z_{12}-exciton Rydberg energy 104 meV. Such a finite confinement potential gives rise to the penetration of the exciton wavefunction into the glass matrix, and consequently results in less effective confinement. The power of the R-dependence is thus expected to be lowered.

It is of interest to note that the size-dependent enhancement of f_x per nanocrystal does not saturate up to the largest size of $R \approx 40a_B$ studied here, as shown in Fig. 4.12. This behavior is different from that observed in CuCl nanocrystals, where the decrease of oscillator strength is clearly observed for the large nanocrystals. [56] To understand this difference, let us first review the case for CuCl nanocrystals and then compare it to that

for CuBr nanocrystals. Figure 4.2 shows the $|\chi^{(3)}|\Gamma_h/\alpha T_1^*$ as a function of mean radius for CuCl nanocrystals. * As can be seen, the size-enhancement exhibits the saturation and

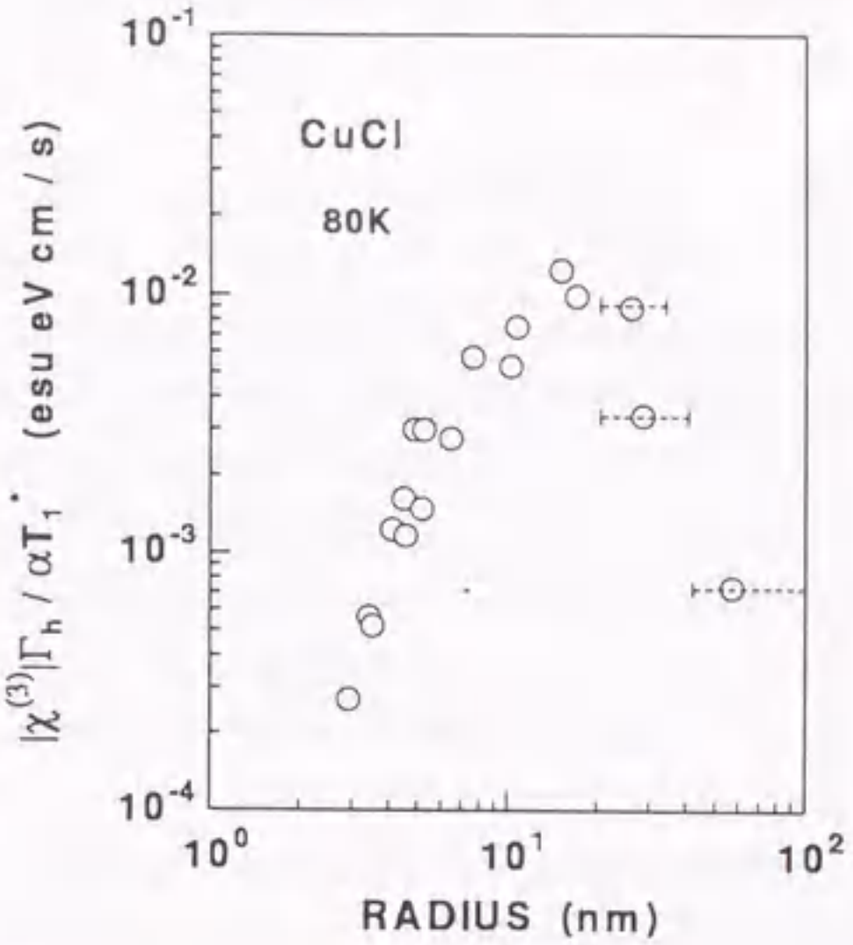

Figure 4.13: Size dependence of $|\chi^{(3)}|\Gamma_h/\alpha T_1^*$ for CuCl nanocrystals.

decrease around $R \sim 15$ nm. In CuCl nanocrystals, the saturation of the size enhancement was argued in terms of the following mechanisms. [56] First, the energy splitting of the confined levels in large nanocrystals becomes smaller and higher confined levels are thermally excited. The thermal energy k_BT corresponds to the confinement energy ΔE for the nanocrystals for which f_x has a maximum value. The oscillator strength is then redistributed among the thermally activated sublevels, and this leads to the decrease of f_x defined for the two-level system. Second, when the longitudinal-transverse splitting Δ_{LT} becomes comparable to the confinement energy, the giant-oscillator-strength effect disappears. For CuBr nanocrystals, the smallest confinement energy is $\Delta E = 17$ meV for the sample with the largest mean radii($R = 50$ nm) in this study, and the thermal energy is $k_BT = 6.7$ meV at 77 K. As the longitudinal-transverse splitting equals

* Note that the mean radii of CuCl nanocrystals have been corrected for the mean radii in Fig. 3 of Ref. [56]. In Ref. [56], the mean radii of CuCl nanocrystals were estimated from the empirical relationship between the radius and the confinement energy ΔE of the lowest confined Z_3 exciton, i.e.,

$$\Delta E = 0.67 \cdot \frac{\hbar^2}{2M_{ex}}(\frac{\pi}{R})^2, \tag{4.6}$$

which was cited from Ref. [58]. However, it was later found by X-ray diffraction measurements that such a relation does not hold for the samples used in Ref. [56]. The confinement energy for CuCl nanocrystals was found to consists of the exciton mass-center confinement energy as well as a Coulomb interaction term due to the interface charge, as described in Section 4.1.1 of this chapter. Therefore, the simple estimation using Eq. (4.6) yielded smaller radii than the actual ones.

12.5 meV, [28] we have the following inequalities: $\Delta E(\geq 17$ meV$) > k_B T$ (6.7meV) and $\Delta E(\geq 17$ meV$) > \Delta_{LT}$ (12.5 meV). Both the first and the second mechanisms predict the unsaturating behavior of oscillator strength in the size range studied. As the experiment result does not exhibit the saturation, both the mechanisms may explain the experimental results.

The recent theoretical work by Nair and Takagahara has suggested a new explanation for the saturation behavior in large CuCl nanocrystals. They took into account the contribution due to the higher sublevels of confined excitons but this does not cancel out completely the enhancement of $\chi^{(3)}$ due to the lowest exciton. In stead, taking into account the two-exciton states(biexcitons) for large CuCl quantum dots, they found that pronounced cancellation of the contributions to $\chi^{(3)}$ occurs between the two-exciton states and the lowest exciton state resulting in the saturation behavior in CuCl nanocrystals. [59] The two-exciton states should also exist in CuBr nanocrystals. Actually, luminescence due to the biexcitons has been observed.(See Fig. 4.8.) Therefore, the same cancellation effect should also exist in CuBr nanocrystals resulting in the saturation behavior. Why the cancellation effect does not work in CuBr nanocrystals is not clear at the present stage. Since the valence band structure is different in CuCl and CuBr, as a hint to the answer, the role of the band structure is investigated in the next chapter.

4.3 Summary

The size-dependent optical nonlinearity in CuBr nanocrystals over the wide range of sizes has been investigated by means of DFWM, luminescence lifetime and resonant luminescence experiments. Measurements of the dispersion of $|\chi^{(3)}|$ have revealed that the nonlinearity is governed by resonant enhancement of confined excitons. The figure of merit $|\chi^{(3)}|/\alpha T_1^*$ at the resonance with Z_{12} excitons exhibits the size-dependent enhancement of $R^{1.9}$. The measured lifetime and homogeneous width show the size-dependences of $R^{-1.5}$ and $R^{0.1}$, respectively. The size dependence of the oscillator strength of Z_{12} excitons was derived from the measured relaxation parameters. An unambiguous size enhancement of the oscillator strength per nanocrystal was elucidated in CuBr nanocrystals, i.e., $f_x \propto R^{2.0}$ for $2.7 \leq R \leq 50$ nm. The size dependence of oscillator strength does not exhibit the saturation behavior for the larger sizes, which is unlike the case of CuCl nanocrystals. The saturation behavior observed in CuCl nanocrystals is explained in terms of the cancellation of the exciton mediated enhancement with the contributions of the two-exciton states. The different behavior of the size dependence between CuCl and CuBr nanocrystals implies the role of the valence band structure in the size-dependent enhancement of nonlinear polarization in the resonant regime.

Chapter 5

Third-order susceptibilities in $CuBr_xCl_{1-x}$ (x=0.11, 0.26, 0.97) nanocrystals

Preface

As discussed in Chapter 4, the size dependence of the oscillator strength f_x exhibit different features in the large-sized CuCl and CuBr nanocrystals. In CuCl nanocrystals a saturation and decrease of f_x is observed, while in CuBr nanocrystals no saturation is observed in the size range under investigation. The saturation behavior for CuCl nanocrystals can be interpreted in terms of the contributions of the two-exciton states. As this contribution may exist also in CuBr nanocrystals, the different behaviors imply a role of the valence band structure in the size dependence for large sizes. Naturally the unsaturating enhancement of oscillator strength with increasing size to infinity is unphysical. For further larger sizes approaching to the light wavelength, the size-enhancement should be saturated, and the oscillator strength should converge to the bulk limit. This situation is also discussed at the end of this chapter. In this chapter, the size-dependences of the third-order nonlinearity and the oscillator strength have been investigated for $CuBr_xCl_{1-x}$ (x=0.11, 0.97 and 0.26) nanocrystals. As the spin-orbit splitting between Γ_7- and Γ_8- valence bands is 0 at $x = 0.26$, the valence band structure for $x = 0.11$ and that for $x = 0.97$ are analogous to that of CuCl and CuBr, respectively. The size-dependences of the oscillator strength in nanocrystals of CuCl-type, CuBr-type and the nearly-degenerate case have been compared to make clear a role of the valence band structures.

5.1 Results

5.1.1 Quantum size effect and the dispersion of the third-order nonlinear susceptibility $\chi^{(3)}$

Figure 5.1 shows the absorption spectra and photon energy dependence of $\chi^{(3)}$ for $CuBr_xCl_{1-x}$ nanocrystals with various composition ratios in the size range of $4.1 - 5.2$ nm. The two absorption bands correspond to Z_3 and Z_{12} excitons consisting of the Γ_7 and Γ_8 valence band, respectively. For $x \leq 0.26$, the Z_3-exciton band lies in the lower-energy side, while for $x \geq 0.26$ the Z_{12}-exciton band lies in the lower-energy side. The Z_{12}- and Z_3-exciton bands are nearly degenerate for $x = 0.26$. The variation of the absorption features, due to Z_{12} and Z_3 excitons, with composition ratios is consistent with the results obtained in the bulk alloy, indicating that the band structures are varied in nanocrystals. Vertical arrows indicate the lowest exciton peaks in bulk solid solutions, which are obtained using the bulk exciton energies with the same composition ratios.[60] All the absorption peaks shift to the blue side due to the quantum confinement effect.

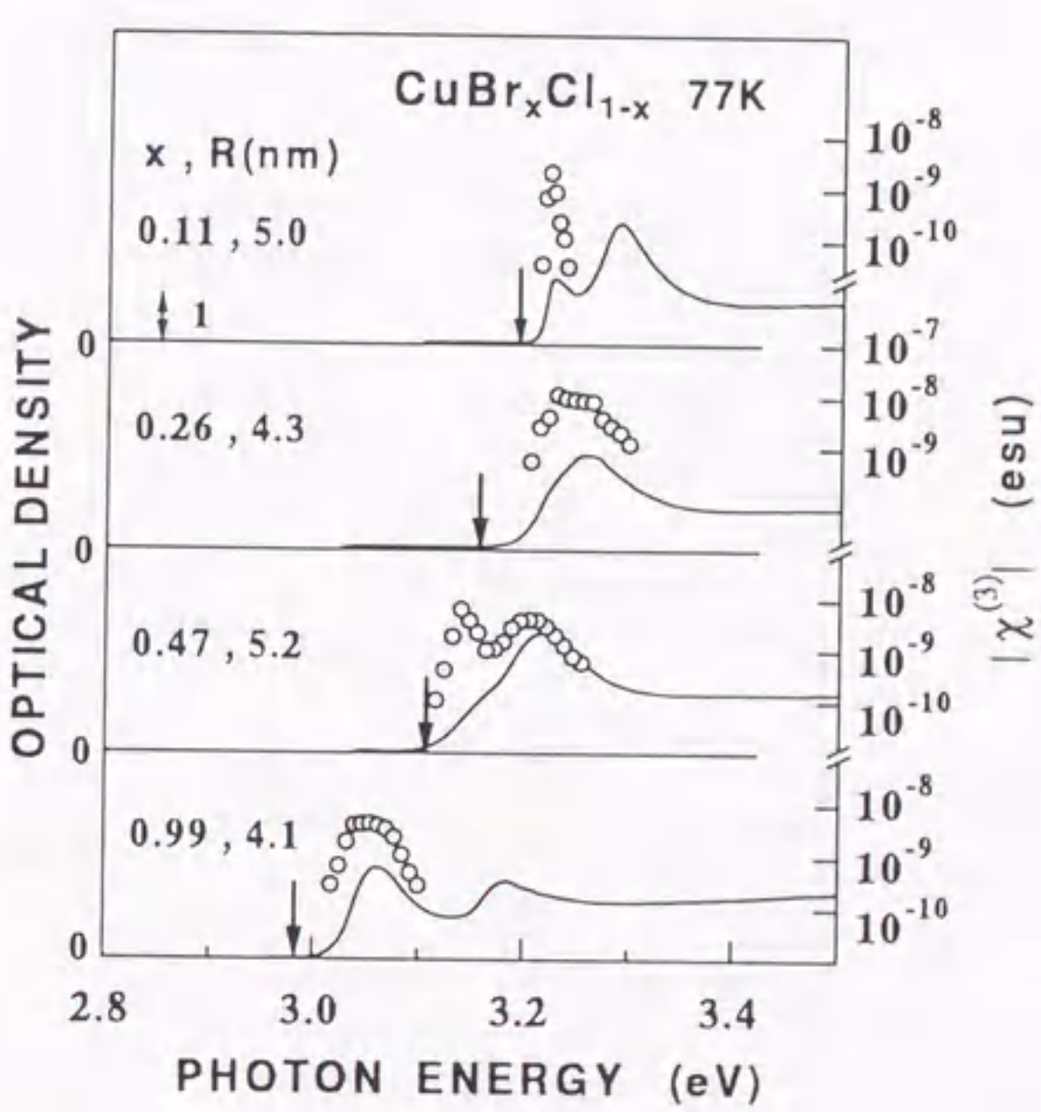

Figure 5.1: Absorption spectra and photon energy dependence of $|\chi^{(3)}|$ for $CuBr_xCl_{1-x}$ nanocrystals with different mean radii and composition ratios at 77 K. Open circles and solid curves illustrate $|\chi^{(3)}|$ and the absorption spectrum, respectively.

Here let us discuss the problem of the composition ratio fluctuations. The composition ratio and the mean radius of $CuBr_xCl_{1-x}$ nanocrystals have been estimated by the XRD profile analysis ignoring fluctuations in the composition ratio. Any fluctuations in the composition ratio for different nanocrystals corresponds to the fluctuations in lattice constants, and consequently the diffraction angle due to nanocrystals in XRD measurements has a distribution. This means an error in the size(composition ratio) estimation from the width(diffraction angle) of the XRD pattern. The fluctuations in the composition ratio is also reflected in the distribution of exciton energies, and we can make a rough estimation of the fluctuations through observing the absorption spectra. The spectral width of the lowest exciton band for $x = 0.11$ is about 10 meV and that for $x = 0.99$ is about 25 meV. They are almost the same as those for CuCl and CuBr, respectively. The spectral width of the exciton band is dominated by the inhomogeneous width, which arises from the distributions of size and composition ratio for the alloy case but only the size distribution for the purely CuBr or CuCl cases. As the size distribution for nanocrystals with a similar mean radius may be almost the same, the similar inhomogeneous width for the alloy and pure copper halide cases suggests that the inhomogeneous broadening is governed by the crystallite size distribution and the contribution of the fluctuation of composition ratio is negligible.

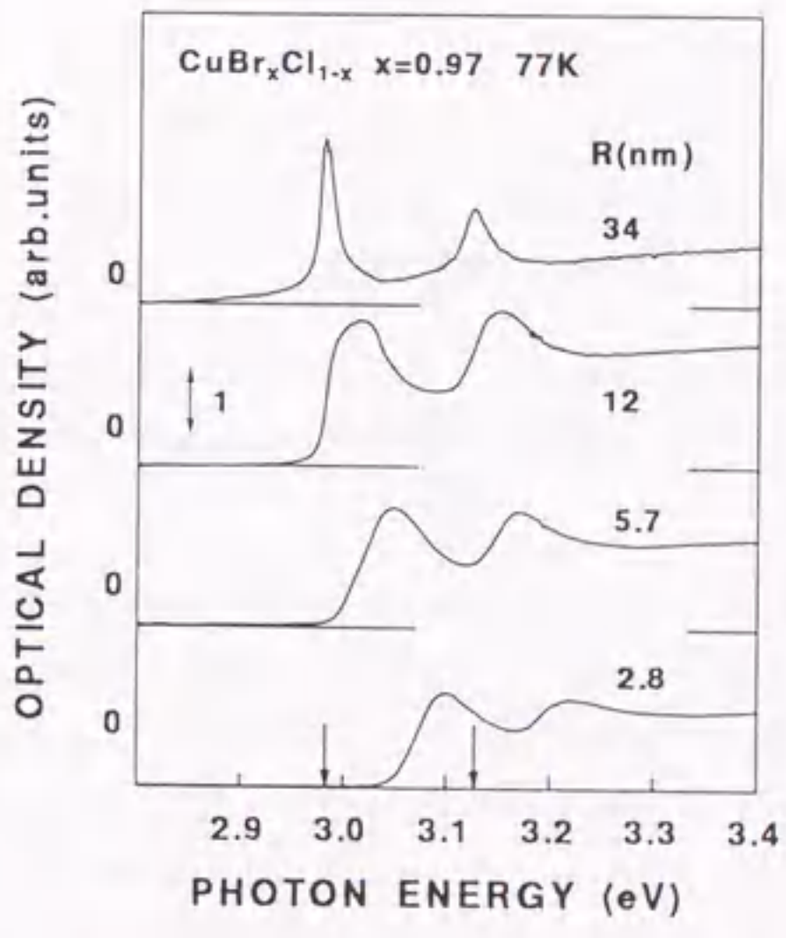

Figure 5.2: Absorption spectra of $CuBr_xCl_{1-x}$ nanocrystals ($x = 0.97$) with different mean radii at 77 K. Vertical arrows indicate the bulk Z_{12}- and Z_3-exciton energies for $x = 0.97$.

Figure 5.2, 5.3 and 5.4 show the absorption spectra of $CuBr_xCl_{1-x}$ nanocrystals with various mean radii for $x = 0.97, 0.11$ and 0.26, respectively. All the spectra were measured at 77 K. Vertical downward arrows indicate the bulk exciton energies for the corresponding composition ratios. Z_{12} and Z_3 exciton bands can be seen and they are shifted to the higher-energy-side due to quantum confinement effect. The details have been described in Section 4.1 of Chapter 4.

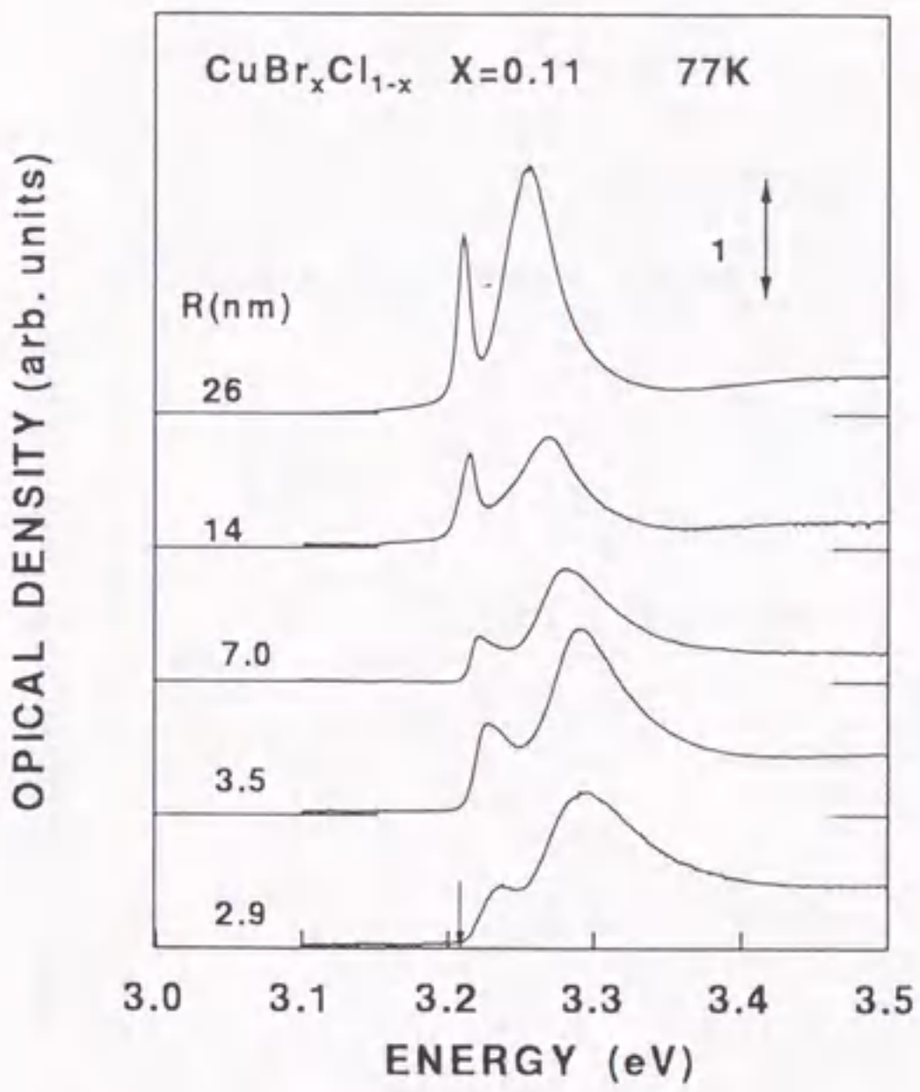

Figure 5.3: Absorption spectra of $CuBr_xCl_{1-x}$ nanocrystals ($x = 0.11$) with different mean radii at 77 K. The vertical downward arrow indicates the bulk Z_3-exciton energy for $x = 0.11$.

To observe resonant behaviors of nonlinearities, the $\chi^{(3)}$ values have been measured around the exciton absorption bands. As shown by open circles in Fig. 5.1, $\chi^{(3)}$ exhibits the resonance enhancement at the vicinity of excitonic absorption peak. The resonant behavior is more pronounced in the $\chi^{(3)}$ spectrum than in the absorption spectrum. In the sample of $R = 5.2$ nm (x=0.47), the absorption of the Z_{12} exciton appears as a shoulder in the lower-energy side of the absorption spectrum, but in contrast the dispersion of $\chi^{(3)}$ exhibits clearly a peak. This is attributed to the fact that higher order interaction between light and matter is involved in the third-order nonlinear process, as noted in Section 2.2.2 of Chapter 2.

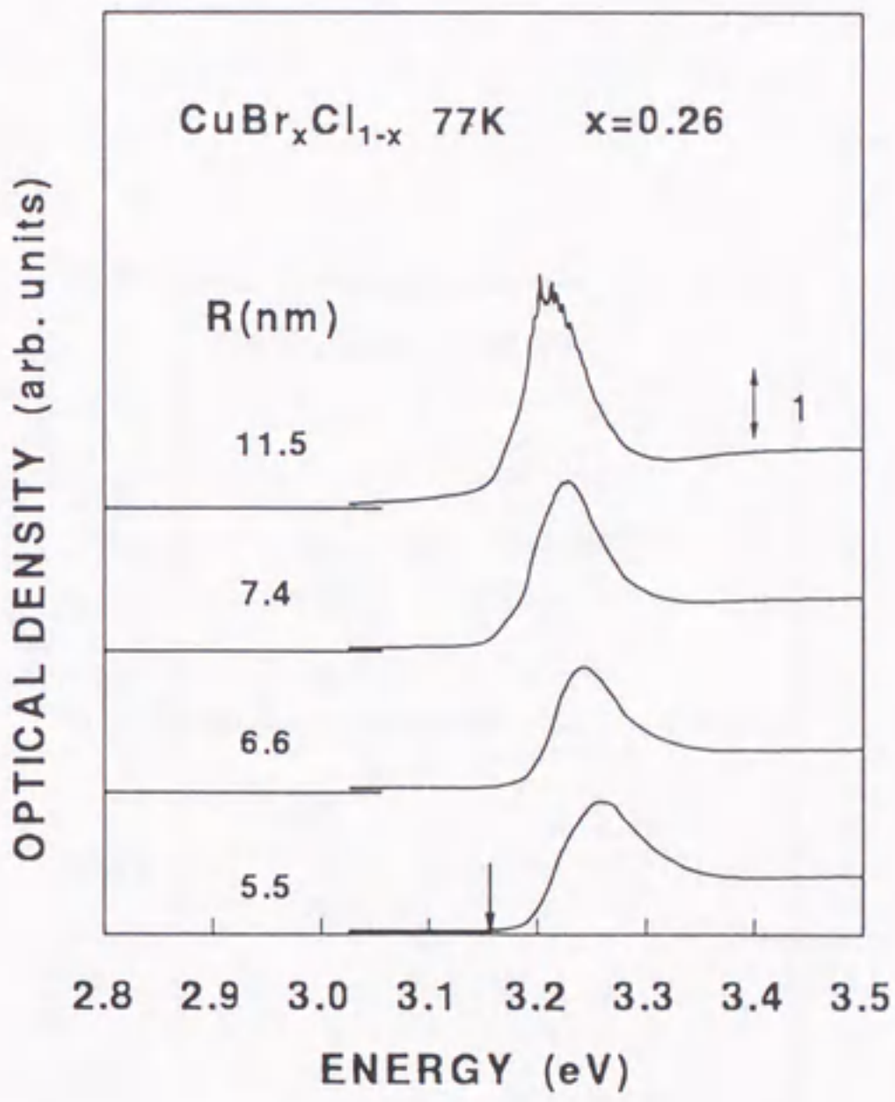

Figure 5.4: Absorption spectra of $CuBr_xCl_{1-x}$ nanocrystals ($x = 0.26$) with different mean radii at 77 K. The vertical downward arrow indicates the bulk exciton energy for $x = 0.26$.

5.1.2 Size dependence of the third-order nonlinear susceptibility $\chi^{(3)}$

In analogy with the study of CuBr nanocrystals, the size dependence of $\chi^{(3)}$ at resonance with the lowest confined exciton was measured and then analyzed by the two-level model. The R-dependences of T_1^* and Γ_h were then measured and the size dependence of the exciton oscillator strength was obtained with the measured parameters. The results of 1) the R-dependences of $\chi^{(3)}$, T_1^* and Γ_h, 2) the R-dependence of the figure of merit $|\chi^{(3)}|/\alpha T_1^*$, and 3) the R-dependence of the exciton oscillator strength, are presented for the $CuBr_xCl_{1-x}$ nanocrystals with $x = 0.97, 0.11$ and 0.26.

x=0.97

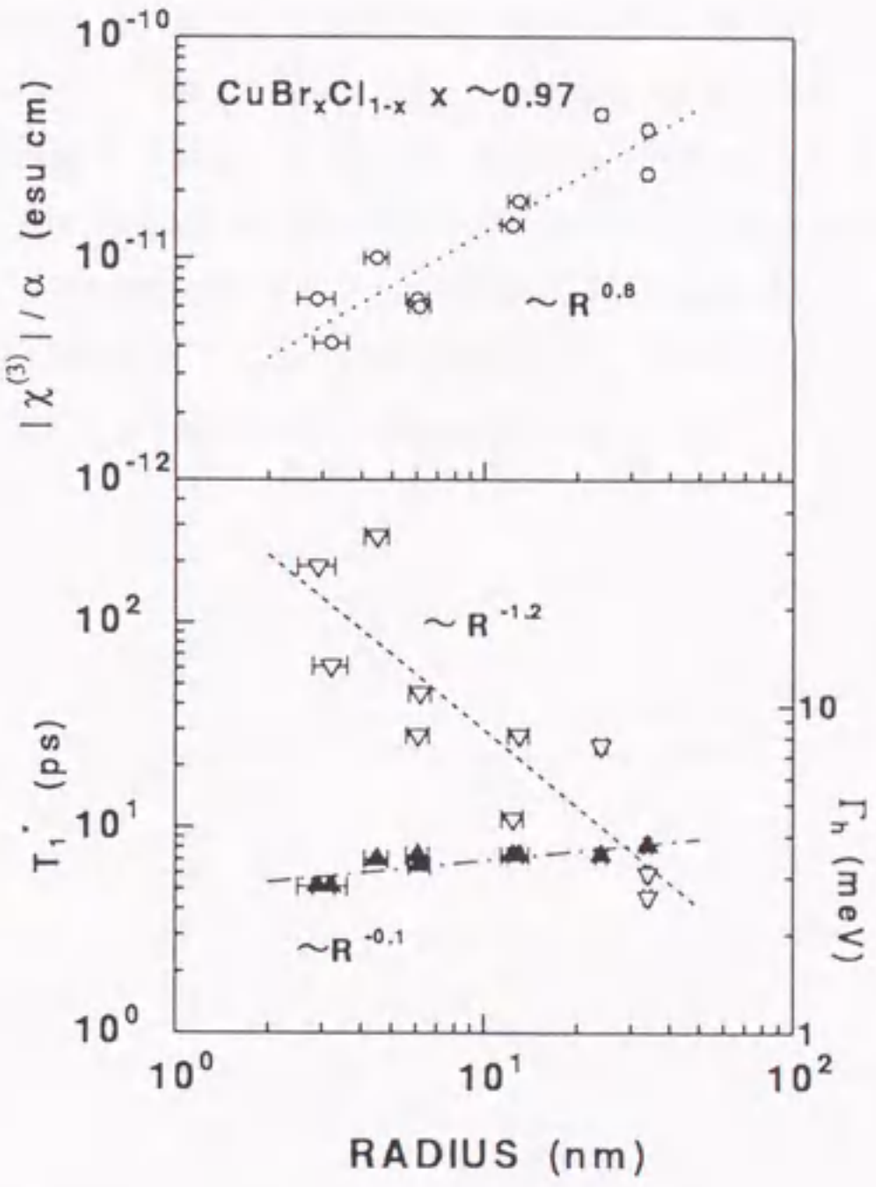

Figure 5.5: (a) $|\chi^{(3)}|/\alpha$ as a function of crystallite radii for $CuBr_xCl_{1-x}$ nanocrystals ($x = 0.97$) at 77 K. The straight line indicates the result of a least-squares fit, which is the $R^{0.8}$-dependence. (b) Radius dependence of T_1^*, and Γ_h for $CuBr_xCl_{1-x}$ nanocrystals ($x = 0.97$) at 77 K.

The size dependence of $|\chi^{(3)}|/\alpha$ measured at the peak energy of the Z_{12} excitons is shown in Fig. 5.5 (a). $|\chi^{(3)}|/\alpha$ increases with increasing sizes and a least-squares fit yields the $R^{0.8}$-dependence. The $|\chi^{(3)}|/\alpha$ value ranges from $0.40 - 4.4 \times 10^{-11}$ esu·cm for the radii in the range from $2.8 - 34$ nm, and the values are much smaller than that of CuBr nanocrystals with the corresponding radius, suggesting shorter T_1 and/or larger Γ_h than those for CuBr nanocrystals. Figure 5.5 (b) shows the measured values of effective lifetime T_1^* and Γ_h as a function of radius. Γ_h (closed triangles) is almost independent of the size and the values range from $2.5 - 3.8$ meV. Both the size dependence and the magnitude of Γ_h are similar to those for CuBr nanocrystals. As the luminescence decay curve exhibits a three-component decay, the T_1^* defined by Eq. (4.4) has been used. The effective lifetime T_1^*(open triangles) ranging from $4.6 - 270$ ps decreases with decreasing size generally, and a least-squares fit yields the $R^{-1.2}$-dependence. Here, the lifetimes for the four samples in the size range from $13 - 34$ nm are too short to be accurately measured from the luminescence decay curve, so they were measured by a pump-probe measurement using the 200 fs-Ti:Al_2O_3 laser. The time-delay dependence of the differential absorption at the absorption peak gives a value of T_1^*. As shown in Fig. 5.6, the decay curves for the samples (a) and (b) were fitted to the two-component exponential decay, i.e., $c = 0$ in Eq. (4.3)., The fitting parameters are 7 ps(1) and 150 ps(0.3) for the sample (a), 6 ps(1) and 150 ps(0.2) for the sample (b), respectively. For the samples (c) and (d), the single exponential fitting yields 6 ps and 5 ps, respectively.

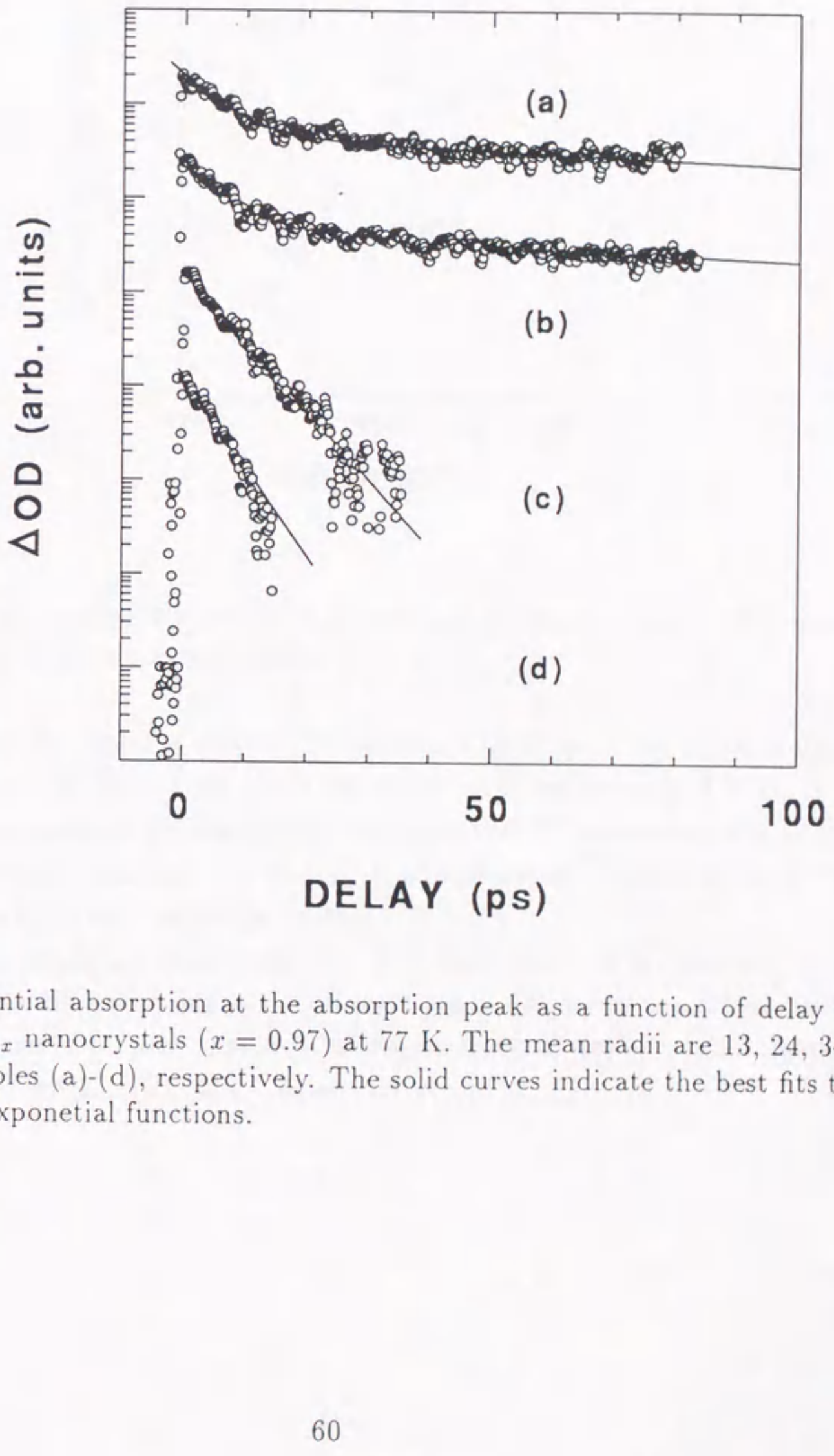

Figure 5.6: Differential absorption at the absorption peak as a function of delay times for four $CuBr_xCl_{1-x}$ nanocrystals ($x = 0.97$) at 77 K. The mean radii are 13, 24, 34 and 34 nm for the samples (a)-(d), respectively. The solid curves indicate the best fits to the multi-component-exponetial functions.

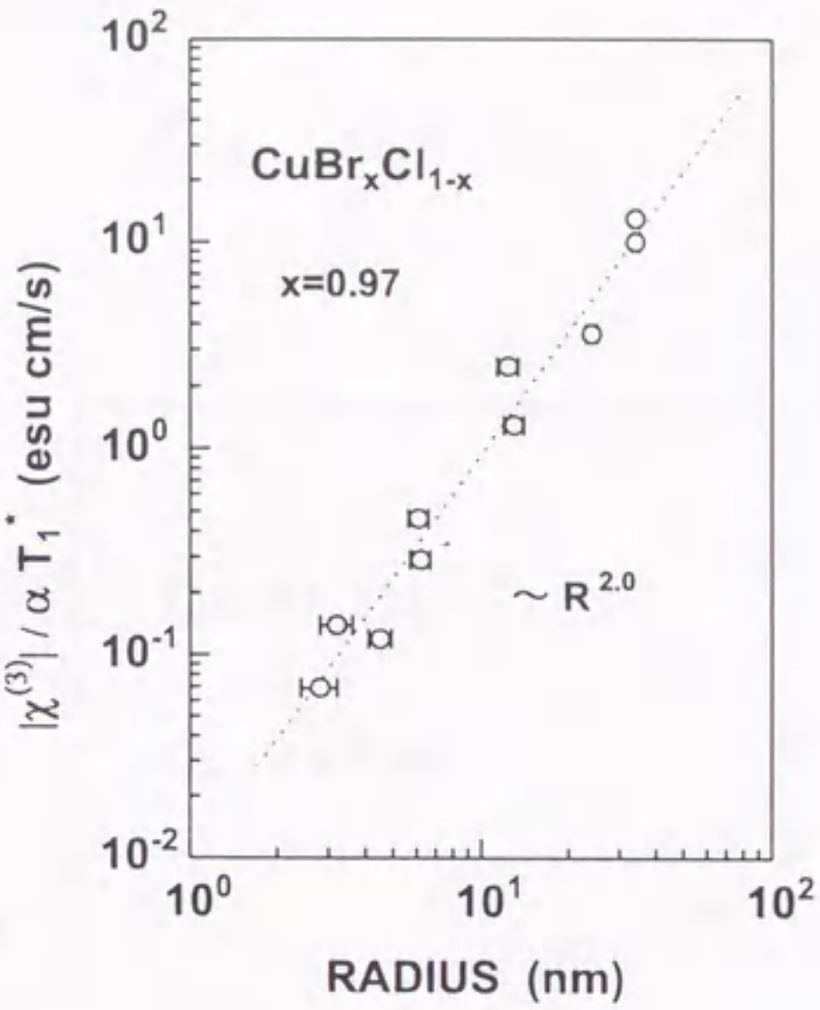

Figure 5.7: Figure of merit $|\chi^{(3)}|/\alpha T_1^*$ for Z_{12} excitons in $CuBr_xCl_{1-x}(x = 0.97)$ nanocrystals as a function of the nanocrystal radius.

Figure 5.7 shows the figure of merit $|\chi^{(3)}|/\alpha T_1^*$ as a function of the mean radius. The figure of merit increases from 0.069 to 13 esu·cm/s upon an increase of R from 2.8 to 34 nm. The $R^{2.0}$-dependence is stronger than the observed $R^{0.8}$-dependence of $|\chi^{(3)}|/\alpha$ in Fig. 5.5(a). This results from the fact that T_1^* is approximately dependent on $R^{-1.2}$. No saturation is observed in the size range studied.

With the above measured parameters, the size dependence of $|\chi^{(3)}|\Gamma_h/\alpha T_1^*$ is calculated, and the results are shown in Fig. 5.8. A least-squares fit yields the $R^{2.1}$-dependence, which is in good agreement with that for CuBr nanocrystals. No saturation behavior is observed in the size range of $R = 2.8 - 34$ nm under study.

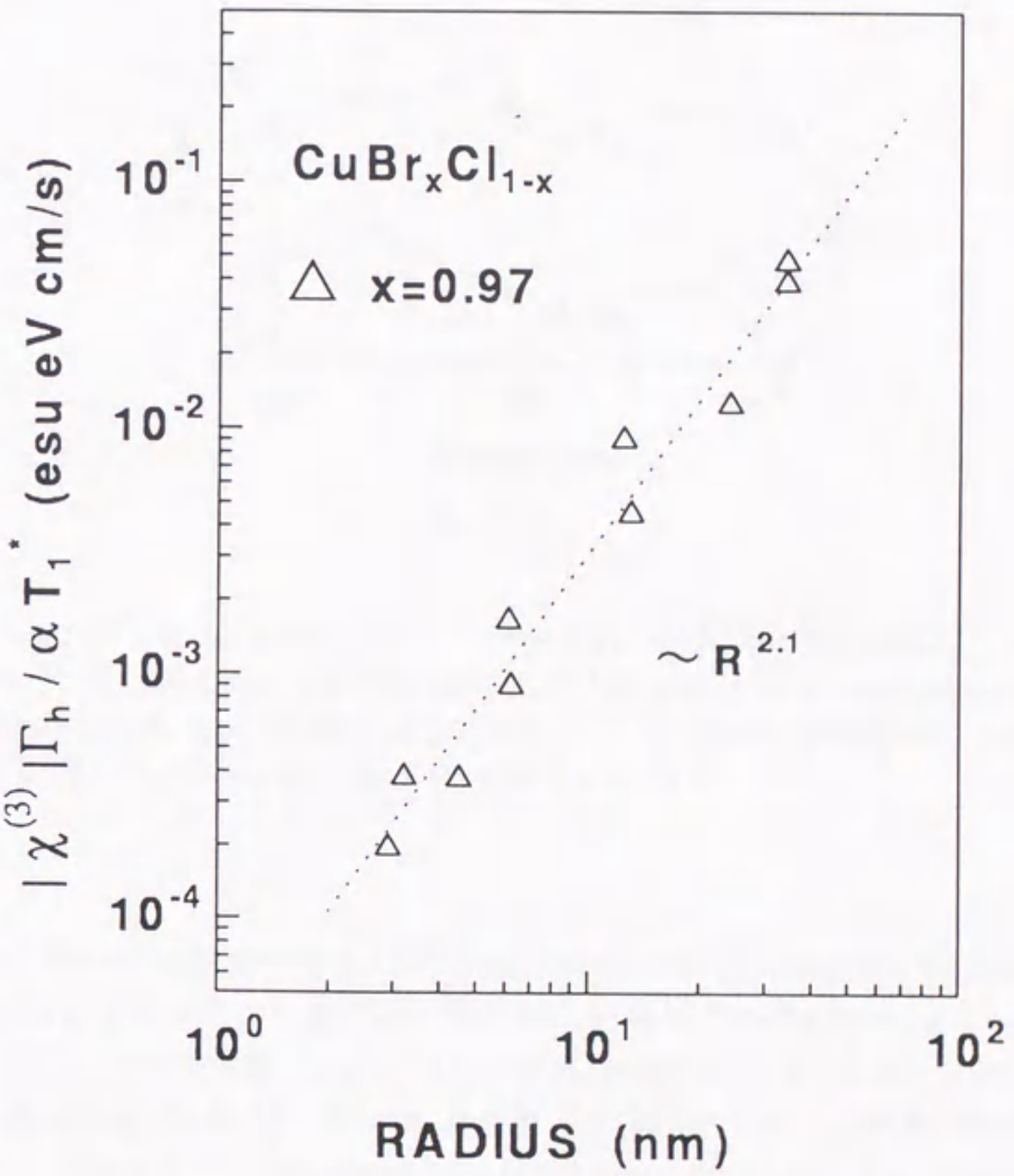

Figure 5.8: Size dependence of f_x for $CuBr_xCl_{1-x}$ nanocrystals ($x = 0.97$) at 77 K. The solid straight line indicates the least-squares fit which is the $R^{2.1}$-dependence.

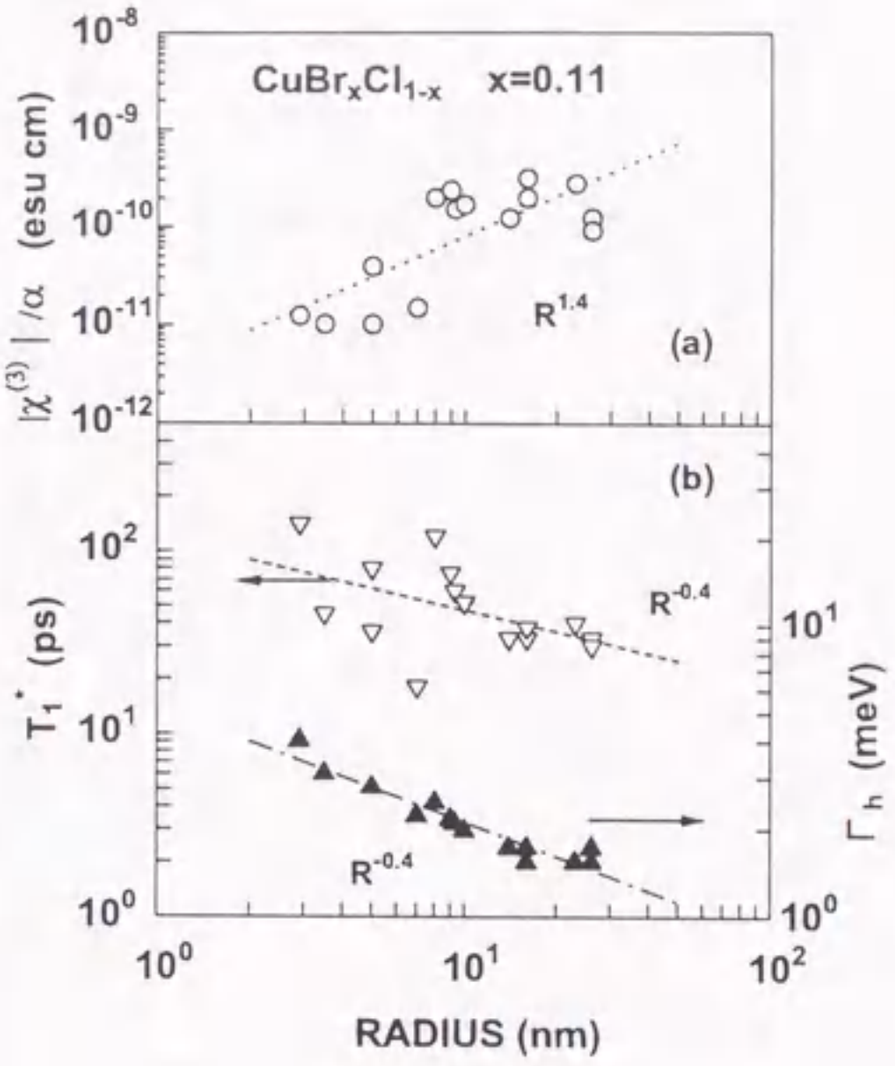

Figure 5.9: (a) $|\chi^{(3)}|/\alpha$ as a function of crystallite radii for $CuBr_xCl_{1-x}$ nanocrystals ($x = 0.11$) at 77 K. The straight line indicates the result of a least-squares fit, which is the $R^{1.4}$-dependence. (b) Radius dependence of T_1^* (open triangles), and Γ_h (closed triangles) for $CuBr_xCl_{1-x}$ nanocrystals ($x = 0.11$) at 77 K.

x=0.11

$|\chi^{(3)}|$ values at the resonance of the Z_3 exciton were measured, and the size dependence of $|\chi^{(3)}|/\alpha$ is shown in Fig. 5.9 (a). $|\chi^{(3)}|/\alpha$ increases with increasing sizes and a least-squares fit yields the $R^{1.4}$-dependence. The $|\chi^{(3)}|/\alpha$ value ranges from $1.0 - 32 \times 10^{-11}$ esu·cm for the radius in the range from $2.9 - 26$ nm. In Fig. 5.9 (b) the size-dependences of T_1^* and Γ_h are shown. Γ_h (closed triangles) shows the $R^{-0.4}$-dependence and the magnitude ranges from $1.6 - 4.0$ meV. The effective lifetimes(open triangles) are in the range of $18 - 140$ ps.

Figure 5.10 shows the figure of merit $|\chi^{(3)}|/\alpha T_1^*$ as a function of the mean radius. The figure of merit increases from 0.088 to 8.4 esu·cm/s upon an increase of R from 2.9 to 16 nm, and the $R^{2.1}$-dependence is obtained by the least-squares fit. However, the figure of merit shows a decreasing trend with increasing size in larger sizes, reducing to 2.8 esu·cm/s at $R = 26$ nm.

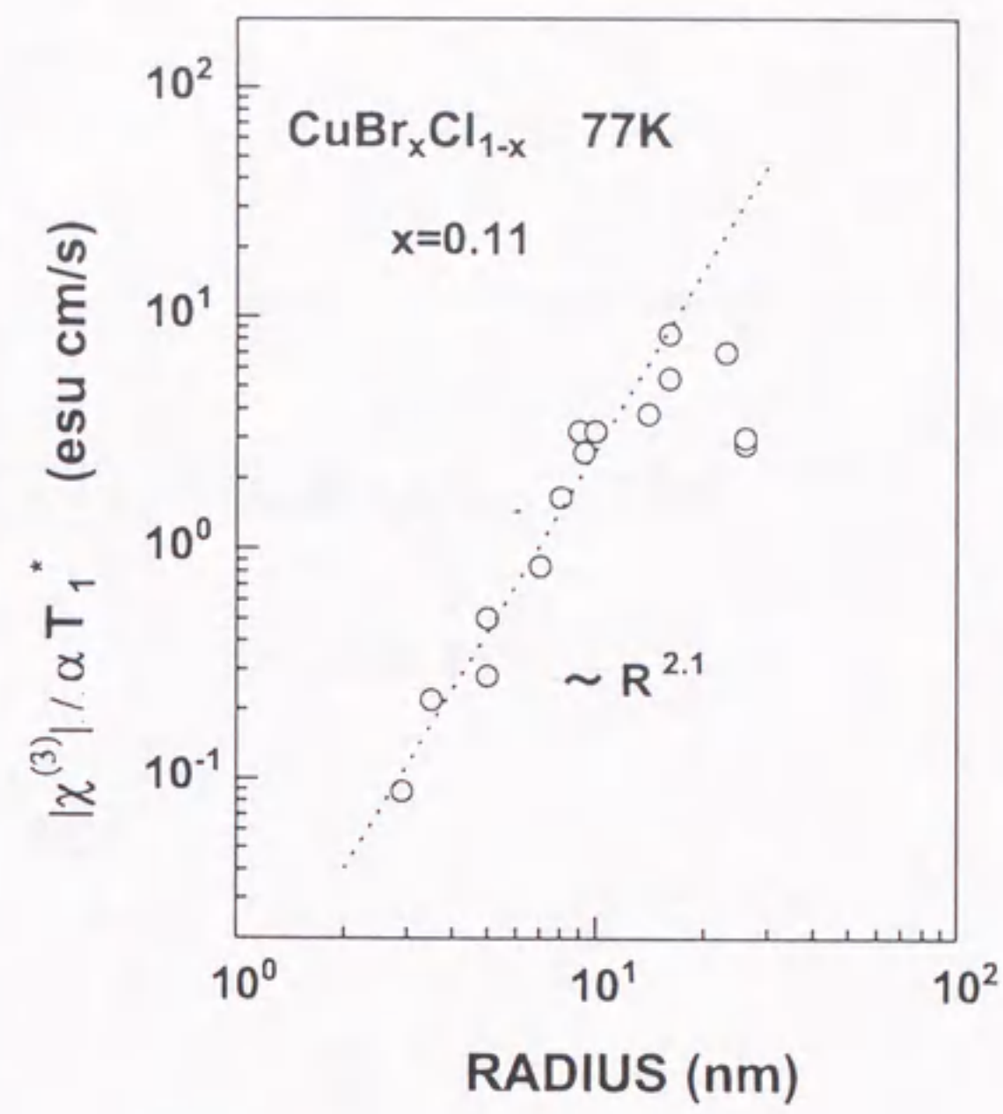

Figure 5.10: Figure of merit $|\chi^{(3)}|/\alpha T_1^*$ for Z_3 excitons in $CuBr_xCl_{1-x}(x = 0.11)$ nanocrystals as a function of the nanocrystal radius.

The size dependence of $|\chi^{(3)}|\Gamma_h/\alpha T_1^*$ is shown in Fig. 5.11. A least-squares fit for the samples with radii below 16 nm yields the $R^{2.1}$-dependence. For the three samples of $R = 23$ and 26 nm, the values of $|\chi^{(3)}|\Gamma_h/\alpha T_1^*$ show the obvious deviation from the $R^{2.1}$-dependence, which indicates that the saturation behavior exists also in $CuBr_xCl_{1-x}(x = 0.11)$ nanocrystals.

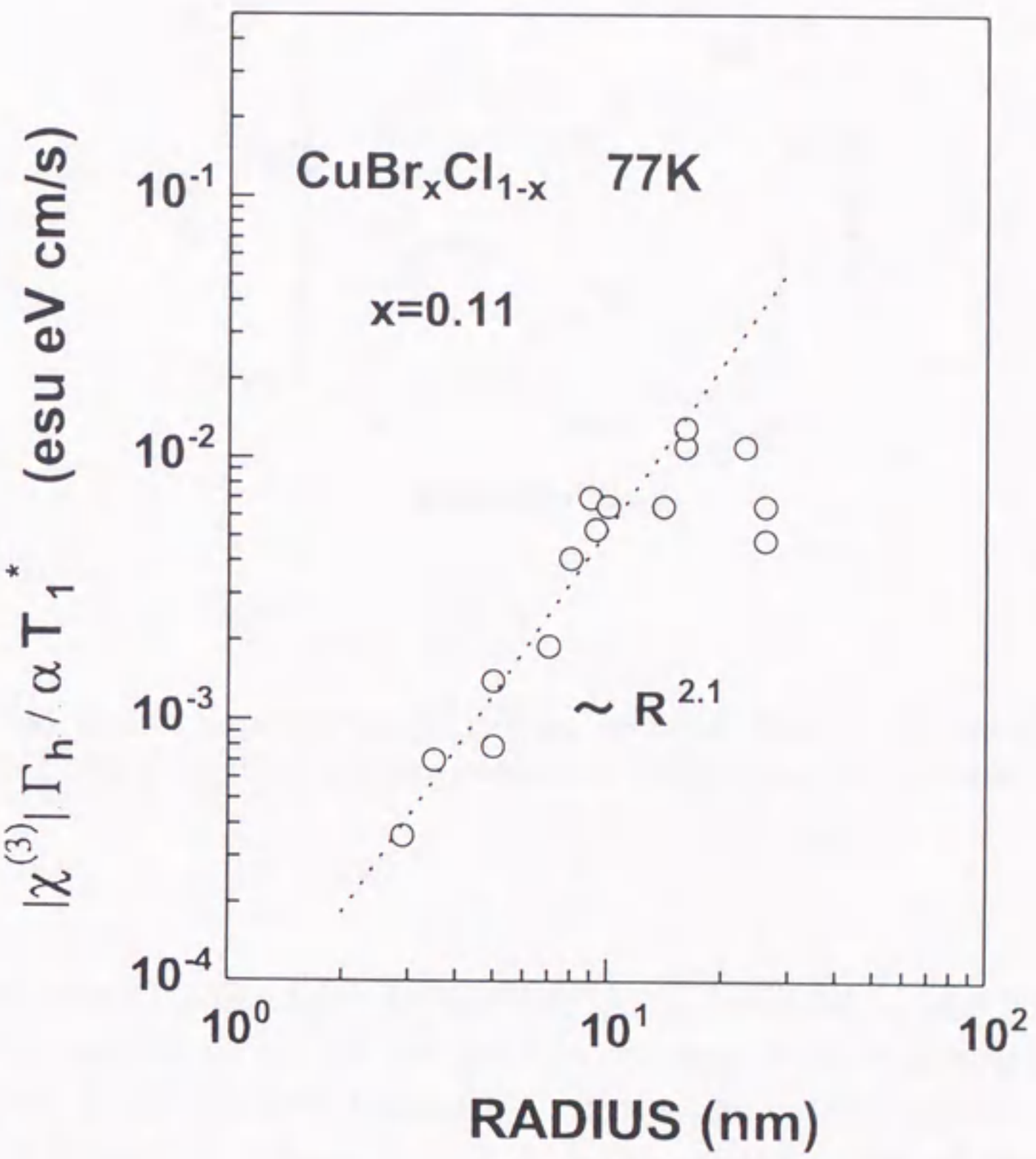

Figure 5.11: Size dependence of f_x for $CuBr_xCl_{1-x}$ nanocrystals ($x = 0.11$) at 77 K. The dotted line indicates the least-squares fit which is the $R^{2.1}$-dependence.

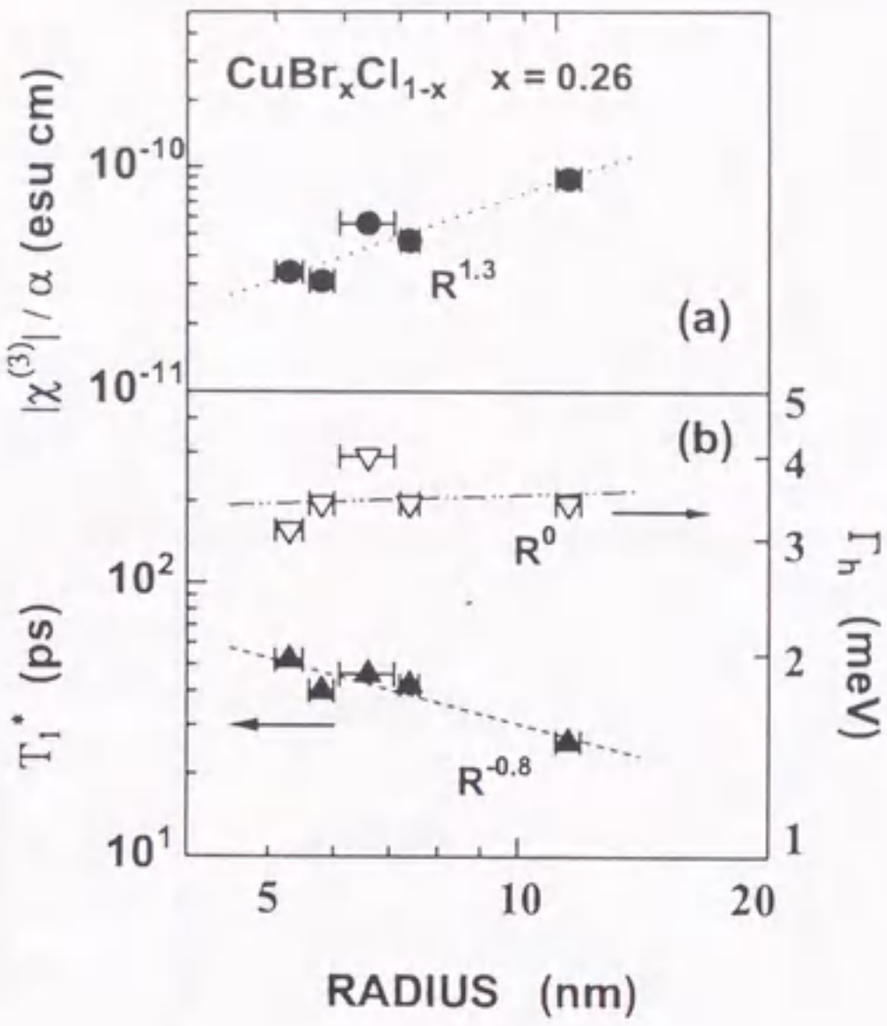

Figure 5.12: (a) Radius dependence of $|\chi^{(3)}|/\alpha$, and (b) effective lifetime T_1^* and homogeneous width Γ_h as a function of mean radius for $CuBr_xCl_{1-x}$ nanocrystals($x = 0.26$) at 77 K.

x=0.26

Figure 5.12 (a) shows the size dependence of $|\chi^{(3)}|/\alpha$ for $CuBr_xCl_{1-x}$ ($x = 0.26$) nanocrystals with mean radii of $5.3 - 11.5$ nm. $|\chi^{(3)}|/\alpha$ increases with increasing sizes and the least-squares fit yields the $R^{0.9}$-dependence. The magnitude of $|\chi^{(3)}|/\alpha$ ranges from $3.0 - 8.7 \times 10^{-11}$ esu·cm. Shown in Fig. 5.12 (b) are the values of effective lifetime T_1^* and Γ_h as a function of radius. Γ_h (open triangles) is almost independent of the size and the values are $3.0 - 4.0$ meV. T_1^* (closed triangles) shows the weak size dependence.

The size dependence of the figure of merit $|\chi^{(3)}|/\alpha T_1^*$ and $|\chi^{(3)}|\Gamma_h/\alpha T_1^*$ are shown in Fig. 5.13 and 5.14, respectively. The figure of merit increases from 0.65 to 3.4 esu·cm/s upon an increase of R from 5.3 to 16 nm, exhibiting the $R^{2.1}$-dependence. The size enhancement of f_x is also observed and its dependence is $R^{2.1}$.

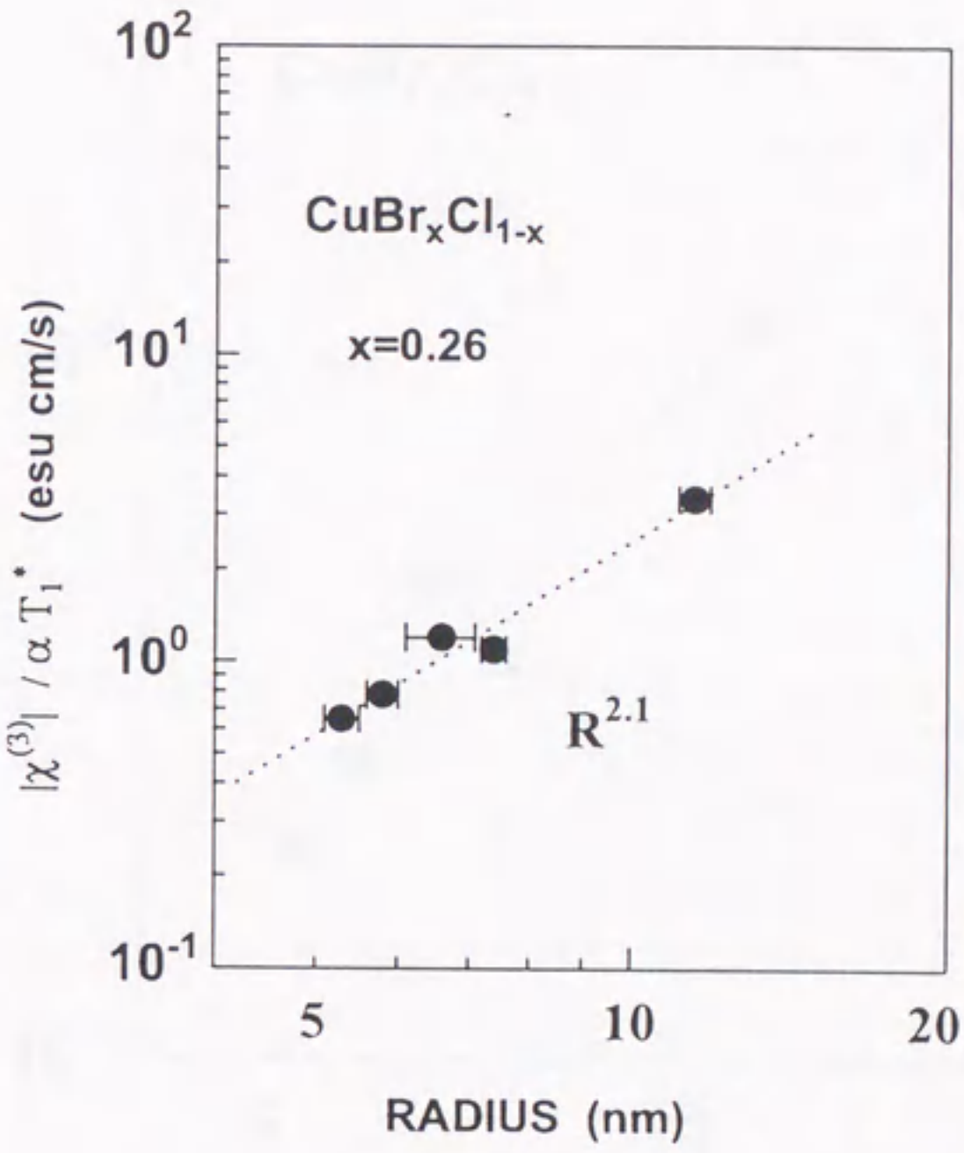

Figure 5.13: Figure of merit $|\chi^{(3)}|/\alpha T_1^*$ in $CuBr_xCl_{1-x}(x = 0.26)$ nanocrystals as a function of the nanocrystal radius.

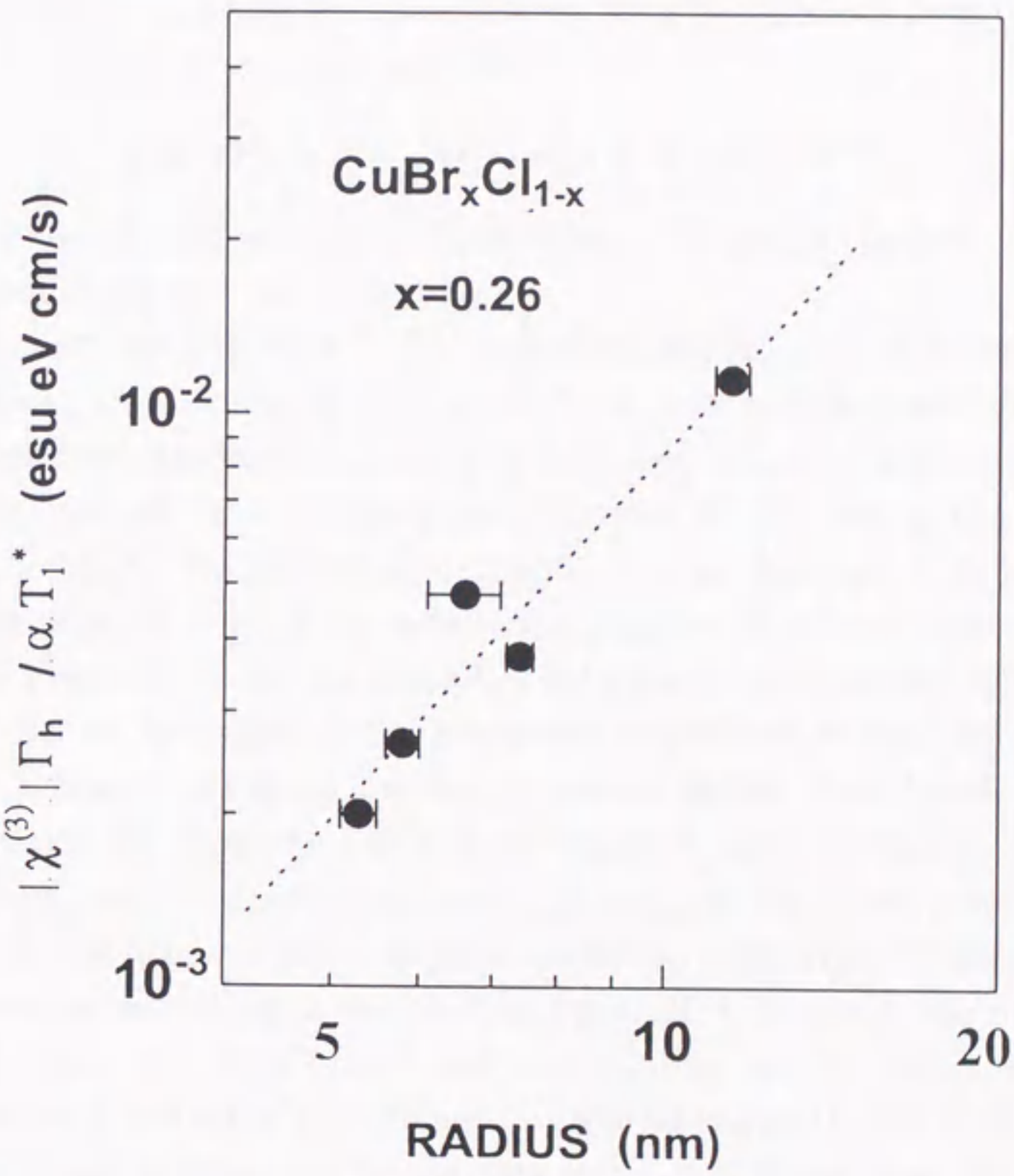

Figure 5.14: (a) Size dependence of $|\chi^{(3)}|\Gamma_h/\alpha T_1^*$ for $CuBr_xCl_{1-x}$ ($x = 0.26$) nanocrystals. The dotted line indicates the result of the $R^{2.1}$-dependence obtained by the least-squares fit.

5.2 Discussion

5.2.1 Saturation of nonlinearities in large-sized nanocrystals

Now, let us make a comparison of the size dependence of exciton oscillator strength among different composition ratios. Fig. 5.15 shows the size-dependences of $|\chi^{(3)}|\Gamma_h/\alpha T_1^*$ for $CuBr_xCl_{1-x}$ nanocrystals with $x = 0, 0.11, 0.26, 0.97$, and 1. For comparison, the mean radius was normalized by the exciton Bohr radius of the corresponding solid solutions. Here the Bohr radius $a_B(x)$ for the composition ratio x is estimated from the Vegard Law for the effective masses of electrons and holes.

$$a_B(x) = x \cdot a_B(CuBr) + (1 - x) \cdot a_B(CuCl), \tag{5.1}$$

where a_B(CuBr)=1.25 nm and a_B(CuCl)=0.68 nm. The results can be classified into two groups: the CuCl-type and the CuBr-type.

For $x = 0$(closed dots) and $x = 0.11$(closed triangles), i.e., the CuCl-type, the oscillator strength increases with increasing sizes up to $R/a_B \approx 20$ and then exhibits a decreasing trend for larger-sized nanocrystals. For $x = 0.97$(open triangles) and $x = 1$(open dots), i.e., the CuBr-type and $x = 0.26$(+), no saturation is observed in the corresponding size range under study. No obvious saturation is seen for the nanocrystals(x=0.97) with the largest size of $R/a_B = 27$. This classification suggests that *the valence band structure plays a role in determining the size-dependent behavior of oscillator strength in large-sized nanocrystals.* Before discussing about the saturation problem, we plot the figure of merit $|\chi^{(3)}|/\alpha T_1^*$ as a function of R/a_B for the five copper halide nanocrystals with different composition ratios. As shown in Fig. 5.16 the figure of merit increases upon an increase of size exhibiting the $R^{2.1}$-dependence for $2 \leq R/a_B \leq 20$ for all the composition ratios. For $R/a_B \geq 20$, the figure of merit shows a decreasing trend with increasing size for the CuCl-type while no saturation is observed for the CuBr-type in the size range studied.

Takagahara and Nair have carried out a calculation on the size dependence of the $|\chi^{(3)}|/\alpha$ values near the exciton resonance in CuCl nanocrystals.[59] They took into account the contributions from the two-exciton states, and found that the $|\chi^{(3)}|/\alpha$ value shall exhibit saturating and decreasing features in large-sized nanocrystals due to the cancellation of the one-exciton mediated enhancement by the two-exciton states. The two-exciton states contribute to the $\chi^{(3)}$ value measured at the the exciton resonance, but the contribution is in sign reverse to that of the lowest one-exciton state. An explicit demonstration of this cancellation may be presented using a three-level model, consisting of the ground state, the lowest exciton state and the two-exciton state. (See Fig. 5.17.) The $|\chi^{(3)}|/\alpha$ is proportional to two dominant terms as

$$|\chi^{(3)}|/\alpha \propto \frac{2|\mu_x|^2}{(\omega_x - \omega) - i\Gamma_h} - \frac{|\mu_{xx}|^2}{(\omega_{xx} - \omega) - i\Gamma_h}. \tag{5.2}$$

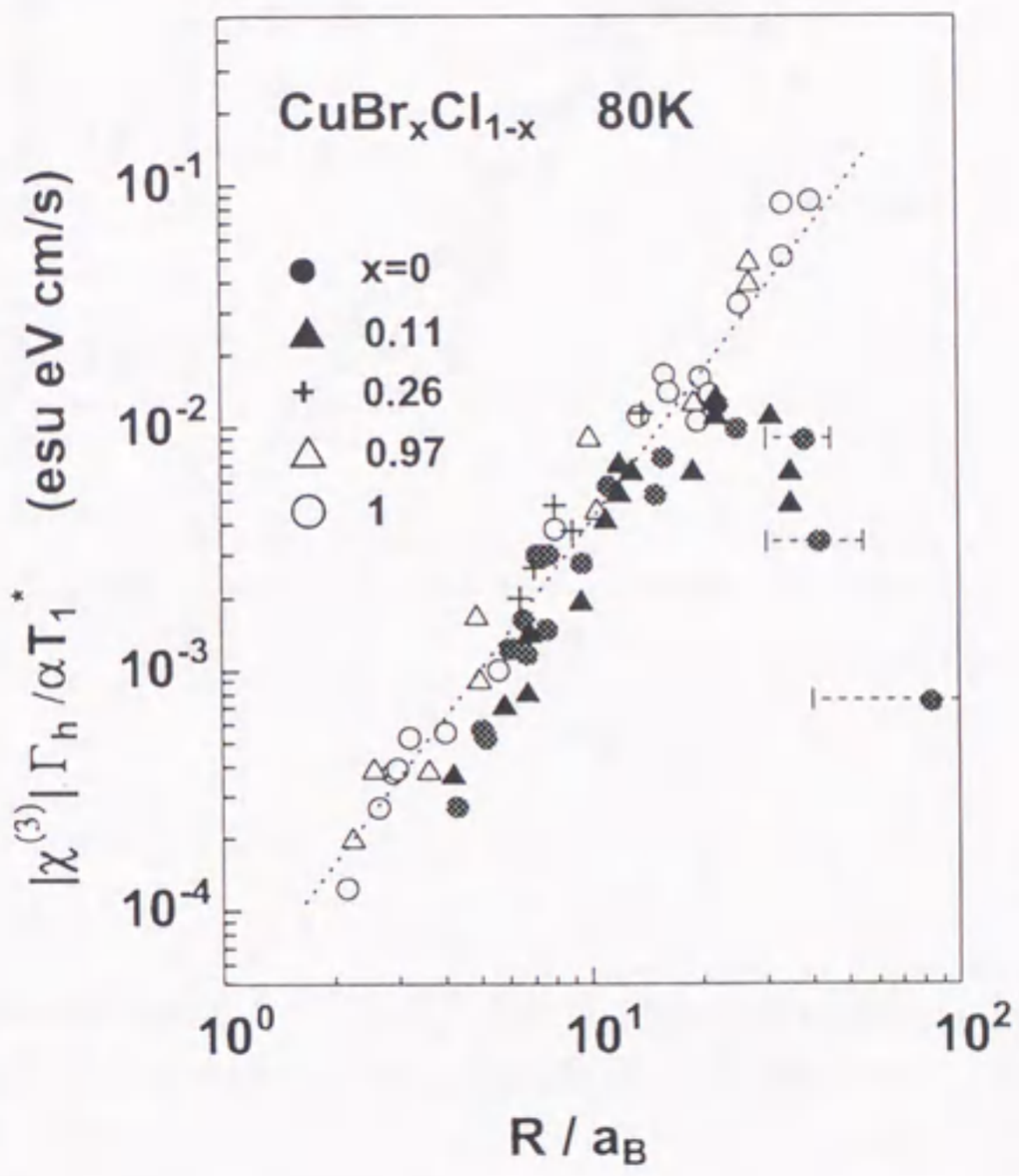

Figure 5.15: Size dependence of $|\chi^{(3)}|\Gamma_h/\alpha T_1^*$ as a function of R/a_B for $CuBr_xCl_{1-x}$ ($x = 0, 0.11, 0.26, 0.97$, and 1) nanocrystals.

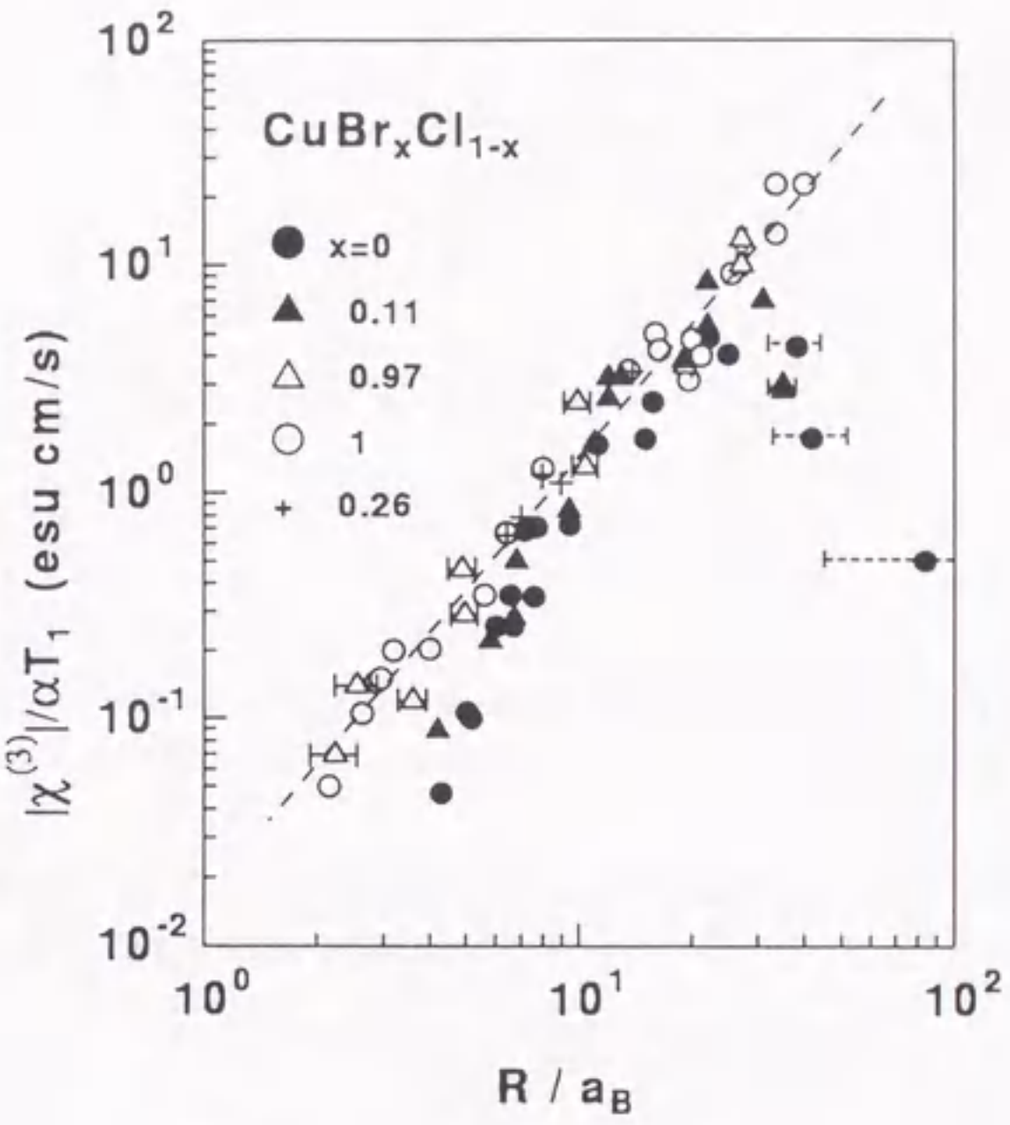

Figure 5.16: Figure of merit $|\chi^{(3)}|/\alpha T_1^*$ for the lowest excitons in $CuBr_xCl_{1-x}$($x = 0, 0.11, 0.26, 0.97$ and 1) nanocrystals as a function of R/a_B.

where the three levels are labeled by 0, X and XX, and ω_X and ω_{XX} denote the transition frequencies, and μ_X and μ_{XX} the dipole moments for the transitions 0→X and X→XX, respectively. [61] The two terms are exactly cancelled out when $|\mu_{XX}|^2 = 2|\mu_X|^2$ and $\omega_X = \omega_{XX}$; a situation to which the energy level structure is found to approach as R increases. The numerically calculated results for CuCl nanocrystals taking into account the inhomogeneous broadening Γ_{ih} are illustrated in Fig. 5.18. The results show that the saturation behavior depends on not only Γ_h but also Γ_{ih}. When the nanocrystal radius is larger than a certain size R_m, the $|\chi^{(3)}|/\alpha$ value starts to decrease from a maximum, and the R_m depends on both Γ_h and Γ_{ih}. A larger Γ_h and/or Γ_{ih} lead to a smaller R_m.

To investigate the different saturation behaviors between the CuBr- and CuCl-type, we compare the measured widths of Γ_h and Γ_{ih} in Table 5.1. Both Γ_h and Γ_{ih} of CuBr-type

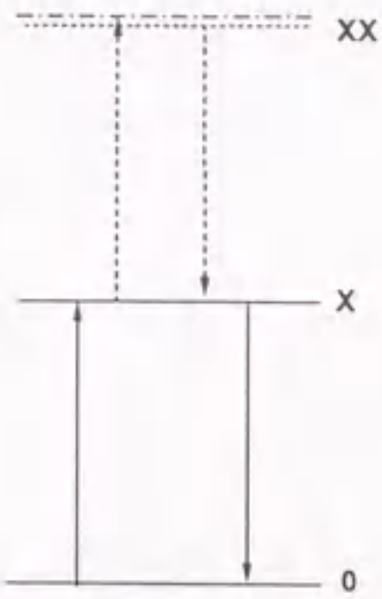

Figure 5.17: Energy diagram of the three-level model. 0, X and XX denote the ground state, confined exciton state and the two-exciton states, respectively.

Table 5.1: Comparison of the homogeneous and inhomogeneous widths of the $Z_3(Z_{12})$-exciton in CuCl(CuBr)-type nanocrystals.

meV	CuBr-type	CuCl-type
Γ_h	3-4	0.9-1.5
Γ_{ih}	8-10	5-6

nanocrystals are larger than those of CuCl-type nanocrystals. The simple application of the theoretical calculation results predicts the smaller R_m for CuBr nanocrystals, i.e., saturation of $|\chi^{(3)}|/\alpha T_1^*$ or f_x should occur at a smaller nanocrystal size of CuBr-type than that of CuCl-type. This is inconsistent with the experimental result in Fig. 5.15. Therefore, Γ_h and/or Γ_{ih} are not the parameters which determine the different saturation behaviors.

As the two-exciton states also exist in the CuBr-type nanocrystals, the contribution of the two-exciton states to nonlinearity should also exist for this type of nanocrystals. Indeed, the emission band from biexcitons is observed in the luminescence spectrum in Fig. 4.8. Therefore, it is natural to attribute the discrepancy of the saturation behaviors to the band structures. In the CuBr-type, the multi-branch Γ_8 band consisting of heavy, light holes and splitted bands due to the k-linear term, lies on the top of the valence bands, while the simple Γ_7 valence band is located on the top of valence bands in the CuCl-type. The two-exciton states should be also multi-branched and complicated in

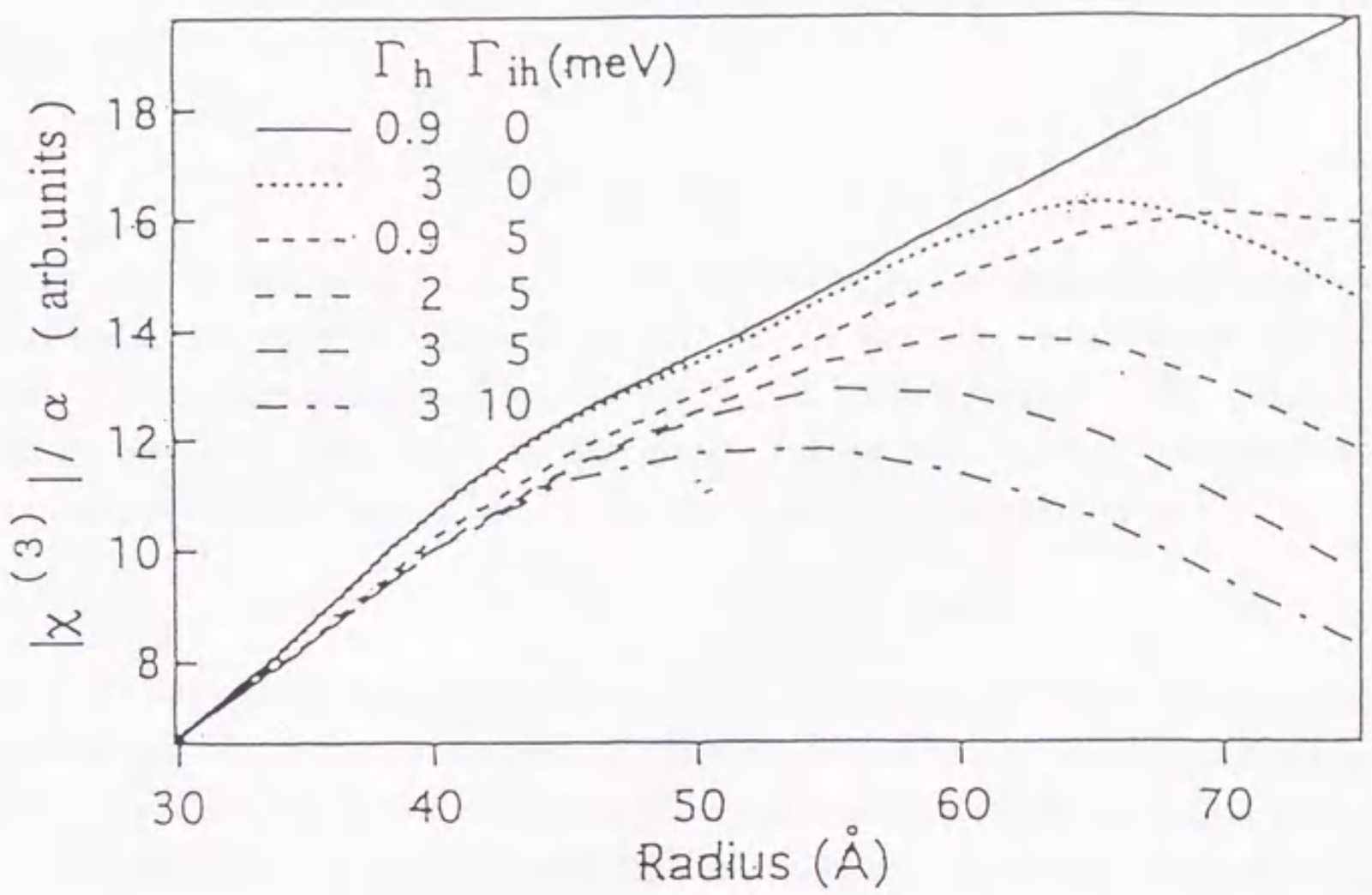

Figure 5.18: Calculated size dependence of the $|\chi^{(3)}|/\alpha$ value near the exciton resonance in CuCl nanocrystals. All the curves have been scaled to the same value at $30\mathring{A}$.

the CuBr-type, and the cancellation due to the two-exciton states may be incomplete or disappearing because of the multiple energy levels. Although a more thorough calculation taking into account the multi-branch band structure is necessary to explain the experimentally observed behaviors for large sizes, the experiments suggest the important role of the two exciton state and the multi-component exciton states in the size dependence of $|\chi^{(3)}|/\alpha T_1^*$ for $R/a_B \geq 20$.

5.2.2 Enhancement factor of oscillator strength in copper halides

Now, we estimate values of the giant oscillator strength per nanocrystal, and compare them with that of the bulk excitons. The value of f_x is calculated using the following equation, [56]

$$Im\chi^{(3)} = 1.3 \times 10^{17} \times \left[\frac{n}{(n^2+2)^2}\right] \cdot \left(\frac{e^2}{2m_0\omega}\right)^2 \cdot \hbar f_x \cdot \frac{\alpha T_1}{\Gamma_h}. \tag{5.3}$$

The enhancement factors of f_x/f_0 are compared for the various composition ratios, where f_0 is defined as the oscillator strength per unit cell for the bulk 1s-exciton in $CuBr_xCl_{1-x}$ crystals. f_0 is experimentally known for CuCl and CuBr reported in the reference,[62] but no reports have been made on the alloy. Taking into account the effective-mass approximation and the Vegard Law, f_0 for the $CuBr_xCl_{1-x}$ is assumed as

$$f_0 = x \cdot f_0(CuBr) + (1-x) \cdot f_0(CuCl), \tag{5.4}$$

where f_0(CuBr)= 0.014 and f_0(CuCl)= 0.00585 have been used.[62] We have also assumed that the dipole matrix element of the band to band transition is constant for the composition ratios. Fig. 5.19 shows the exciton enhancement factor f_x/f_0 as a function of R/a_B for $CuBr_xCl_{1-x}$ nanocrystals with different composition ratios. In the size-range of $2 \leq R/a_B \leq 20$, the same size-dependent enhancement of f_x/f_0, i.e., $f_x/f_0 \propto (R/a_B)^{2.1}$, can be seen for all composition ratios. The enhancement factor ranges from $3-2000$ for the case of CuBr nanocrystals. The values of f_x/f_0 for different composition ratios lay almost on a straight line of the $R^{2.1}$-dependence within a factor of two. Using the least-squares fitting, it has been found that f_x/f_0 can well expressed by $f_x/f_0 = 1.0 \times (R/a_B)^{2.1}$ in nanocrystals of $2 \leq R/a_B \leq 20$ for all the composition ratios. If we compare the experiments with the calculation by Kayanuma (dotted curves), the agreement is fairly good in the size range of $2.2 \leq R/a_B \leq 10$, without any fitting parameters! In the theoretical calculations the assumption of infinite confinement potential has been made, while the confinement potential due to the glass matrix is about 1 eV. The finite confinement potential means less effective confinement, leading to smaller effective volume of the exciton envelope function within the nanocrystal and consequently smaller oscillator strength. This explains the smaller values of the experimental results. Therefore, we have experimentally confirmed that *the size-dependent enhancement of exciton oscillator strength exists indeed in the copper halide nanocrystals as a result of the quantum confinement effect.* It is the size-dependent enhancement effect of oscillator strength that essentially gives rise to the size-dependent enhancement of nonlinearity in semiconductor nanocrystals.

It is worth noting that the nonlocal effect does not work in the crystallite sizes studied here. When the crystallite size is of the order of the light wavelength, the giant oscillator

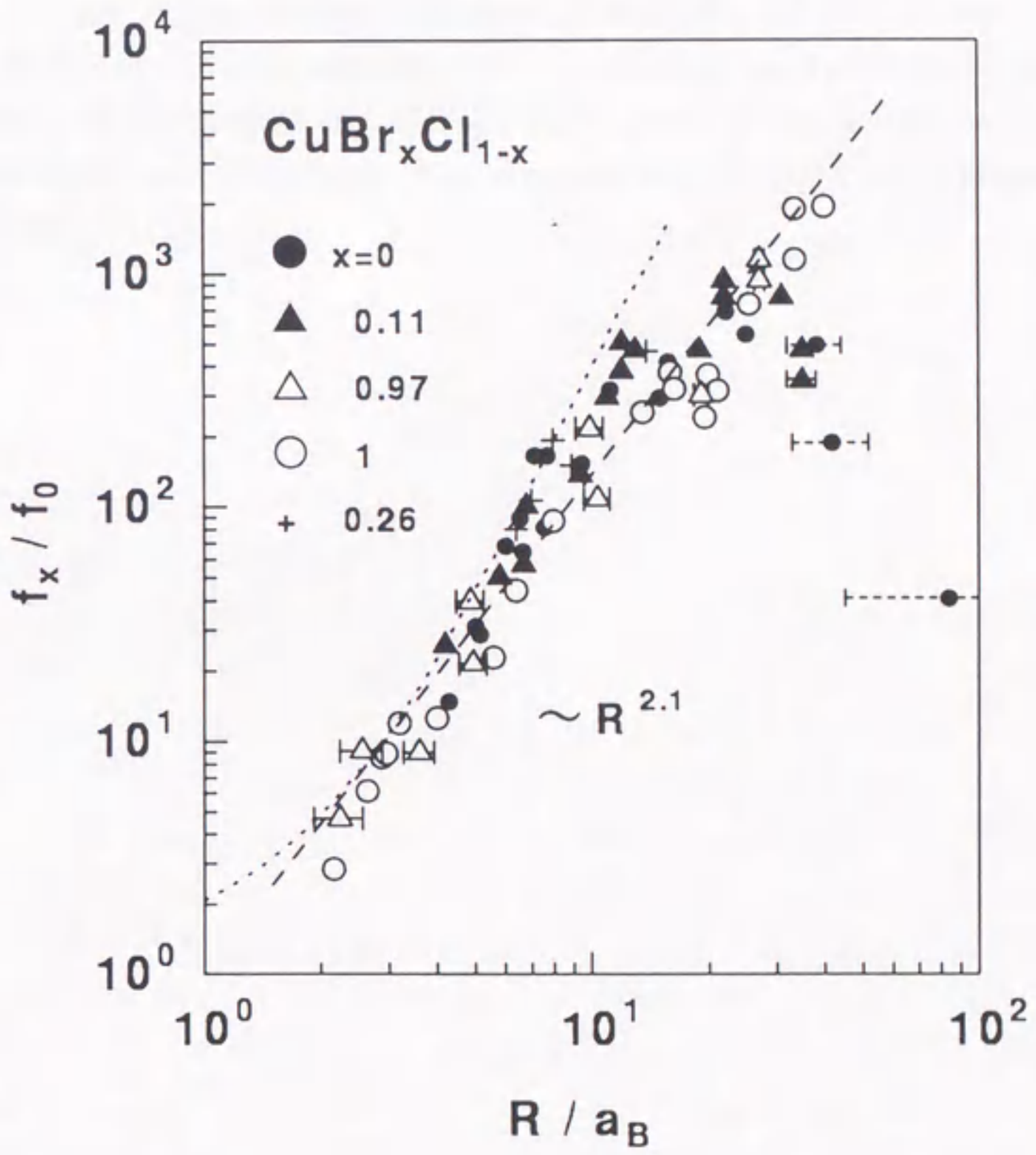

Figure 5.19: Enhancement factor f_x/f_0 of exciton oscillator strength as a function of R/a_B for $CuBr_xCl_{1-x}$ nanocrystals with different composition ratios at 77 K. The broken line indicate the $R^{2.1}$-dependence. The dotted curve indicates the calculation by Kayanuma with the assumption of infinite confinement potential.[18]

strength effect should disappear and the oscillator strength converges to the bulk limit f_0. In this size regime, the excited state is entendedn over the crystallite and an optical polarization can be exerted on a position different from the point irradiated by an incident light. Such a nonlocal effect reflecting the coherence of the electronic wavefunction within the crystallite plays a role in the nonlinear polarization, when the spatial variation of the electric field is comparable to the range of the wavefunction. [63] The light wavelength λ_m near the resonance of Z_{12} excitons in the 40 nm-size nanocrystal is estimated from the dispersion relation of the dielectric constant. Taking $E_T = 2.981$ eV and $\Gamma_h = 4.0$ meV, the refractive index near the resonance is calculated to be 4.03 which yields $\lambda_m \sim 100$ nm. Therefore, for the largest size of CuBr nanocrystal in this study the long wavelength approximation still seems to hold. The nonlocal effects might be important in the size range $R \geq 100$ nm. [63]

Chapter 6

Conclusion

6.1 Origin of size-dependent optical nonlinearities in copper halide nanocrystals

This study has been made to elucidate a role of the quantum confinement effect in the third-order nonlinearity of semiconductor nanocrystals and the origin of the size-dependent enhancement of $\chi^{(3)}$. The copper halide nanocrystals, which typically shows the exciton confinement effect in the weak confinement regime, have been used for the experimental study. First, the size dependence and the origin of nonlinearity have been investigated for CuBr nanocrystals. The third-order nonlinear susceptibility $\chi^{(3)}$ due to the confined excitons has been measured by means of degenerate four-wave mixing using a nanosecond pulse laser. By changing the wavelength of the laser light, the enhancement of $\chi^{(3)}$ has been observed at the exciton resonance. The $|\chi^{(3)}|/\alpha$ values at the Z_{12}-exciton resonance shows an increasing trend with the increasing crystallite mean radius R, and the $R^{0.4}$-dependence by the least-squares fitting is obtained. This size-dependent nonlinearity is analyzed with a two-level atomic model which indicates that the nonlinearity is determined by the exciton lifetime T_1 , homogeneous width Γ_h and the oscillator strength f_x. The crystallite size-dependences of T_1 and Γ_h are investigated by using the time-resolved photoluminescence spectroscopy and the resonant photoluminescence spectroscopy. The $R^{-1.5}$- and $R^{0.1}$-dependence have been found for T_1 and Γ_h, respectively. With the above measured parameters the size dependence of the oscillator strength has been calculated. It has been found that the oscillator strength f_x satisfies the proportionality $f_x \propto R^{2.0}$. It is this size-dependent enhancement of oscillator strength that gives rise to the size-enhancement of nonlinearity due to the confined excitons in CuBr nanocrystals. The size dependence of f_x does not show any saturation in the size range of $2.2 \leq R/a_B \leq 40$. This is in contrast to the saturation behavior of the oscillator strength observed in CuCl nanocrystals, where f_x exhibits a saturation feature with increasing radius around $R/a_B \approx 20$.

To elucidate the mechanism and the origin determining the different behaviors of oscillator strength in the large-size regime, the study has been extended to the solid solutions of CuCl and CuBr in which the valence band structure changes with the composition ratio. We used the $CuBr_xCl_{1-x}$ with different composition ratios, $x = 0.11, 0.26$, and 0.97. In $CuBr_xCl_{1-x}$ (x=0.97) nanocrystals with the CuBr-type band structure the oscillator strength does not show any saturation behavior in the size range of $R/a_B = 2.4 - 27$, while in $CuBr_xCl_{1-x}$(x=0.11) nanocrystals with the CuCl-type band structure the saturation and decreasing features are observed for $R/a_B \leq 20$. This result suggests that the valence band structure play a role in the size dependence of the nonlinearity for the large sizes around $R/a_B \approx 20$. The theoretical calculation on the CuCl-type nanocrystals has revealed that the two-exciton states also contribute to $\chi^{(3)}$ at the exciton resonance. Since the contribution due to the two-exciton states is in sign reverse to that of the lowest one-exciton state, the cancellation of the two contributions occurs. The numerical calculation has shown the saturation behavior of $\chi^{(3)}/\alpha$ in CuCl-type nanocrystals. [59] Therefore, the saturation behavior observed in CuCl-type nanocrystals for $R/a_B \geq 20$ can be explained by this effect.

Such a cancellation effect should also exist in CuBr-type nanocrystals, because there also exist the two-exciton states, which has been confirmed by the observation of the photoluminescence due to the biexciton states. Nevertheless, the experimental results do not show the saturation behavior, indicating that the cancellation effect is eliminated in the CuBr-type nanocrystals in the size range under study. This is attributed to the fact that in CuBr-type nanocrystals both the two-exciton states and one-exciton states consist of multiple components due to the Γ_8 valence band and the k-linear term. The cancellation is expected to be eliminated among the multiple components, in contrast to the case of CuCl-type nanocrystals. It is found that the valence band structure plays a role in determining the size dependence of nonlinearity in large-sized nanocrystals.

Using the measured values of $\chi^{(3)}, \alpha, T_1^*$ and Γ_h, the giant oscillator strength f_x has been calculated. The enhancement factors of f_x with respect to the bulk oscillator strength f_0 have been compared among the copper halide nanocrystals with various composition ratios. It has been found that f_x/f_0 can well expressed by $f_x/f_0 = 1.0 \times (R/a_B)^{2.1}$ in nanocrystals for $2 \leq R/a_B \leq 20$ for all the composition ratios, which indicates that the size-enhancement effect of the oscillator strength is determined by the ratio R/a_B. These results give the experimental proofs for *the giant oscillator strength which is determined by the volume of the exciton coherently generated within a nanocrystal.*

6.2 Size dependence of excitonic nonlinearities in restricted geometries: comparison with the quantum well structures

Let us discuss about the size dependence of $\chi^{(3)}$ in nanocrystals, both in the strong and weak confinement regimes and in quantum well (QW) structures. For simplicity, we consider the case of the constant volume fraction r of nanocrystals in glass, i.e., $N = 3r/4\pi R^3$ in Eq. (1.1), and assume that T_1 and Γ_h are size-independent. In the weak confinement regime ($R/a_B \gg 1$) the observed dependence of f_x is R^2, whereas the theoretical dependence is R^3 for the infinite potential. [18, 19] With these dependences, $\chi^{(3)}$ is dependent on R^1 and R^3 for $f_x \propto R^2$ and R^3, respectively. This enhancement of $\chi^{(3)}$ with *increasing* dimension in the weak confinement regime is essentially originated from the size-dependent oscillator strength per nanocrystal, which results from the coherent superposition of the dipole moment within the envelope function of exciton. To engineer materials with larger optical nonlinearities using semiconductor nanocrystals in this confinement regime, we should use the large nanocrystals, as long as the cancellation effect and the nonlocal effect do not occur.

In the strong confinement regime ($R/a_B \ll 1$), on the other hand, f_x is approximately independent of R.[18] Then, Eq. (1.1) gives the R^{-3}-dependence of $\chi^{(3)}$. In this case, a larger $\chi^{(3)}$ is expected for the smaller dimension. The enhancement of nonlinearity with *decreasing* size in the strong confinement regime results from the increase of nanocrystal density under the condition of the constant volume fraction. Although f_x for the confined exciton (i.e., the electron-hole pair state) also originates from the superposition of dipole moment within the nanocrystal in this regime, in contrast to the weak confinement regime it remains constant despite any further decrease in the volume of the exciton state. The electron-hole correlation becomes more pronounced in the confined exciton within the finite volume than that in the bulk exciton ($\propto (4\pi a_B^3/3)^{-1}$). Consequently, the oscillator strength per unit volume is concentrated by a factor a_B^3/R^3, which is so-called the concentration of oscillator strength, and this concentration corresponds to the increase of the relative spectral weight of the absorption with respect to the bulk exciton by a factor a_B^3/R^3, as discussed by Schmitt-Rink et al.[5] Hence by making a crystal of certain volume into smaller parts we can engineer correspondingly larger optical nonlinearities.

The enhancement in the strong confinement regime can be compared to the well-width dependent enhancement of $\chi^{(3)}$ in QW structures. In typical QW structures of III-V semiconductors. the well-width l_z is smaller than a_B and the Bohr radius is reduced to $a_B/4$ in the exact two-dimensional limit when l_z decreases.[64] The reduction of Bohr radius within the QW layer results from the confinement induced by the enhanced Coulomb interaction. Both the imposed confinement by the barriers and the Coulomb ineraction

reduce the extent of exciton wavefunction. The exciton oscillator strength *per unit surface* is proportional to $1/\pi a_B^2$, and thus is enhanced with the reducing Bohr radius. Indeed, the theoretical calculation of $\chi^{(3)}$ shows the l_z^{-1}-dependence if we ignore the well-width dependence of T_1 and Γ_h.[65] Therefore, the nonlinearity in QW structures is enhanced with *decreasing* dimension, which is essentially the same as that for nanocrystals in the stong confinement regime.

Acknowledgments

The author greatly acknowledges his thanks to Prof. A. Nakamura for his leading instructions and stimulating and instructive discussions throughout the seven-year research and life at the Applied Physics department of Nagoya University. The author is deeply impressed by his prudence, diligence, strict attitude as well as the spirit of criticising and persistent pursuing in research. The author shall be benefited for life due to what he has learned throughout the period of study and life.

The author also greatly acknowledges his thanks to Prof. M. Sakata and Associated Prof. Y. Moritomo for their critical reading of the thesis and discussions.

Special thanks are due to Prof. M. Sakata, Dr. M. Takata[1] and their collaborators Y. Kuboda, S. Yamamura, B. Umeda, E. Nishibori and other members for the splendid work in X-ray diffraction measurements. It is a significant work to determine the size and the composition ratio for the $CuBr_xCl_{1-x}$ nanocrystals in this study. Thanks are also due to T. Manabe, N. Sugimoto and S. Itoh in Asahi Co. for preparing the high quality CuBr-doped glasses, and to S. Sasaki and M. Ohta for their $CuBr_xCl_{1-x}$ samples of efforts. Mr. T. Sumi and other technical staffs in the Applied Physics Department for their help in troubleshootings of cryostat.

The author acknowledges with pleasure the impressive conversations he has had with many members in the lab and the Applied Physics Department, in particular those with Dr. T. Tokizaki[2] , Dr. M. Ichida and Dr. Y. Hamanaka. They are thanked for the helpful instructions and advices. Special thanks are due to Dr. M. Ichida for installing the LaTeXwhich saves a great labor for the author to finish the manuscript smoothly. Thanks are due to the helpful advice and heartful help during the early stage of this study, especially those from H. Kitagawa, S. Kataoka and H. Sakai, T. Ukai, and the other members in the lab are also thanked. H. Ohmura, H. Ohara, and M. Ota are thanked for their collaboration in some experiments.

Valuable and fruitful discussions with Dr. T. Takagahara on the saturation problem of the oscillator strength were greatly appreciated. Stimulating and critical discussions with Prof. T. Itoh, Y. Masumoto and K. Cho in the meetings of Physical Society of Japan were also faithfully acknowledged. Discussions with Prof. S. Kon, N. Tanaka and C. Flytzanis on the research of CuBr nanocrystals were also acknowledged.

The author thanks Aichi Science & Technology Foundation for the fellowships, and thanks the Meitetsu Kokusaiyukue Foundation, Chyubu Denryoku Co. for the financial support in the author's Master course study.

Finally, the author wishes to record his indebtedness to his family in China and Japan, whose constant encouragement made this work possible.

---

[1] Present address: Faculty of Science and Engineering, Shimane University, Matsue, 690 Japan.
[2] Present address: Electrotechnology Laboratory, MITI, Ibaraki, 305 Japan.

Bibliography

[1] C. Weisbuch and B. Vinter. *Quantum Semiconductor Structures.* Academic Press, 1991.

[2] S. Schmitt-Rink, D. S. Chemla, and D. A. B. Miller. *Advances in Physics*, page 89, 1989.

[3] H. Haug. *Optical Nonliearities and Instabilities in Semiconductors.* Academic Press, 1988.

[4] R. K. Jain and R. C. Lind. *J. Opt. Soc. Am.*, 73:647, 1983.

[5] S. Schmitt-Rink, D. A. B. Miller, and D. S. Chemla. *Phys. Rev. B*, page 8113, 1987.

[6] P. Roussignol, D. Ricard, and C. Flytzanis. *Appl. Phys. B51, 437*, 1990.

[7] D. W. Hall and N. F. Borrelli. *J. Opt. Soc. Am. B5, 1650*, 1988.

[8] S. H. Park, R. A. Morgan, Y. Z. Hu, M. Linderberg, S. W. Koch, and N. Peyghambarian. *J. Opt. Soc. Am. B7, 2097*, 1990.

[9] H. Shinojima, J. Yumoto, and N. Uesugi. *Appl. Phys. Lett.*, page 298, 1992.

[10] A. Nakamura, Y.L. Li, T. Kataoka, and T. Tokizaki. *J. Lumin.*, 60&61:376, 1994.

[11] Y. Kato, C. I. Yu, and T. Goto. *J. Phys. Soc. Jpn.*, 28:104, 1970.

[12] A. Goldmann. *Phys. Stat. Solidi. B*, 81:9, 1977.

[13] R. S. Knox. *Theory of Excitons.* Academic Press, 1963.

[14] K. Cho. *Excitons.* Springer, 1979.

[15] D. C. Reynolds and T. C. Collins. *Excitons, their properties and uses.* Academic Press, 1981.

[16] Al. L. Efros and A. L. Efros. *Sov. Phys. Semicond. 16, 772*, 1982.

[17] L. E. Brus. *J. Chem. Phys.*, 80:4403, 1984.

[18] Y. Kayanuma. *Phys. Rev. B*, 38:9797, 1988.

[19] E. Hanamura. *Phys. Rev. B*, 37:1273, 1988.

[20] T. Takagahara. . *Phys. Rev. B*, 39:10206, 1989.

[21] E. I. Rashba and G. E. Gurgenishvili. *Soviet Phys. -Solid State*, 4:759, 1962.

[22] C. H. Henry and K. Nassau. *Phys. Rev. , B*, 1:1628, 1970.

[23] E. Hanamura. *Phys. Rev. B*, 38:1228, 1988.

[24] M. Cardona. *Phys. Rev.*, 129:69, 1963.

[25] K. Shindo, A. Morita, and H. Kamimura. *J. Phys. Soc. Japan*, 20:2054, 1965.

[26] M. Luttinger. *Phys. Rev.*, 102:1030, 1956.

[27] E. O. Kane. *Phys. Rev. B*, 11:1512, 1975.

[28] Y. Nozue. *J. Phys. Soc. Japan*, 51:1840, 1982.

[29] A. I. Ekimov, A. A. Onushchenko, A. G. Plyukhin, and Al. L. Efros. *Sov. Phys. JETP*, page 894, 1985.

[30] N. Bloembergen. *Nonlinear Optics.* Benjamin. Inc., 1965.

[31] Y. R. Shen. *The Principles of Nonlinear Optics.* John. Wiley & Sons, Inc., 1984.

[32] N. Bloembergen and Y. R. Shen. *Phys. Rev.*, 133:A37, 1964.

[33] T. Yajima and H. Souma. *Phys. Rev. A*, 17:309, 1978.

[34] A. Nakamura, H. Yamada, and T. Tokizaki. *Phys. Rev. B*, 40:8585, 1989.

[35] Y. Kondo, N. Sugimoto, T. Manabe, S. Ito, T. Tokizaki, and A. Nakamura. *Nonlinear Optics*, 13:143, 1995.

[36] B. E. Warren. *X-ray Diffraction.* Addison-Wesley, 1969.

[37] A. Guinier. *X-Ray Diffraction.* Freeman, San Francisco, 1963.

[38] L. S. Birks and H. J. Friedman. *J. Appl. Phys.*, 17:687, 1946.

[39] B. Champagnon, B. Andrianasolo, A. Ramos, M. Gandais, M. Allais, and J-P Benoit. *J. Appl. Phys.*, 73:2775, 1993.

[40] R. W. Wyckoff. Crystal structures, 1963.

[41] H. J. Eichler. special issue on dynamic gratings and four-wave-mixing. *IEEE J. Quantum Electron.*, QE-22, 1984.

[42] D. S. Chemla, D. A. Miller, P. W. Smith, A. C. Gossard, and W. Wiegmann. *IEEE J. Quantum Electron.*, QE-20:265, 1984.

[43] C. Weber, U. Becker, R. Renner, and C. Klingshirn. *Appl. Phys. B.*, 45:113, 1988.

[44] H. J. Eichler and F. Massman. *J. Appl. Phys.*, 53:3237, 1982.

[45] M. N. Islam, E. P. Ippen, E. G. Burkhardt, and T. J. Bridges. *J. Appl. Phys.*, 59:2619, 1986.

[46] P. N. Butcher and D. Cotter. *The Elements of Nonlinear Optics.* Cambridge University Press, Cambridge, 1990.

[47] H. Hiraga, S. Ohmi, T. Tokizaki, and A. Nakamura. unpublished.

[48] B. P. Singh, M. Samoc, H. S. Nalwa, and P. N. Prasad. *J. Chem. Phys. 925, 2758,* 1990.

[49] D. Richardson, E. M. Wright, and S. W. Koch. *Phys. Rev. A*, 41:1620, 1990.

[50] M. Mitsunaga, H. Shinojima, and K. Kubodera. *J. Opt. Am. B*, 5:1448, 1988.

[51] T. Itoh and M. Furumiya. *J. Lumin.*, 48&49:704, 1991.

[52] A. Nakamura, M. Ohta, and S. Sasaki. *J. Lumin.*, 72-74:370, 1997.

[53] J. E. Potts, R. C. Hanson, C. T. Walker, and C. Schwab. *Solid State Commun.*, 13:389, 1973.

[54] T. Wamura, Y. Masumoto, and T. Kawamura. *Appl. Phys. Lett.*, 59:1758, 1991.

[55] T. Tokizaki, T. Kanetaka, H. Ohmura, and A. Nakamura. *Prog. Crystal Growth and Charact.*, 33:187, 1996.

[56] T. Kataoka, T. Tokizaki, and A. Nakamura. *Phys. Rev. B*, 48:2815, 1993.

[57] H. Yamada, T. Tokizaki, and A. Nakamura. unpublished.

[58] A. I. Ekimov, Al. L. Efros, and A. A. Onushchenko. *Solid State Commun.*, 56:921, 1985.

[59] S. V. Nair and T. Takagahara. *Phys. Rev. B*, 53:R10516, 1996.

[60] T. Takahashi and T. Goto. *J. Phys. Soc. Japan*, 25:461, 1968.

[61] S. V. Nair and T. Takagahara. *Phys. Rev. B*, 55:5153, 1997.

[62] H. Akiyama, T. Kuga, M Matsuoka, and M. Kuwata-Gonokami. *Phys. Rev. B*, 42:5621, 1990.

[63] Hajime Ishihara and Kikuo Cho. *Phys. Rev. B42, 1724*, 1990.

[64] M. Shinada and S. Sugano. *J. Phys. Soc. Jpn.*, 21:1936, 1966.

[65] T. Takagahara. *Phys. Rev. B*, 40:12359, 1989.

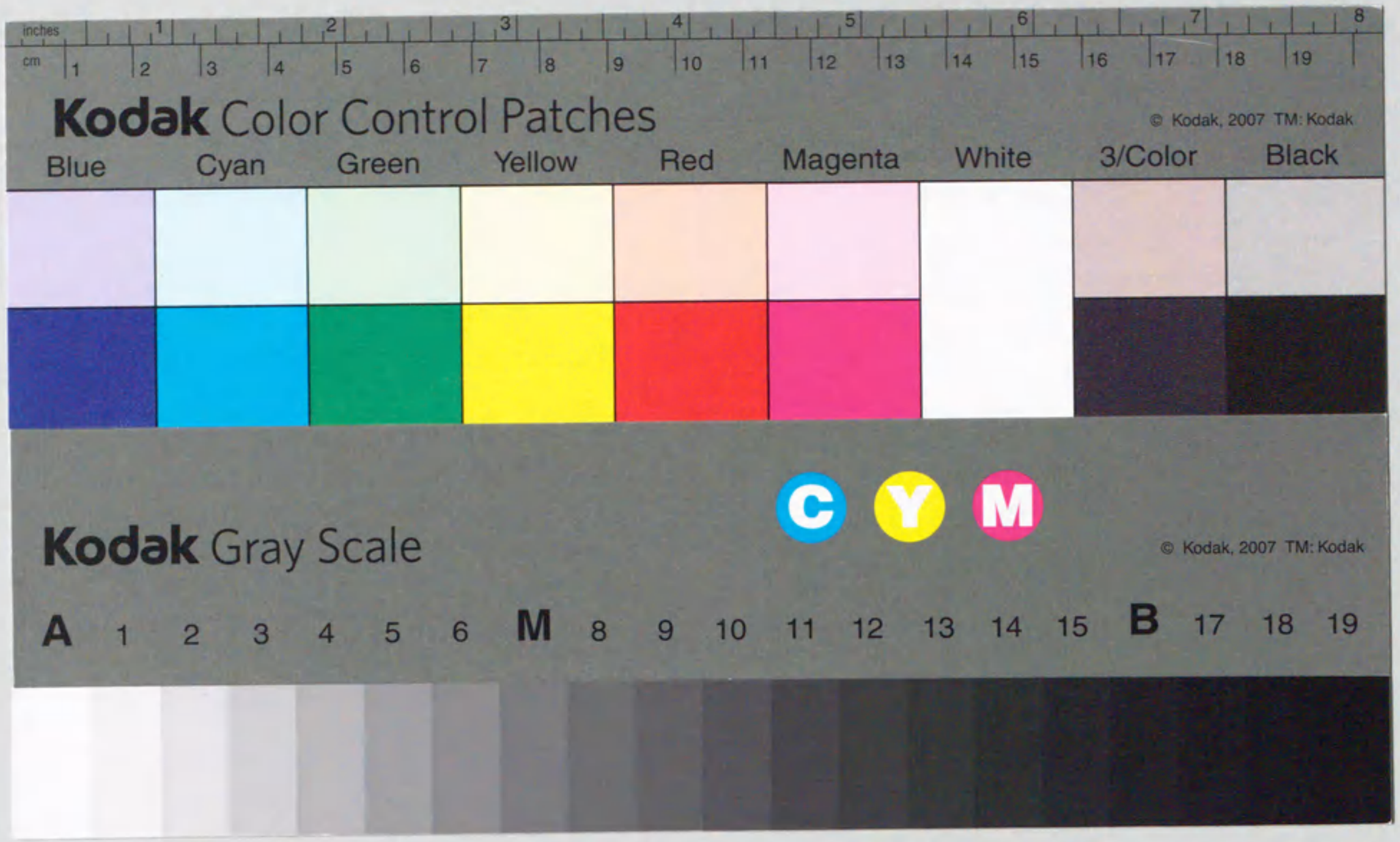
inches
cm
Kodak Color Control Patches
© Kodak, 2007 TM: Kodak
Blue
Cyan
Green
Yellow
Red
Magenta
White
3/Color
Black
Kodak Gray Scale
C
Y
M
© Kodak, 2007 TM: Kodak
A 1 2 3 4 5 6 M 8 9 10 11 12 13 14 15 B 17 18 19